THEORY AND APPLICATIONS OF ELECTROMAGNETIC METAMATERIALS

EDITED BY: Fajun Xiao, Weiren Zhu, Xingzhan Wei and Ivan Rukhlenko

frontiers Research Topics

About Frontiers

Frontiers is more than just an open-access publisher of scholarly articles: it is a pioneering approach to the world of academia, radically improving the way scholarly research is managed. The grand vision of Frontiers is a world where all people have an equal opportunity to seek, share and generate knowledge. Frontiers provides immediate and permanent online open access to all its publications, but this alone is not enough to realize our grand goals.

Frontiers Journal Series

The Frontiers Journal Series is a multi-tier and interdisciplinary set of open-access, online journals, promising a paradigm shift from the current review, selection and dissemination processes in academic publishing. All Frontiers journals are driven by researchers for researchers; therefore, they constitute a service to the scholarly community. At the same time, the Frontiers Journal Series operates on a revolutionary invention, the tiered publishing system, initially addressing specific communities of scholars, and gradually climbing up to broader public understanding, thus serving the interests of the lay society, too.

Dedication to Quality

Each Frontiers article is a landmark of the highest quality, thanks to genuinely collaborative interactions between authors and review editors, who include some of the world's best academicians. Research must be certified by peers before entering a stream of knowledge that may eventually reach the public - and shape society; therefore, Frontiers only applies the most rigorous and unbiased reviews.
Frontiers revolutionizes research publishing by freely delivering the most outstanding research, evaluated with no bias from both the academic and social point of view. By applying the most advanced information technologies, Frontiers is catapulting scholarly publishing into a new generation.

What are Frontiers Research Topics?

Frontiers Research Topics are very popular trademarks of the Frontiers Journals Series: they are collections of at least ten articles, all centered on a particular subject. With their unique mix of varied contributions from Original Research to Review Articles, Frontiers Research Topics unify the most influential researchers, the latest key findings and historical advances in a hot research area! Find out more on how to host your own Frontiers Research Topic or contribute to one as an author by contacting the Frontiers Editorial Office: frontiersin.org/about/contact

THEORY AND APPLICATIONS OF ELECTROMAGNETIC METAMATERIALS

Topic Editors:
Fajun Xiao, Northwestern Polytechnical University, China
Weiren Zhu, Shanghai Jiao Tong University, China
Xingzhan Wei, Chongqing Institute of Green and Intelligent Technology (CAS), China
Ivan Rukhlenko, The University of Sydney, Australia

Table of Contents

Editorial: Theory and Applications of Electromagnetic Metamaterials

Fajun Xiao[1], Weiren Zhu[2]*, Xingzhan Wei[3] and Ivan D. Rukhlenko[4]

[1]*MOE Key Laboratory of Material Physics and Chemistry Under Extraordinary Conditions, and Shaanxi Key Laboratory of Optical Information Technology, School of Physical Science and Technology, Northwestern Polytechnical University, Xi'an, China,* [2]*Department of Electronic Engineering, Shanghai Jiao Tong University, Shanghai, China,* [3]*Chongqing Institute of Green and Intelligent Technology, Chinese Academy of Sciences, Chongqing, China,* [4]*Institute of Photonics and Optical Science (IPOS), School of Physics, The University of Sydney, Camperdown, NSW, Australia*

Editorial on the Research Topic

Theory and Applications of Electromagnetic Metamaterials

Metamaterials, a kind of artificially structured materials made of subwavelength composites, are endowed with a plethora of intriguing properties that do not exist in nature. For decades, metamaterials have flourished and been kept redefining the boundaries of fundamental and applied sciences. In particular, the emerging concept of metasurfaces, a two-dimensional form of metamaterials, provides a versatile solution to manipulating electromagnetic waves with almost arbitrary amplitudes, phases, polarizations, and frequencies, facilitating the implement of novel integrated microwave and photonics devices with greatly enhanced performances. This special issue holds original research and review articles on several topics of metamaterials including reconfigurable metasurfaces, perfect metamertial absorbers, topological metamaterials, and thus highlights the latest developments in the electromagnetic metamaterials both in the theory and applications.

In Zahra et al., Zahra provided a comprehensive introduction of metasurfaces, especially their applications in the modulations of the amplitudes, phases, and polarizations of electromagnetic waves. Special emphasis was given on the newly developed smart metasurfaces that possess the active, reconfigurable, and programmable characteristics *via* the electrical, optical, thermal and mechanical ways. An outlook of the development trend was also made for this fascinating area. In another review article, Ma et al. overviewed the recent advances in metamaterial-based temperature sensing. They comprehensively analyzed the enhanced sensing performances of typical metamaterial designs, in terms of the sensitivity and resolution, which may shed light on the solution toward the future high-precision sensing.

Significant interests have been devoted on the manipulations of electromagnetic waves using metasurfaces through phase modulations. Bai et al. proposed a facile structure composed of hexagonal-ring to efficiently generate the orbital angular momentum waves. This metasurface is insensitive to the polarization of the illumination and holds a great promise for radio communications and radar applications. Cao et al. presented a high efficient and cost-effective programmable metasurface that achieve a real-time scanning pencil beams with desirable directions. Yang et al. presented a theoretical framework for the modulation of WiFi signals, where reconfigurable metasurface loaded with varactor diodes is use to effectively control the in-band transmission and reflection coefficients for maintaining different far-field electromagnetic characteristics. Ahamed et al. numerically presented a reconfigurable metamaterial filter for THz waves, based on the binary response by controlling the plasmatic electron packet in electric split-ring resonators. Such a binary filter could be digitally encoded for the information processing systems.

Apart from phase modulations, metamaterials/metasurfaces allow extreme control of the electromagnetic waves' magnitudes. One of the key applications for such a modulation is perfect metamaterial absorbers. Wang et al. proposed a graphene-based metamaterial absorber that shows merits of broadband high absorption, polarization insensitivity, and immune to wide incident angle. Deng et al. presented a stereo perfect metamaterial absorber based on standing gear-shaped resonant structure, which shows wide-incident-angle stability for both TE and TM modes. Liu et al. reported a dual-band optical metamaterial absorber with peak absorptivities of 99.986% at 1,310 nm and 99.421% at 1,550 nm. The potential application as a refractive index sensor was also numerically discussed.

The research of topological insulators is another hot topic in metamaterials. While conventional topological insulators typically made of either dielectric or metallic materials in the previous references, Du et al. proposed a hybrid topological model consisting of both metal and dielectric materials, offering a new method for achieving topological edge states.

We would like to thank all contributing authors to the issue, and the editorial staff of Frontiers in Physics for making this special issue possible.

AUTHOR CONTRIBUTIONS

All authors listed have made a substantial, direct, and intellectual contribution to the work and approved it for publication.

Polarization-Insensitive Reflective Metasurfaces for Highly Efficient Generation of OAM Beams

Xudong Bai *

R&D Center, Shanghai Aerospace Electronics Company Ltd., China Academy of Aerospace Electronics Technology, Shanghai, China

The polarization-insensitive reflective metasurfaces constructed from hexagonal-ring units along with honeycomb lattice are proposed for the efficient generation of converged orbital angular momentum (OAM) waves. The proposed unit has a very succinct structure constructed from a hexagonal-ring patch along with a hexagonal metallic reflector, which could achieve a polarization-insensitive response to the incident waves, when binding further with the hexagonal lattice. Through the topology optimization of the unit arrangement, two reflective metasurfaces stimulating the first-order and the second-order OAM beams are numerically designed, which may find useful in radio communications and radar applications.

Keywords: OAM, metasurface, reflective, hexagonal-ring, polarization-insensitive

INTRODUCTION

Since the first exploration by Allen et al., orbital angular momentum (OAM) has displayed its independent value in many interdisciplinary fields and has become one of the most important research frontiers in modern technologies [1]. Recently, OAM has been thoroughly studied and widely understood as a promising candidate for information multiplexing to increase the spectral efficiency in microwave domain [2], and the capacity of the wireless communication systems can thus be largely extended [3, 4]. Many researches have then been conducted for stimulating OAM waves, which can generally be split into two categories, the microwave antenna method [5–11] and the physical optics method [12–23].

One of the most elegant approach to stimulate OAM for microwave antenna method is based on high-order mode patch antenna [5]. For example, dual circularly polarized (CP) dual-mode vortex OAM beams were succinctly generated by exciting the second-order resonance modes on a single patch antenna, which is with very compact structure and much suitable for low-cost OAM applications [6]. For more flexible multi-mode OAM modulation, circular phased array systems are constructed to provide the successive phase shifts in elements [7]. The dual-mode OAM operation was realized in a four-element array by employing the opposite phase differences created for left-handed CP and right-handed CP incidences, where the four dual-CP elements are sequentially rotated [8]. To stimulate more OAM modes associated with multi-polarization operation, circular horn array using elements with three polarizations was realized by introducing the phase control networks, which can be very costly and complicated [9]. For the low-cost multi-mode OAM operation, Rotman lens was introduced to simplify the feed network for the phased array [10], and later combined with Fabry-Perot resonant cavity to improve the beam divergence for different OAM modes [11]. Major drawbacks with such microwave antenna methods are that versatile modulations of mixed or multi-OAM modes in different propagation directions are hardly achieved.

In-depth research and exploration based on physical optics theory have been devoted to stimulate OAM beams through the wavefront transformation of the spherical or plane waves, including the dielectric spiral plate [12], discrete spiral reflector [13], and twisted parabolic reflector [14], whose structures are all very ponderous and enormous in real applications. Recently, metasurfaces have been widely researched for the independent talent of delicate regulation on electromagnetic waves [15–17], which also draw significant attention as a promising realization approach for OAM generation in physical optics method [18–26]. High-efficiency reflective and transmissive metasurfaces with various topological forms have been proposed for vortex OAM generation in linear polarization [18–20]. For the converging OAM radiation with CP waves, broadband transmissive metasurfaces based on Pancharatnam–Berry phase or photon spin Hall effect have been efficiently demonstrated [21–24]. Recently, to improve the isotropy and spatial coverage property of the metasurfaces, polarization-insensitive transmissive metasurfaces with honeycomb lattice or rotational symmetry arrangement are proposed to create converging OAM beams for fully polarized applications [25, 26], which are troubled with the complex design along with the complicated configurations.

In this paper, we propose the design of polarization-insensitive reflective metasurfaces with very succinct units along with a honeycomb lattice for the efficient generation of converging OAM waves. The proposed units are constructed from hexagonal-ring patches along with hexagonal metallic reflectors, which could obtain a full-polarization response of the incident wave, when binding further with the hexagonal lattice. Through the topology optimization of the unit arrangement, the reflective metasurfaces stimulating the first-order and the second-order OAM beams are numerically demonstrated.

FIGURE 1 | Metasurface unit architecture and numerical simulations. **(A)** Exploded view of the hexagonal unit on top and the reflective metasurface at bottom. **(B)** Simulated reflection coefficient for the eight representative units at 7.5 GHz. **(C)** Simulated reflection phase spectra of Unit 4 for different incident angles. **(D)** Simulated reflection phase spectra of Unit 4 for orthogonal linear polarizations in normal incidence ($\theta = 0°$).

HEXAGONAL UNIT DESIGN

Figure 1A presents the architecture of the hexagonal units in the metasurface, which have a very succinct structure and composed of two metal layers supported by a substrate layer. The numerical simulations of the units are carried out with the support of CST Microwave Studio Software by using unit-cell boundary conditions along with the Floquet-port excitations. The substrate layer has a dielectric constant of 3.66, a dissipation factor of $\tan \delta = 0.0037$, and a thickness of $h = 1.524$ mm. The unit is a hexagonal structure with a periodic side length $R = 8$ mm, corresponding to a central working frequency $f = 7.5$ GHz. The upper hexagonal-ring patch serves as the phase-shift metasurface, while the lower metal ground layer plays the role of the metallic reflector. The reflective phase modulation of the units can be achieved by varying the outer side length r_o of the hexagonal-ring patch, while the inner side length r_i remains constant.

Based on the former study on the phase-quantization effects for the metasurface lens, the quantization loss for the typical 3-bit metasurfaces is only 0.2 dB, which is within the scope of acceptable [25]. Eight representative units are thus selected for the construction of the honeycomb reflectarray to minimize the reflection losses and acquire the high-linearity phase-shift range of 2π, as shown in **Figure 1B**. Almost complete reflections have been obtained for all eight representative units, along with the full 2π phase modulation. All the optimized parameters for the designed representative units are provided in **Figure 1**.

Figure 1C presents the simulated reflection phase spectra of Unit 4 for different incident angles as representative, and the phase shift has relatively minor change while varying the incidence angle, implying that the hexagonal unit possesses a good spatial coverage property. **Figure 1D** shows the simulated phase spectrum in reflection coefficient of Unit 4 for orthogonal linear polarizations as representative, and

FIGURE 2 | Reflective metasurface for OAM mode $l = +1$. **(A)** Quantized phase distributions for the units. **(B)** Topological structure of the metasurface. **(C)** The amplitude pattern of the simulated far-field radiation. **(D)** The phase pattern of the simulated far-field radiation.
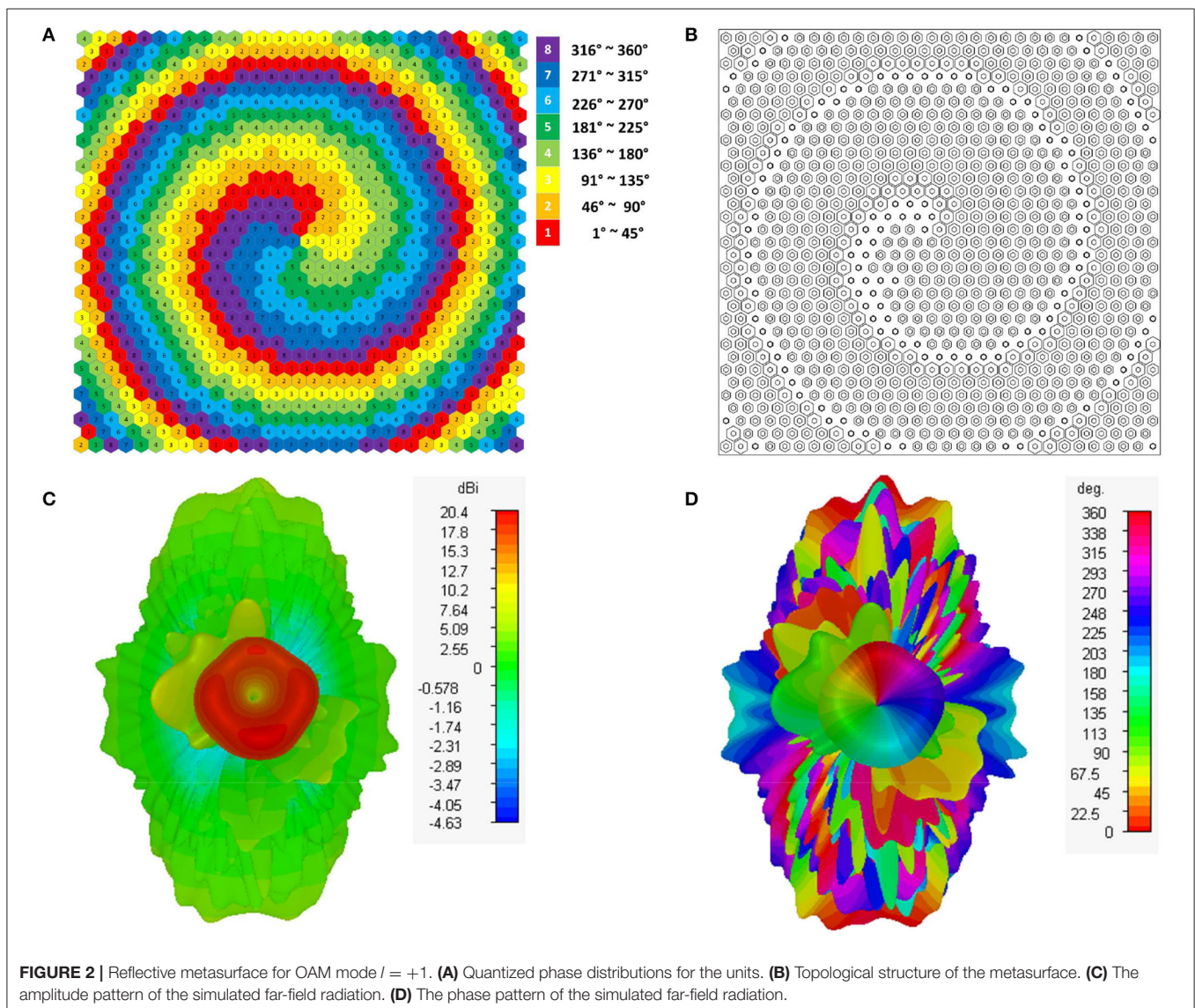
almost no phase shifts could be observed for the two different polarizations, implying that the hexagonal unit possesses good polarization-insensitive characteristic.

METASURFACES CONFIGURATION AND VERIFICATION

The proposed reflective metasurfaces are constructed with the honeycomb lattice by using 974 hexagonal units, and a standard waveguide horn is positioned in the metasurface central axis as the space feed source, as shown in **Figure 1A**. To improve the beam divergence and obtain the convergent OAM beams through the proposed reflective metasurfaces, the theoretical phase modulation ϕ for the metasurface units should be designed to meet the equation below [27]:

$$\phi = 2\pi \left(\sqrt{(x^2+y^2)+F^2} - F \right) / \lambda + l \cdot \arctan(y/x) \quad (1)$$

Here l is the designed OAM mode number, (x, y) are the unit position coordinates, λ is the free-space wavelength, and F is the focal length of the feed antenna and set as $F = 8\lambda = 320$ mm.

To stimulate the OAM wave with mode number $l = +1$, the required phase-shift distribution for all the units are designed using Equation (1) and performed as shown in **Figure 2A**. The corresponding topological structure of the honeycomb metasurface is provided in **Figure 2B**, which clearly exhibits a single spiral configuration. **Figure 2C** presents the amplitude pattern of the simulated far-field radiation of the honeycomb metasurface for OAM mode number $l = +1$, where an annular tapered pattern of high-intensity radiation is clearly revealed. The side lobes are much lower than the main lobe, indicating that the electromagnetic energy is mainly propagating with the OAM
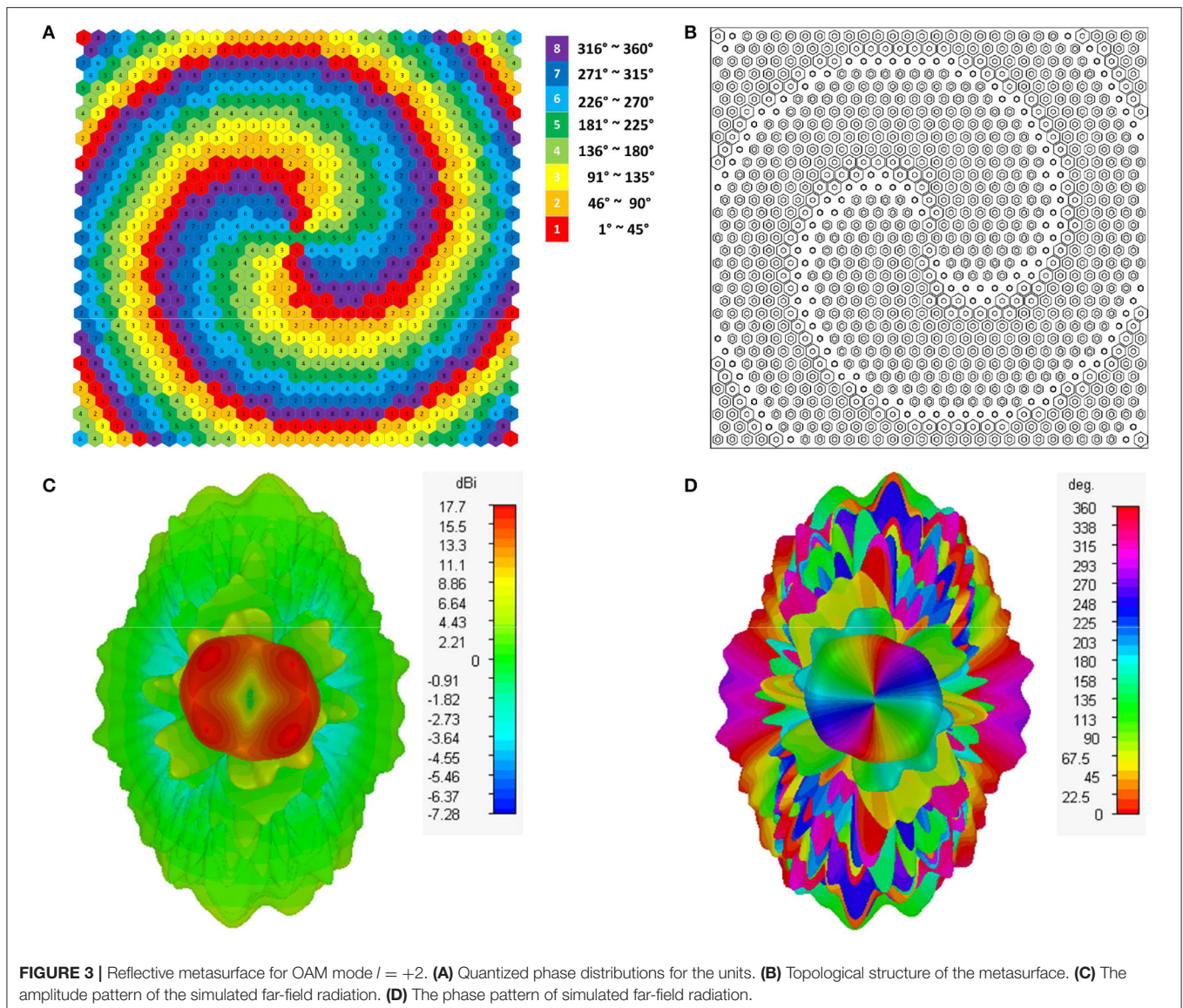

FIGURE 3 | Reflective metasurface for OAM mode $l = +2$. **(A)** Quantized phase distributions for the units. **(B)** Topological structure of the metasurface. **(C)** The amplitude pattern of the simulated far-field radiation. **(D)** The phase pattern of simulated far-field radiation.

wave. The corresponding phase pattern of the simulated far-field radiation is also plotted in **Figure 2D**, where the characteristic spiral phase front along with on-axis phase singularity of OAM are clearly revealed. The phase distribution of the OAM waves undergoes a linear variation of 2π around the axis of propagation, indicating the creation of a vortex beam with OAM mode $l = +1$.

For the OAM mode with number $l = +2$, the required phase-shift distributions are provided in **Figure 3A**, along with the corresponding metasurface structure shown in **Figure 3B**, both clearly exhibiting the double-helix configuration. **Figures 3C,D** present the amplitude and phase patterns of the simulated far-field radiation for OAM $l = +2$, respectively. The high-intensity annular tapered patterns along with the characteristic spiral phase fronts as well as on-axis phase singularity are clearly exhibited. The phase distribution undergoes a linear variation of 4π around the axis of propagation, indicating the creation of a vortex beam with OAM mode $l = +2$.

CONCLUSION

In summary, polarization-insensitive reflective metasurfaces constructed from hexagonal-ring units along with honeycomb lattice have been proposed for efficient converging OAM generation. The proposed unit is made of a very succinct structure that binds further with the hexagonal lattice for obtaining a full-polarization response to the incident wave. Through the topology optimization of the units, two reflective metasurfaces stimulating the first-order and the second-order OAM beams have been numerically verified, which could be a promising candidate for radio communications and radar applications.

DATA AVAILABILITY STATEMENT

The raw data supporting the conclusions of this article will be made available by the author, without undue reservation.

AUTHOR CONTRIBUTIONS

XB designed and performed the design and simulation as well as wrote the paper.

FUNDING

REFERENCES

1. Allen L, Beijersbergen MW, Spreeuw RJC, Woerdman JP. Optical angular momentum of light and the transformation of Laguerre-Gauss laser modes. *Phys Rev A.* (1992) **45**:8185–9. doi: 10.1103/PhysRev A.45.8185

2. Thidé B, Then H, Sjöholm J, Palmer K, Bergman J, Carozzi TD, et al. Utilization of photon orbital angular momentum in the low-frequency radio domain. *Phys Rev Lett.* (2007) **99**:087701. doi: 10.1103/PhysRevLett.99.087701

3. Hu T, Wang Y, Liao X, Zhang J, Song Q. OFDM-OAM modulation for future wireless communications. *IEEE Access.* (2019) **7**:59114–25. doi: 10.1109/ACCESS.2019.2915035

4. Guo Z, Yang G. Radial uniform circular antenna array for dual-mode OAM communication. *IEEE Anten. Wireless Propag. Lett.* (2017) **16**:404–7. doi: 10.1109/LAWP.2016.2581204

5. Barbuto M, Trotta F, Bilotti F, Toscano A. Circular polarized patch antenna generating orbital angular momentum. *Prog Electromagn Res.* (2014) **148**:23–30. doi: 10.2528/PIER14050204

6. Bai X, Liang X, Li M, Zhou B, Geng J, Jin R. Dual-circularly polarized conical-beam microstrip antenna. *IEEE Anten Wireless Propag Lett.* (2015) **14**:482–5. doi: 10.1109/LAWP.2014.2369515

7. Mohammadi SM, Daldorff LKS, Bergman JES, Karlsson RL, Thidé B, K. Forozesh, et al. Orbital angular momentum in radio-a system study. *IEEE Trans Antennas Propag.* (2010) **58**:565–72. doi: 10.1109/TAP.2009.2037701

8. Bai X, Liang X, Sun Y, Hu P, Yao Y, K. Wang, et al. Experimental array for generating dual-circularly polarized dual-mode OAM radio beams. *Sci Rep.* (2017) **7**:40099. doi: 10.1038/srep40099

9. Bai X, Jin R, Liu L, Geng J, Liang X. Generation of OAM radio waves with three polarizations using circular horn antenna array. *Int J Anten Propag.* (2015) **2015**:132549. doi: 10.1155/2015/132549

10. Bai X, Liang X, Li J, Wang K, Geng J, Jin R. Rotman lens-based circular array for generating five-mode OAM radio beams. *Sci. Rep.* (2016) **6**:27815. doi: 10.1038/srep27815

11. Bai X, Cao A, Kong F, Qian J, Xu S, Yan W, et al. Rotman lens-fed Fabry-Perot resonator antennas for generating converged multi-mode OAM beams. *IEEE Access.* (2019) **7**:105768–75. doi: 10.1109/ACCESS.2019.2932199

12. Niemiec R, Brousseau C, Emile O, Ménard A. Characterization of an OAM flat-plate antenna in millimetre frequency band. *IEEE Anten Wireless Propag Lett.* (2014) **13**:1011–4. doi: 10.1109/LAWP.2014.2326525

13. Tamburini F, Mari E, Thidé B, Barbieri C, Romanato F. Experimental verification of photon angular momentum and vorticity with radio techniques. *Appl Phys Lett.* (2011) **99**:204102. doi: 10.1063/1.3659466

14. Mari E, Spinello F, Oldoni M, Ravanelli RA, Romanato F, Parisi G. Near-field experimental verification of separation of OAM channels. *IEEE Antennas Wireless Propag Lett.* (2015) **14**:556–8. doi: 10.1109/LAWP.2014.2369536

15. Li A, Singh S, Sievenpiper D. Metasurfaces and their applications. *Nanophotonics.* (2018) **7**:989–1011. doi: 10.1515/nanoph-2017-0120

16. Glybovski SB, Tretyakov SA, Belov PA, Kivshar YS, Simovski CR. Metasurfaces: From microwaves to visible. *Phys Rep.* (2016) **634**:1–72. doi: 10.1016/j.physrep.2016.04.004

17. Li A, Li Y, Long J, Forati E, Du Z, D. Sievenpiper. Time-moduated nonreciprocal metasurface absorber for surface waves. *Opt Lett.* (2020) **45**:1212–5. doi: 10.1364/OL.382865

18. Yu S, Li L, Shi G, Zhu C, Zhou X, Shi Y. Design, fabrication, and measurement of reflective metasurface for orbital angular momentum vortex wave in radio frequency domain. *Appl Phys Lett.* (2016) **108**:121903. doi: 10.1063/1.4944789

19. Akram MR, Ding G, Chen K, Feng Y, Zhu W. Ultra-thin single layer metasurfaces with ultra-wideband operation for both transmission and reflection. *Adv Mater.* (2020) **32**:1907308. doi: 10.1002/adma.201907308

20. Chen Y, Zheng S, Li Y, Hui X, Jin X, H. Chi, et al. A flat-lensed spiral phase plate based on phase-shifting surface for generation of millimeter-wave OAM beam. *IEEE Anten Wireless Propag Lett.* (2016) **15**:1156–8. doi: 10.1109/LAWP.2015.2497243

21. Akram MR, Bai X, Jin R, Vandenbosch GAE, Premaratne M, Zhu W. Photon spin Hall effect based ultra-thin transmissive metasurface for efficient generation of OAM waves. *IEEE Trans Antennas Propag.* (2019) **67**:4650–8. doi: 10.1109/TAP.2019.2905777

22. Xu H, Liu H, Ling X, Sun Y, Yuan F. Broadband vortex beam generation using multimode Pancharatnam–Berry metasurface. *IEEE Trans Antennas Propag.* (2017) **65**:7378–82. doi: 10.1109/TAP.2017.2761548

23. Zhang K, Yuan Y, Zhang D, Ding X, Ratni B, S. Burokur, et al. Phase-engineered metalenses to generate converging and non-diffractive vortex beam carrying orbital angular momentum in

microwave region. *Opt Express.* (2018) **26**:1351–60. doi: 10.1364/OE.26.0 01351

24. Akram MR, Mehmood MQ, Bai X, Jin R, Premaratne M, Zhu W. High efficiency ultra-thin transmissive metasurfaces. *Adv Opt Mater.* (2019) **7**:1801628. doi: 10.1002/adom.201801628

25. Bai X, Kong F, Qian J, Song Y, He C, Liang X, et al. Polarization-insensitive metasurface lens for efficient generation of convergent OAM beams. *IEEE Antennas Wireless Propag Lett.* (2019) **18**:2696–700. doi: 10.1109/LAWP.2019.2949085

26. Akram M, Mehmood M, Tauqeer T, Rana A, Rukhlenko I, Zhu W. Highly efficient generation of Bessel beams with polarization insensitive metasurfaces. *Opt Express.* (2019) **27**:9467–80. doi: 10.1364/OE.27.0 09467

27. Qin F, Wan L, Li L, Zhang H, Wei G, Gao S. A transmission metasurface for generating OAM beams. *IEEE Antennas Wireless Propag Lett.* (2018) **17**:1793–6. doi: 10.1109/LAWP.2018.2867045

Construction of a Cost-Effective Phased Array Through High-Efficiency Transmissive Programable Metasurface

Anjie Cao[1,2]*, Zhansheng Chen[1], Kai Fan[1], Yuehui You[1] and Chong He[2]

[1] R&D center, Shanghai Institute of Satellite Engineering, Shanghai, China, [2] Department of Electronic Engineering, Shanghai Jiao Tong University, Shanghai, China

Programmable metasurfaces have shown great potential in the areas of low-complexity phase array systems in comparison with the conventional phased array antennas. In this document, a 1-bit transmissive programable metasurface with high efficiency is proposed for the cost-effective beam-steering phased array. The designed transmissive metasurface is made up of reconfigurable cells with perfect 1-bit phase tuning and less transmission losses. Through dynamically programming the 1-bit code distributions of the metasurface, real-time scanning pencil beams in desired directions can be created.

Keywords: metasurface, programmable, phased array, cost-effective, transmissive

INTRODUCTION

Recently, metasurfaces are widely known as a kind of two-dimensional periodic structures with subwavelength scale, owing to its independent talent of delicate modulation on electromagnetic waves [1]. Based on the advantages of low loss, easy integration and simple preparation, metasurfaces have shown extensive application prospects and become a research hotspot in modern physics, information science and the related interdisciplinary [2–4].

Within microwave domain, metasurfaces also arouse a wide range of investigation, such as radiation improvement [5–7], perfect absorbers [8, 9], OAM-EM wave generation [10–13], scattering reduction [14–16], holographic imaging [17, 18], and energy harvesting [19]. Metasurfaces particularly demonstrate the unique abilities in waveform shaping through the phase manipulation of the building units in microwave metasurfaces. Reflective metasurfaces were demonstrated to generate the high-intensity pencil beams or high-purity vortex waves through the full 2π phase tuning [20, 21]. Polarization-insensitive transmissive metasurface with hexagonal unit configuration is proposed to stimulate vortex beam at any polarization [22]. The ultra-thin transmissive metasurfaces were designed for high-efficiency wavefront modulation in circular polarization, based on photon spin Hall effect or Pancharatnam-Berry phase theory [23, 24]. Nevertheless, for all the foregoing designs, only the fixed directional or shaped beams can be created once the metasurfaces are constructed, which restrict the application for dynamic control in electromagnetic wave.

The programmable metasurfaces integrated with lumped components could be very practical for the fine-grained modulation over electromagnetic waves, which also show great advantages at improving the incomplexity and cost for dynamic beam forming or scanning, in comparison with conventional phased array systems that are composed of massive digital or analog phase shifters [25]. Digital or programmable metamaterials are firstly proposed in 2014 to expand the concept of metamaterials by using dynamic sequences of "0" and "1" bits [26]. Ulteriorly, the metasurface unit

FIGURE 1 | Topological configuration of the proposed transmissive metasurface (all dimensions are in millimeters) **(A)** Exploded view of the 1-bit cell on top along with the metasurface at bottom **(B)** Transmitting layer **(C)** Bias layer **(D)** Receiving layer.
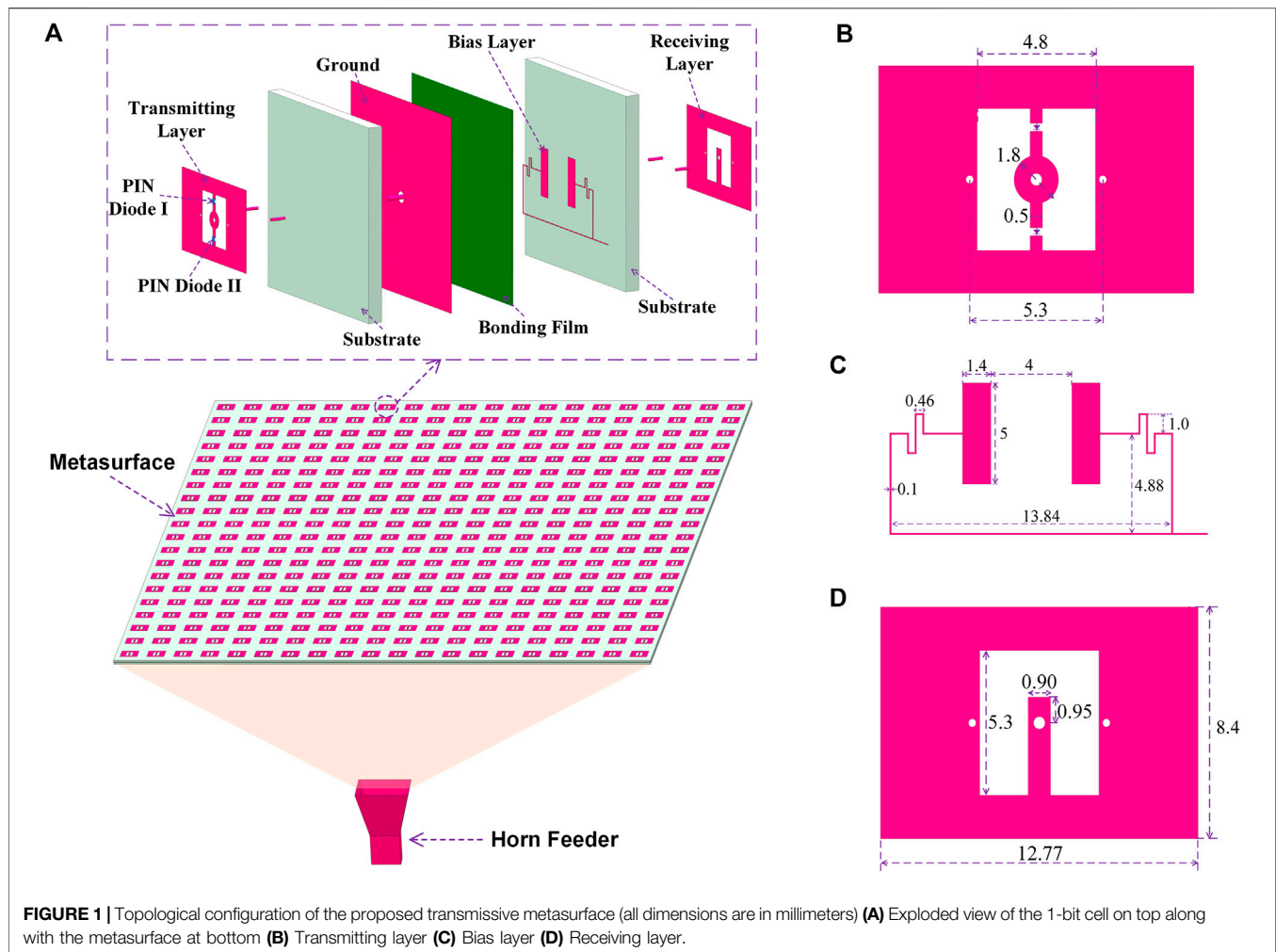
can obtain a clear alteration in resonant property through integrating lumped components, and the programmable reflective metasurfaces are thus actually constructed for the dynamic modulation of the electromagnetic waves [27]. The digital reflective metasurfaces were constructed by designing reconfigurable cells combined with the PIN diodes for binary phase states [28, 29]. Later, two-bit reflective programable metasurfaces were designed by integrating two PIN diodes or a voltage-controlled varactor diode to modulate the resonant characteristics of the reconfigurable units [30, 31]. Since the feed shielding effects and the phase distortions are usually very serious for the reflective metasurfaces, the programmable transmissive metasurfaces are then proposed to avoid these deficiencies [32]. Metasurface unit integrated with C-shaped patch and U-shaped slot serving as the receiver and transmitter was designed to construct the digital transmissive metasurface [33]. Metasurface unit with the combination of a couple of C-shaped patches and ring slots was adopted to achieve 1-bit phase resolution [34]. Later, the equivalent magnetic dipole unit was also presented by combining the rectangular patch and side-shorted patch [35]. However, all these transmissive metasurfaces are suffering from very high transmission losses due to the

insufficient unit architecture design, which lead to the low aperture efficiency not exceeding 20.0%.

In this document, a high-efficiency transmissive 1-bit digital metasurface is designed for the construction of the cost-effective phased array. Through dynamically programming the 1-bit code distributions of the metasurface when biasing the integrated PIN diodes, real-time scanning pencil beams in the desired directions can be created and the numerical simulation results demonstrate the availability of the proposed metasurface.

UNIT DESIGN AND CONFIGURATION

The component of the designed transmissive programable metasurface is a reconfigurable programmable cell with binary phase modulation. The 1-bit unit is constructed with multilayer metallic structure along with two dielectric substrates and a bonding film, the structure of which is shown in **Figure 1A**. The two dielectric substrates have the same parameters with the dielectric constant of 3.55 and the thickness of 1.524 mm, and the thickness of the bonding film is 0.1 mm. The metallic structure is composed of the transmitting patch, the ground plane, the bias

FIGURE 2 | Simulated scattering parameters of the proposed metasurface cell (A) Magnitude for both $\pi/0$-states (B) Phases for both $\pi/0$ states.
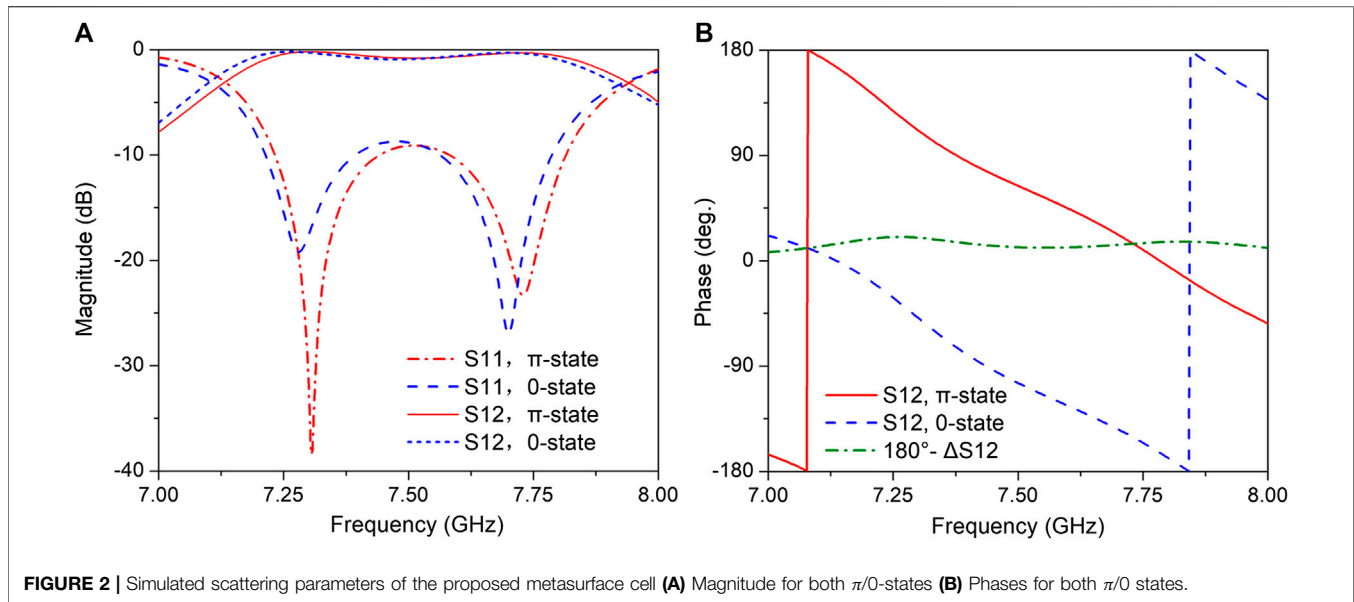
layer and the receiving patch. The transmitting patch is designed in front with a rectangular patch loaded by an O-slot and two PIN diodes, while the same-sized receiving patch is set on the reverse side and integrated by an U-slot, and the two patches constitute an integral whole by a metallized central via-hole through the ground. In addition, the transmitting patch is connected with the ground through a pair of symmetric via-holes, while the receiving patch is connected with a pair of rectangular distributed capacitors in the bias layer in similar way for biasing purpose. To reduce the influence of the bias lines on the designed unit, the bias lines are designed using extremely narrow linewidths and located near the ground plane. Detailed structure and dimensions of the proposed metasurface cell are also given in **Figure 1**.

The PIN diode M/A-COM Flip Chip MA4FCP305 is chosen to construct and modulate the unit, and the parameter modelling of the PIN diode is characterized as lumped components for the binary ON/OFF states [36]. When biasing the PIN diode with a forward current, the ON state along with a series of a resistance $R_{ON} = 2.1\ \Omega$ would be employed; and for a reverse bias voltage, the OFF state along with a parallel of a capacitance $C_{OFF} = 0.05$ pF would be applied for the PIN diode. The 1-bit phase modulation of the unit can be accomplished through biasing the integrated PIN diodes. The simulated scattering parameters of the designed metasurface cell are plotted in magnitude and phase for both $\pi/0$ states, as shown in **Figure 2**. When PIN diode I is at the ON state and PIN diode II is at the OFF state, the metasurface cell would be operating at the π-state; the simulated S_{11} is less than –10 dB from 7.23 to 7.82 GHz, and the simulated S_{12} is above –2 dB from 7.17 to 7.89 GHz. When PIN diode I is at the OFF state and PIN diode II is at the ON state, the metasurface cell would be working at the 0-state; now the simulated S_{11} is less than –10 dB from 7.21 to 7.79 GHz, and the simulated S_{12} is above –2 dB from 7.13 to 7.86 GHz. The phase displacement of the binary cell states could maintain constant at nearby π with relatively small variations.

METASURFACE CONFIGURATION AND BEAM-SCANNING VERIFICATION

In the actual metasurface design, the transmissive programable metasurface is constructed with 400 units and an overall dimension of 400×400 mm^2, and the overall structure of the designed metasurface is also shown in **Figure 1A**. The focal source of a standard waveguide horn is placed in front of the

FIGURE 3 | Spatially-fed geometry and the relevant vector coordinates.
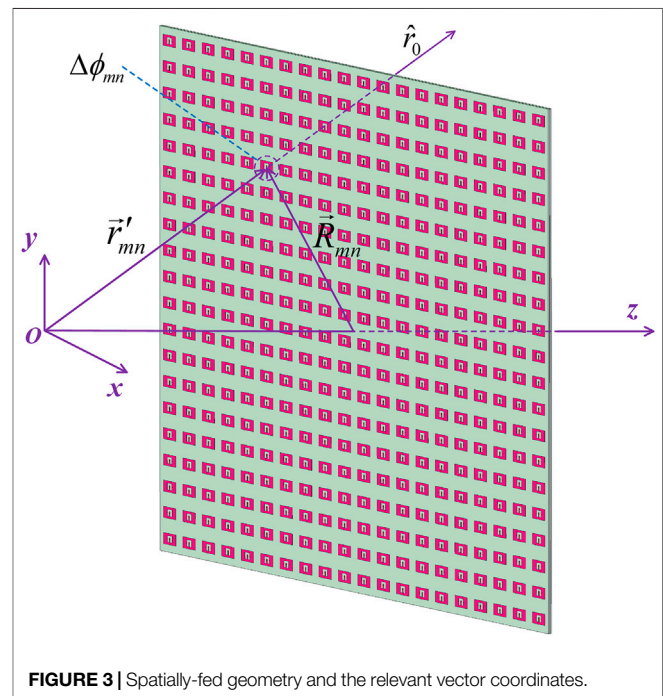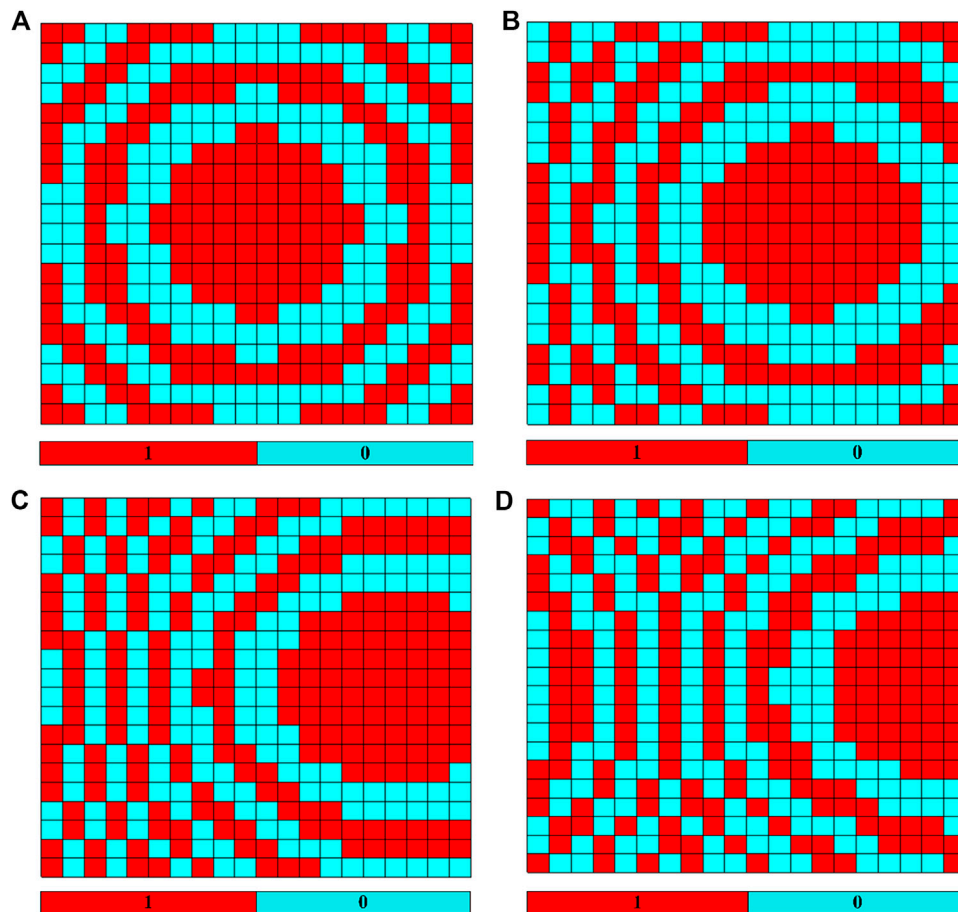
FIGURE 4 | Optimal quantized phase code distributions for four beam directions **(A)** $\theta = 0°$ **(B)** $\theta = 15°$ **(C)** $\theta = 30°$ **(D)** $\theta = 45°$.

central axis of the metasurface with a focal length of F = 5λ = 200 mm, and the cells on the metasurface serve as the 1-bit phase shifters for the incoming wave and are modulated through the bias layer.

To generate a scanning pencil beam in the desired direction, the phase compensation $\Delta\phi_{mn}$ for the metasurface cells should satisfy the formula,

$$k_0\left(r'_{mn} - \overrightarrow{R}_{mn} \cdot \hat{r}_0\right) - \Delta\phi_{mn} = 2n\pi \quad n \in Z \tag{1}$$

where k_0 is the wavenumber, $\overrightarrow{r}'_{mn}$ is the position vector of the mnth unit, $\overrightarrow{R}_{mn}$ is the position vector of the mnth unit relative to $(0, 0, f)$, and $\hat{r}_0$ is the desired direction of the pencil beam. All these parameters are defined as shown in **Figure 3**.

To get the overall code distribution on the metasurface, the binary phase states for each unit could be obtained by furtherly quantizing the continuous phase shift $\Delta\phi_{mn}$,

$$\phi_Q = \begin{cases} 0, & \Delta\phi_{mn} \in [0 + 2n\pi, \pi + 2n\pi) \\ \pi, & \Delta\phi_{mn} \in [\pi + 2n\pi, 2\pi + 2n\pi) \end{cases} \quad n \in Z \tag{2}$$

To further validate the effectiveness of the transmissive programmable metasurface, steering pencil beams with a wide scanning range of at least 45° and an angular spacing of 15° are

then numerically generated. The optimal quantized code distributions for the four directional beams are generated using **Equation (2)** and implemented as shown in **Figure 4**, which can be simply controlled by the modulation of the ON/OFF states of the PIN diodes. The simulated far-field radiation patterns for the scanning pencil beams in four directions are plotted in **Figure 5**. For the broadside radiation, a directional beam is obtained with a simulated gain over 25.3 dB, corresponding to an aperture efficiency over 27% by using the following definition:

$$\eta = \frac{G}{4\pi A \big/ \lambda^2} \tag{3}$$

where G is the simulated gain and A is the metasurface aperture area. When furtherly considering the quantization loss of about 3 dB for a typical 1-bit phase resolution, the metasurface aperture efficiency could be expected to exceed 50% theoretically. As the scanning angle of the steering beam increases, the main-lobe maximum gain would decrease due to the diminution of the effective metasurface aperture area, which is in accordance with the traditional phased array antenna. For all the four directional scanning beams, the side-lobe levels are −10 dB lower than that of the main lobes.
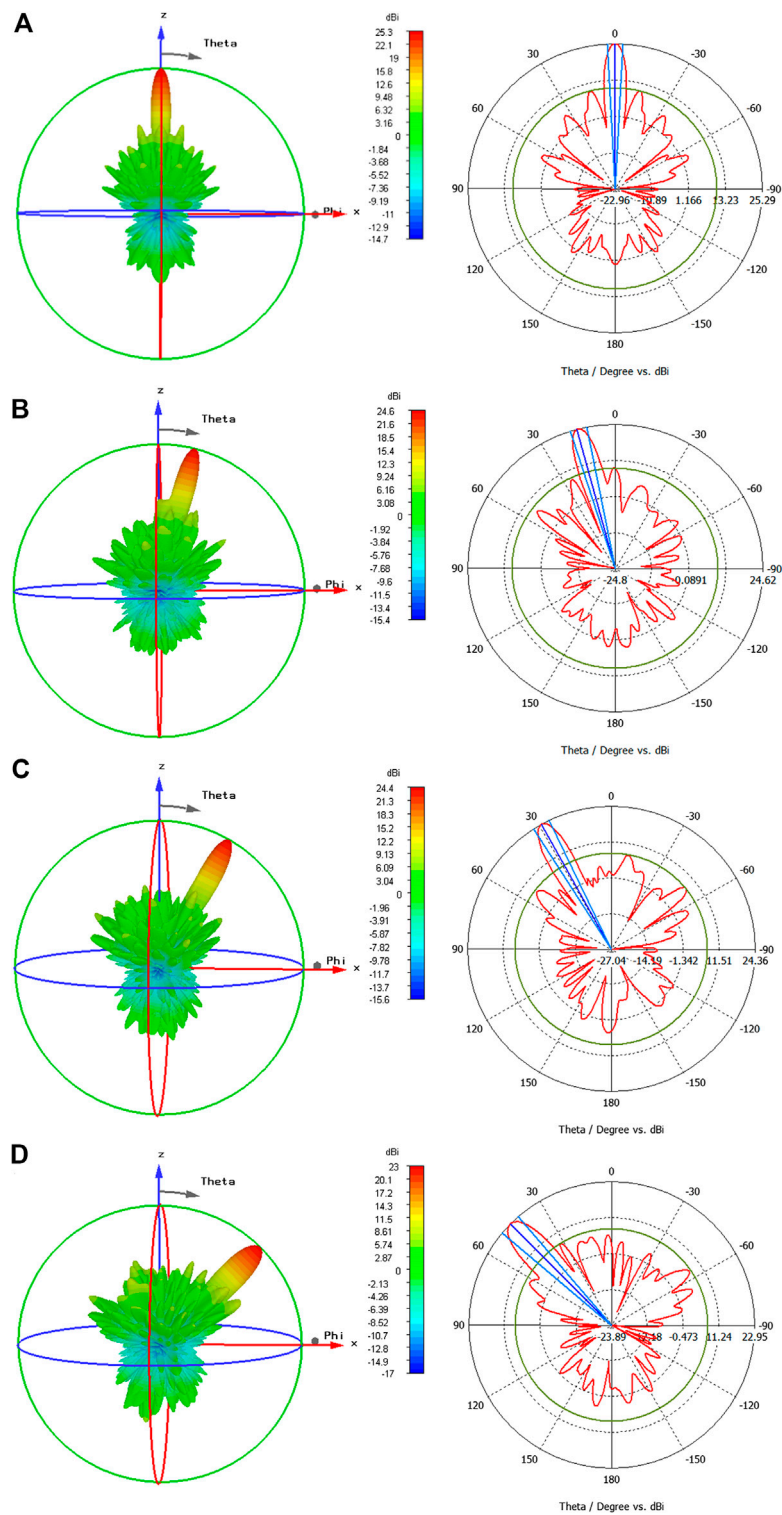
FIGURE 5 | Simulated 3-D and 2-D far-field radiation patterns for four beam directions **(A)** $\theta = 0°$ **(B)** $\theta = 15°$ **(C)** $\theta = 30°$ **(D)** $\theta = 45°$.

CONCLUSION

In summary, a high-efficiency transmissive programable metasurface with 1-bit phase modulation is presented for the construction of a cost-effective phased array. The expected performances with real-time dynamic scanning beams are investigated, and scanning pencil beams in four directions with low side-lobe levels are generated through dynamically programming the 1-bit code distributions on the metasurface, which verify the effectiveness of the presented transmissive programable metasurface design.

DATA AVAILABILITY STATEMENT

The original contributions presented in the study are included in the article, further inquiries can be directed to the corresponding author.

AUTHOR CONTRIBUTIONS

AC, ZC, KF, YY, and CH designed and performed the research as well as wrote the paper.

REFERENCES

1. Li A, Singh S, Sievenpiper D. Metasurfaces and their applications. *Nanophotonics* (2018) 7:989–1011. doi:10.1515/nanoph-2017-0120
2. He Q, Sun S, Xiao S, Zhou L. High-effiiency metasurfaces: principles, realizations, and applications. *Adv Opt Mater* (2018) 6:1800415. doi:10.1002/adom.201800415
3. Li Z, Premaratne M, Zhu W. Advanced encryption method realized by secret shared phase encoding scheme using a multiwavelength metasurface. *Nanophotonics* (2020) 9:3687. doi:10.1515/nanoph-2020-0298
4. Li A, Li Y, Forati E, Kim S, Lee J, Long J, et al. Direct conversion of static voltage to a steerable RF radiation beam using an active metasurface. *IEEE Trans Antennas Propag* (2020) 68:1680–8. doi:10.1109/TAP.2019.2934903
5. Bai X, Cao A, Kong F, Qian J, Xu S, Yan W, et al. Rotman lens-fed Fabry–Perot resonator antennas for generating converged multi-mode OAM beams. *IEEE Access* (2019) 7:105768–75. doi:10.1109/ACCESS.2019.2932199
6. Raeker BO, Rudolph SM. Arbitrary transformation of antenna radiation using a cylindrical impedance metasurface. *Antennas Wirel Propag Lett* (2016) 15:1101–4. doi:10.1109/LAWP.2015.2494739
7. Sun J, Chen K, Ding G, Guo W, Zhao J, Feng Y, et al. Achieving directive radiation and broadband microwave absorption by an anisotropic metasurface. *IEEE Access* (2019) 7:93919–26. doi:10.1109/ACCESS.2019.2928839
8. Li A, Li Y, Long J, Forati E, Du Z, Sievenpiper D. Time-moduated nonreciprocal metasurface absorber for surface waves. *Opt Lett* (2020) 45:1212–5. doi:10.1364/OL.382865
9. Li A, Kim S, Luo Y, Li Y, Long J, Sievenpiper DF. High-power transistor-based tunable and switchable metasurface absorber. *IEEE Trans Microw Theor Tech* (2017) 65:2810–8. doi:10.1109/TMTT.2017.2681650
10. Akram MR, Ding G, Chen K, Feng Y, Zhu W. Ultra-thin single layer metasurfaces with ultra-wideband operation for both transmission and reflection. *Adv Mater* (2020) 32:1907308. doi:10.1002/adma.201907308
11. Bai X, Kong F, Sun Y, Wang G, Qian J, Li X, et al. High-efficiency transmissive programmable metasurface for multimode OAM generation. *Adv Optical Mater* (2020) 8:2000570. doi:10.1002/adom.202000570
12. Akram MR, Mehmood MQ, Bai X, Jin R, Premaratne M, Zhu W. High efficiency ultra-thin transmissive metasurfaces. *Adv Opt Mater* (2019) 7:1801628. doi:10.1002/adom.201801628
13. Bai X. High-efficiency transmissive metasurface for dual-polarized dual-mode OAM generation. *Results Phys* (2020) 18:103334. doi:10.1016/j.rinp.2020.103334
14. Zhuang Y, Wang G, Liang J, Zhang Q. Dual-band low-scattering metasurface based on combination of diffusion and absorption. *IEEE Antennas Wirel Propag Lett* (2017) 16:2606–9. doi:10.1109/LAWP.2017.2735483
15. Saifullah Y, Waqas AB, Yang G-M, Zhang F, Xu F. 4-bit optimized coding metasurface for wideband RCS reduction. *IEEE Access* (2019) 7:122378–86. doi:10.1109/ACCESS.2019.2937849
16. Liu X, Gao J, Xu L, Cao X, Zhao Y, Li S. A coding diffuse metasurface for RCS reduction. *IEEE Antennas Wirel Propag Lett* (2017) 16:724–7. doi:10.1109/LAWP.2016.2601108
17. Yurduseven O, Marks DL, Gollub JN, Smith DR. Design and analysis of a reconfigurable holographic metasurface aperture for dynamic focusing in the Fresnel zone. *IEEE Access* (2017) 5:15055–65. doi:10.1109/ACCESS.2017.2712659
18. Ramalingam S, Balanis CA, Birtcher CR, Shaman HN. Polarization-diverse holographic metasurfaces. *IEEE Antennas Wirel Propag Lett* (2019) 18:264–8. doi:10.1109/LAWP.2018.2888811
19. Amer AAG, Sapuan SZ, Nasimuddin N, Alphones A, Zinal NB. A comprehensive review of metasurface structures suitable for RF energy harvesting. *IEEE Access* (2020) 8:76433–52. doi:10.1109/ACCESS.2020.2989516
20. Bai X. Polarization-insensitive reflective metasurfaces for highly efficient generation of OAM beams. *Front Physics* (2020) 8:244. doi:10.3389/fphy.2020.00244
21. Akram Z, Li X, Qi Z, Aziz A, Yu L, Zhu H, et al. Broadband high-order OAM reflective metasurface with high mode purity using subwavelength element and circular aperture. *IEEE Access* (2019) 7:71963–71. doi:10.1109/ACCESS.2019.2919779
22. Bai X, Kong F, Qian J, Song Y, He C, Liang X, et al. Polarization-insensitive metasurface lens for efficient generation of convergent OAM beams. *IEEE Antennas Wirel Propag Lett* (2019) 18:2696–700. doi:10.1109/LAWP.2019.2949085
23. Akram MR, Bai X, Jin R, Vandenbosch GAE, Premaratne M, Zhu W. Photon spin Hall effect based ultra-thin transmissive metasurface for efficient generation of OAM waves. *IEEE Trans Antennas Propag* (2019) 67:4650–8. doi:10.1109/TAP.2019.2905777
24. Akram MR, Mehmood MQ, Tauqeer T, Rana AS, Rukhlenko ID, Zhu W. Highly efficient generation of Bessel beams with polarization insensitive metasurfaces. *Optic Express* (2019) 27:9467–80. doi:10.1364/OE.27.009467
25. Liu S, Xu H-X, Zhang HC, Cui TJ. Tunable ultrathin mantle cloak via varactor-diode-loaded metasurface. *Optic Express* (2014) 22:13403–17. doi:10.1364/OE.22.013403
26. Della Giovampaola C, Engheta N. Digital metamaterials. *Nat Mater* (2014) 13:1115–21. doi:10.1038/NMAT4082
27. Liu S, Cui TJ. Concepts, working principles and applications of coding and programmable metamaterials. *Adv Opt Mater* (2017) 5:1700624. doi:10.1002/adom.20170062410.1002/adom.201700624
28. Wan X, Qi MQ, Chen TY, Cui TJ. Field-programmable beam reconfiguring based on digitally controlled coding metasurface. *Sci Rep* (2016) 6:20663. doi:10.1038/srep20663
29. Han J, Li L, Yi H, Shi Y. 1-bit digital orbital angular momentum vortex beam generator based on a coding reflective metasurface. *Opt Mater Express* (2018) 8:3470–8. doi:10.1364/OME.8.003470
30. Zhang L, Chen XQ, Shao RW, Dai JY, Cheng Q, Castaldi G, et al. Breaking reciprocity with space-time-coding digital metasurfaces. *Adv Mater* (2019) 31:1904069. doi:10.1002/adma.201904069
31. Han J, Li L, Yi H, Xue W. Versatile orbital angular momentum vortex beam generator based on reconfigurable reflective metasurface. *Jpn J Appl Phys* (2018) 57:120303. doi:10.7567/JJAP.57.120303
32. Clemente A, Dussopt L, Sauleau R, Potier P, Pouliguen P. Wideband 400-element electronically reconfigurable transmitarray in X band. *IEEE Trans Antenn Propag* (2013) 61:5017–27. doi:10.1109/tap.2013.2271493
33. Wang M, Xu S, Yang F, Hu N, Xie W, Chen Z. A novel 1-bit reconfigurable transmitarray antenna using a C-shaped probe-fed patch element with

broadened bandwidth and enhanced efficiency. *IEEE Access* (2020) 8:
120124–33. doi:10.1109/ACCESS.2020.3004435

34. Nguyen BD, Pichot C. Unit-cell loaded with PIN diodes for 1-bit linearly
polarized reconfigurable transmitarrays. *IEEE Antennas Wirel Propag Lett*
(2019) 18:98–102. doi:10.1109/LAWP.2018.2881555

35. Wang Y, Xu S, Yang F, Li M. A novel 1-bit wide-angle beam scanning
reconfigurable transmitarray antenna using an equivalent magnetic dipole
element. *IEEE Trans Antennas Propag* (2020) 68:5691–5. doi:10.1109/TAP.
2020.2964954

36. MACOM. MA4FCP305 flip chip PIN diodes, (2018) Available from: http://
cdn.macom.com/datasheets/MA4FCP305.pdf (Accessed March, 2018).

Non-Trivial Transport Interface in a Hybrid Topological Material With Hexagonal Lattice Arrangement

Lianlian Du, Yahong Liu*, Meize Li, Huiling Ren, Kun Song* and Xiaopeng Zhao

School of Physical Science and Technology, Northwestern Polytechnical University, Xi'an, China

In this paper, a hybrid topological material with hexagonal lattice arrangement is proposed, consisting of six metal cylindrical resonators and a dielectric slab. As a unit cell, the six metal cylindrical resonators satisfying the C_6 symmetry are selected, and the cylindrical resonators are inserted in the dielectric slab. It is demonstrated that a double Dirac cone is created at the Γ point in the proposed topological material. Since the topological effects of the proposed system can be invoked merely by varying the geometric parameters of the unit cell, two band gaps with different topological characteristics can be easily achieved. It is further demonstrated that the topologically protected edge states can be obtained by connecting the two types of lattices with different topological characteristics. Finally, we implement a sharp bend waveguide by using these two types of the topological lattices. It is demonstrated that electromagnetic waves can propagate robustly along the sharp bend interface.

Keywords: topological material, band gap, topological characteristics, edge states, non-trivial transport, interface

INTRODUCTION

Topological insulator is a kind of new phase of matter state about electron conductivity proposed by condensed-matter physicists. It soon becomes a hot topic in condensed matter physics and quantum materials [1, 2]. Topological insulator is realized firstly by electrons. The interior of a topological insulator is insulated, but there is always a conductive edge state on its boundary or surface. The edge state of the topological insulators is stable, and the motion direction of conducting electrons with different spins is opposite. Therefore, the transmission can be controlled by the spin of the electron, rather than transmitted by electric charge as traditional materials, and this process does not involve dissipation.

Recently, topological insulators have been extended to further areas of photonics [3–7], mechanics [8–13] and acoustics [14–21]. Topological insulators are different from conventional insulators in that the spin-orbit coupling effect of topological insulators is relatively significant. Based on the spin-orbit coupling effect, some researchers proposed a new topological crystalline insulators state [22–27]. For instance, Yang et al. proposed a chiral hyperbolic photonic metamaterial with broken inversion symmetry [26]. Ma et al. proposed a photonic topological insulator with complete topological band gap, which can emulate spin-orbit interaction through bianisotropy [27]. The quantum spin Hall effect is one of the most unique effects of topological insulators [28–31]. Wu et al. presented quantum spin Hall effect in photonic crystals [30]. Yang et al. investigated the pseudo-spin edge states for flexural waves in a honeycomb perforated phononic plate, which behaves an elastic analogue of the quantum spin Hall effect [31].
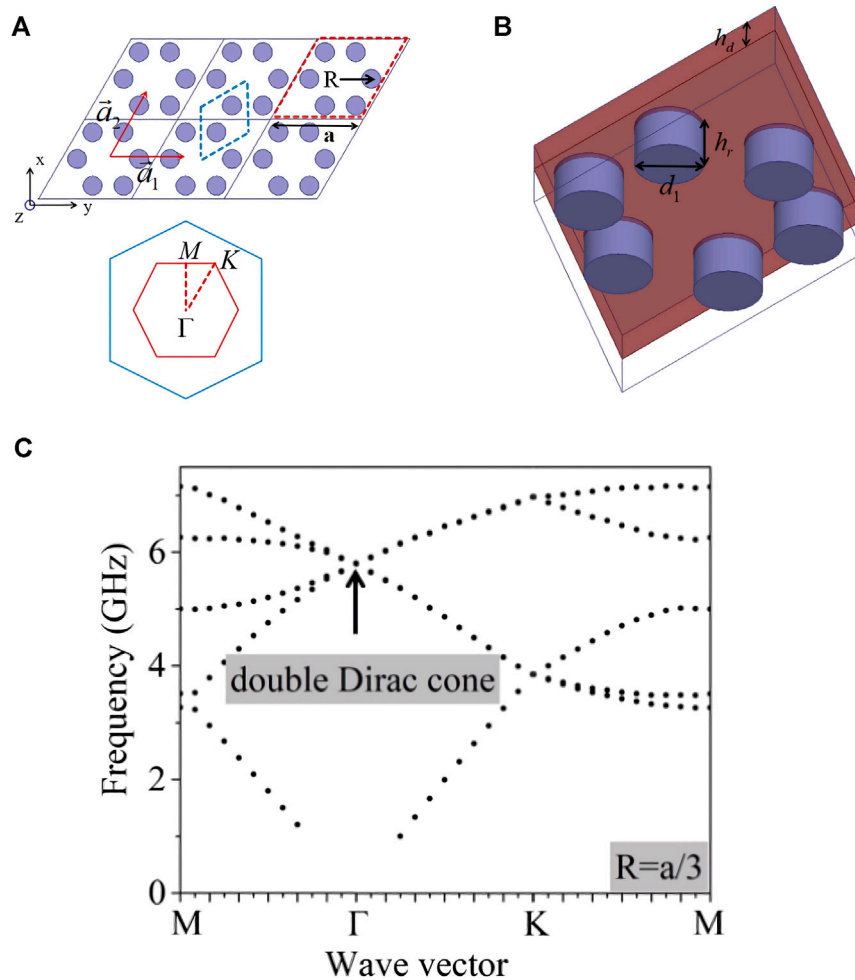
FIGURE 1 | (A) Hexagonal arrangement of the metal cylindrical resonators. The red dotted box indicates six cylindrical resonators. $\vec{a}_1$ and $\vec{a}_2$ are lattice vectors and a is the lattice length of unit cell. The blue dotted box represents the irreducible unit cell in the hexagonal arrangement. The lattice length of the irreducible unit cell is $a/\sqrt{3}$. According to the zone-folding technique, we choose a larger unit cell consisting of six resonators (red dotted box). The below panel is the corresponding Brillouin zones. **(B)** Detailed view of a hybrid unit cell consisting of six metal cylindrical resonators and a dielectric slab. The six metal cylindrical resonators are inserted into the dielectric slab. **(C)** Dispersion diagram of the proposed structure with $R = a/3$. It shows that a double Dirac cone is created at the Γ point.

Besides the quantum spin Hall effect, topological edge state has also set off a research boom. Tzuhsuan et al. proposed a photonic structure consisting of metal rods arranged as a hexagonal array lattice, and demonstrated scattering-free edge states [32]. Huo et al. proposed two-dimensional solid phononic crystal structures, which simultaneously supported the topologically protected edge states for out-of-plane and in-plane bulk elastic waves [33]. Besides metal-based topological materials, dielectric-based topological materials have also been investigated in recent years. Xu et al. proposed a triangle photonic crystal by using core-shell dielectric materials, and demonstrated a helical edge states [34]. Xie et al. proposed a second-order topological insulator in dielectric photonic crystals and visualized one-dimensional topological edge states [35]. The topologically protected edge state has excellent characteristics of robustness, back-scattering suppression and defect immunity [36–40], which have potential applications for manufacturing new computer

chips and other components in the future. In addition, topological insulators can also have been widely applied to the fields of transport in photonic crystals [41], phonon crystals [42] and even circuits composed of classical electronic components [43].

Different from the dielectric-based topological materials or metal-based topological materials presented in the previous references, in this paper, we propose a hybrid topological model consisting of metal and dielectric materials. It provides a new method to realize the topological edge state. The hybrid topological material consists of six metal cylindrical resonators and a dielectric slab. The six cylindrical resonators are inserted into the dielectric slab. The zone-folding technique [44] (using a larger unit cell instead of an irreducible one in a hexagonal crystal lattice) is applied to this present system, so that the double Dirac cone can be generated easily at the Γ point. We demonstrate that the topologically non-trivial and trivial band gaps can be opened
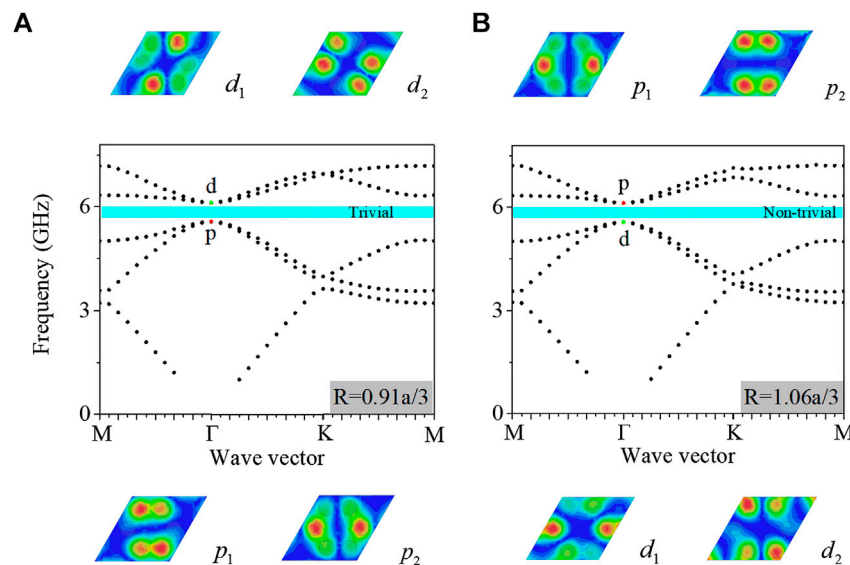
FIGURE 2 | Band structure for different R. The band gap is opened at the Γ point as R varies. **(A)** As $R = 0.91a/3$ ($R < a/3$), band gap is topologically trivial. d-type modes are at the higher frequency and p-type modes are at the lower frequency, which the electric field distributions are shown in the upper and lower illustrations of the band structure diagram, respectively. **(B)** As $R = 1.06a/3$ ($R > a/3$), the band gap is topologically non-trivial. The p-type modes and d-type modes are reversed.

near the double Dirac cone by varying the parameter R. Therefore, the topologically protected edge states can be realized easily by combining two types of lattices with different topological characteristics in the proposed system. Finally, we construct a directional sharp bend waveguide, which shows the robustness propagation of electromagnetic waves is observed in the sharp bend waveguide interface.

THEORETICAL MODEL AND BAND STRUCTURE OF THE HYBRID TOPOLOGICAL MATERIAL

A hexagonal arrangement of the metal cylindrical resonators is shown in **Figure 1A**. The six cylindrical resonators are inserted into a dielectric slab as presented in **Figure 1B**. We choose rhombus-shaped unit cell, where the relevant parameters are shown as follows: the lattice length of unit cell is a, and the distance between the center of each resonator to the center of rhombus-shaped unit cell is R. Each rhombus-shaped unit cell includes six cylindrical resonators in a hexagonal arrangement, showing the C_6 symmetry.

Numerical simulations are performed by using a commercial simulation software High Frequency Structure Simulation Software (HFSS) based on three-dimensional finite element numerical analysis. The metal cylindrical resonators are defined as PEC, and the dielectric slab is Teflon with the relative permittivity of 2.1 and the thickness of $h_d = 2.5mm$. The size of the unit cell is $a = 17\sqrt{3}mm$, and $R = a/3$. The diameter and the height of the cylindrical resonator are both 6 mm (i.e., $d_1 = h_r = 6mm$). The periodic boundary conditions are introduced in the direction of the two lattice vectors. Based on the zone-folding technique, as shown in **Figure 1A**, we select a

unit cell composed of six resonators instead of two resonators. **Figure 1C** presents the band structure, which shows a double Dirac cone is created at the Γ point ($f_d = 5.55GHz$).

As shown in **Figure 2**, it is demonstrated that the band structure can be changed by varying the parameters R. The band inversion can be realized by different values of R. When R is shrunk (**Figure 2A**) or expanded (**Figure 2B**), it can be seen that a complete band gap appears, and simultaneously, the double Dirac cone becomes two double-degenerate modes. The emergence of band gap is due to the change in translational periodicity of the resonators. Keeping the C_6 symmetry, these double-degenerate modes are located above and below the Dirac frequency, respectively. Analogy to electronic orbital shapes, as $R = 0.91a/3$, the lower frequency modes are p-type (p_1 and p_2 as shown in the bottom of **Figure 2A**), and the higher frequency modes are d-type (d_1 and d_2, upper in **Figure 2A**). However, as $R = 1.06a/3$, the topological characteristic of the band gap is completely different from the case of $R = 0.91a/3$. As shown in **Figure 2B**, the degenerate modes are flipped, p-type modes are at the higher frequency and d-type are at the lower frequency. That is to say, band inversion is realized as R varies.

We use the method proposed by Takahiro Fukui et al. [45] to calculate the spin Chern number of the proposed topological material. As $R = 0.91a/3$, the spin Chern number is zero, indicating topologically trivial. In contrast, as $R = 1.06a/3$, the bands have non-zero spin Chern number, which shows the topologically non-trivial. The change of spin Chern number indicates the topological phase transition. Combined **Figure 1C** and **Figure 2**, it can be seen that there is a band gap near the Dirac frequency. As R is shrunk, the double Dirac cone is opened and a complete band gap occurs. In contrast, as R is expanded, the double Dirac cone can also be opened and a band inversion occurs with the topological phase transition. These results

FIGURE 3 | (A) Multi-cell configuration consists of two parts with 10 topologically non-trivial lattices on the left and 10 topologically trivial lattices on the right. **(B)** Band structure of the multi-cell configuration, where the blue and red lines represent the edge states. It can be seen that there are two different pseudo-spin modes at the interface. Red indicates clockwise and blue is anticlockwise. **(C)** Electric field distributions of the multi-cell configuration. The direction of pseudo-spin modes corresponding to **A** and **B** in **Figure 3B**. The color represents the electric field intensity, and the arrows represent the direction of the time-averaged energy flux.

indicate the proposed topological material can possess the characteristics from topologically trivial to topologically non-trivial.

TOPOLOGICAL EDGE STATES

In this section, we combine topologically non-trivial ($R = 1.06a/3$) and topologically trivial ($R = 0.91a/3$) lattices to form multi-cell configurations, and study wave guiding characteristics. As shown in **Figure 3A**, the multi-cell configuration consists of two parts, with 10 topologically non-trivial lattices on the left and 10 topologically trivial lattices on the right. In the simulations, the periodic boundary conditions are introduced in the direction of the two lattice vectors. The band structure of the multi-cell configuration is shown in **Figure 3B**, where the blue and red lines represent edge states. It can be seen that there are two points A and B corresponding to the same eigen-frequency (5.57 GHz). **Figure 3C** presents the electric field distribution of the points A and B, which shows the electromagnetic wave is well confined at the interface between

the topologically non-trivial and trivial lattices both for A and B. However, for the point A, the clockwise pseudo-spin mode is realized at the interface, and anticlockwise pseudo-spin mode is observed for the point B. The direction of the two pseudo-spin modes at the interface is opposite.

As shown in **Figure 3B**, there are two different pseudo-spin modes at the interface of topologically non-trivial and trivial lattices at the same frequency. As shown in **Figure 3C**, opposite spins of these modes can be verified. In general, each frequency of the topological band gap corresponds to two edge states, and the pseudo-spin directions of the two edge states are different. Electromagnetic waves with a certain pseudo-spin direction can only propagate in a fixed direction, which is consistent with the characteristics of the quantum Hall effect.

SHARP BEND WAVEGUIDES

Since the proposed structure can support topological edge states, it is expected that new devices can be implemented by using this unique property. We construct a sharp bend interface by using two types of lattices ($R = 1.06a/3$ and $R = 0.91a/3$), which can operate as a directional waveguide. As shown in **Figure 4A**, we combine topologically non-trivial and topologically trivial lattices to form a two-dimensional sharp bend structure. The upper part of the red line is the topologically non-trivial lattices, and the lower part of the red line is the topologically trivial lattices. In this case, the interface of the two lattices has sharp angles.

In the simulation, the excitation source (denoted by a yellow star in **Figure 4B**) is set at the left side of the junction of the topologically non-trivial and trivial lattices. Radiation boundary conditions are introduced around the two-dimensional sharp bend structure. Simulation results show that the electromagnetic waves can propagate along the sharp bend interface in the frequency range of 5.54–5.8 GHz without obvious backscattering. **Figure 4B** presents the electric field distribution of the structure at 5.7 GHz, which shows electromagnetic waves can propagate along the sharp angles interface without back-scattering. The interface of the non-trivial transport operates like a waveguide.

In order to further verify the robustness of electromagnetic wave propagation along the sharp bend interface, as shown in **Figure 5**, two types of defects are introduced. For the defect 1 as presented in **Figure 5A**, six metal cylindrical resonators are removed from the topologically trivial lattices. The simulated electric field distribution shows there is no back-scattering and electromagnetic waves can transmit completely in this sharp bend interface. For the defect 2 as presented in **Figure 5B**, we remove the four resonators in the same topologically trivial lattices. As expected, the similar result is observed. Therefore, it can be seen that this non-trivial edge state transmission is robust.

CONCLUSION

To conclude, we present a design scheme for a topological material, consisting of six metal cylindrical resonators and a dielectric slab. The topological properties of the system are
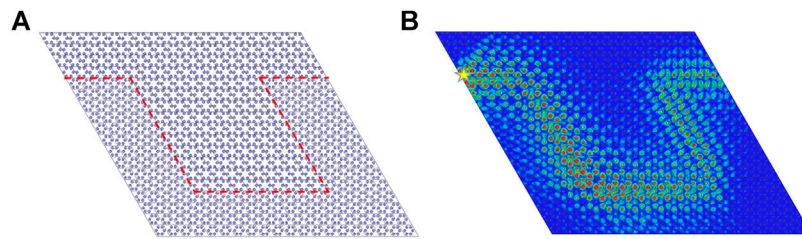
FIGURE 4 | (A) Two-dimensional sharp bend structure consists of topologically non-trivial and trivial lattices. The upper part of the red line is the topologically non-trivial lattices, and the lower part of the red line is the topologically trivial lattices. **(B)** Electric field distribution of the sharp bend structure at 5.7 GHz. The yellow star indicates the excitation source, and the color indicates the electric field intensity.
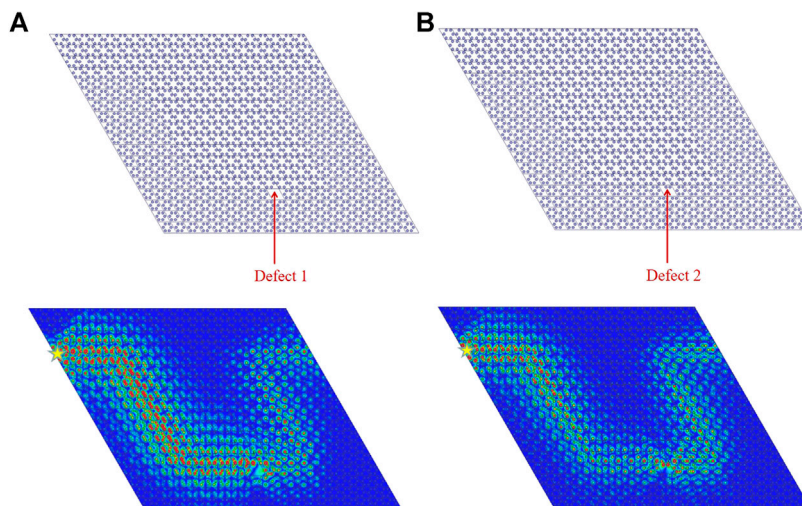
FIGURE 5 | Two types of the defects and the corresponding electric field distributions at 5.7 GHz. **(A)** Defect 1, and **(B)** Defect 2.

studied numerically. Different topologically band gaps are achieved by via changing the geometric parameter *R*. It is demonstrated that the multi-cell configuration composed of two types of lattices with distinct topologies can generate topologically protected edge states. Moreover, the topologically protected edge states can be used to design a sharp bend waveguide, and it exhibits great robustness with immunity to imperfections. It can be expected that this edge state of back-scattering suppression can have potential applications in optical transport and photonic integrated circuits.

DATA AVAILABILITY STATEMENT

The raw data supporting the conclusions of this article will be made available by the authors, without undue reservation.

REFERENCES

1. Qi XL, Zhang SC. Topological insulators and superconductors. *Rev. Mod. Phys* (2011) **83**:1057. doi:10.1103/revmodphys.83.1057

AUTHOR CONTRIBUTIONS

YL conceived the idea and supervised the project. LD and ML performed the numerical simulations. KS and XZ did the theoretical analysis. LD and YL co-wrote the manuscript.

ACKNOWLEDGMENTS

2. Hasan MZ, Kane CL. Colloquium: topological insulators. *Rev. Mod. Phys* (2010) **82**:3045. doi:10.1103/revmodphys.82.3045

3. Wang Z, Chong Y, Joannopoulos JD, Soljačić M. Observation of unidirectional backscattering-immune topological electromagnetic states. *Nature* (2009) **461**(7265):772–5. doi:10.1038/nature08293

4. Khanikaev AB, Mousavi SH, Tse WK, Kargarian M, MacDonald AH, Shvets G. Photonic topological insulators. *Nature Mater* (2013) **12**:233–9. doi:10.1038/nmat3520

5. Liang GQ, Chong YD. Optical resonator analog of a two-dimensional topological insulator. *Phys Rev Lett* (2013) **110**:203904. doi:10.1103/physrevlett.110.203904

6. Hafezi M, Mittal S, Fan J, Migdall A, Taylor JM. Imaging topological edge states in silicon photonics. *Nature Photon* (2013) **7**:1001–5. doi:10.1038/nphoton.2013.274

7. He C, Sun XC, Liu XP, Lu MH, Chen Y, Feng L, et al. Photonic topological insulator with broken time-reversal symmetry. *Proc Natl Acad Sci USA* (2016) **113**(18):4924–8. doi:10.1073/pnas.1525502113

8. Chen BGg, Upadhyaya N, Vitelli V. Nonlinear conduction via solitons in a topological mechanical insulator. *Proc Natl Acad Sci USA* (2014) **111**(36):13004–9. doi:10.1073/pnas.1405969111

9. Paulose J, Chen BGg, Vitelli V. Topological modes bound to dislocations in mechanical metamaterials, *Nature Phys* (2015) **11**:153–6. doi:10.1038/nphys3185

10. Meeussen AS, Paulose J, Vitelli J. Geared topological metamaterials with tunable mechanical stability. *Phys Rev X* (2016) **6**:041029. doi:10.1103/physrevx.6.041029

11. Nash LM, Kleckner D, Read A, Vitelli V, Turner AM, Irvine WTM. Topological mechanics of gyroscopic metamaterials. *Proc Natl Acad Sci USA* (2015) **112**(47):14495–500. doi:10.1073/pnas.1507413112

12. Süsstrunk R, Huber SD. Observation of phononic helical edge states in a mechanical topological insulator. *Science* (2015) **349**(6243):47–50. doi:10.1126/science.aab0239

13. Vila J, Pal RK, Ruzzene M. Observation of topological valley modes in an elastic hexagonal lattice. *Phys Rev B* (2017) **96**:134307. doi:10.1103/physrevb.96.134307

14. Xiao M, Ma G, Yang Z, Sheng P, Zhang ZQ, Chan CT. Geometric phase and band inversion in periodic acoustic systems. *Nature Phys* (2015) **11**:240–4. doi:10.1038/nphys3228

15. Khanikaev AB, Fleury R, Mousavi SH, Alu A. Topologically robust sound propagation in an angular-momentum-biased graphene-like resonator lattice. *Nat Commun* (2015) **6**:8260. doi:10.1038/ncomms9260

16. Mousavi SH, Khanikaev AB, Wang Z. Topologically protected elastic waves in phononic metamaterials. *Nat Commun* (2015) **6**:8682. doi:10.1038/ncomms9682

17. Fleury R, Khanikaev AB, Alu A. Floquet topological insulators for sound. *Nat Commun* (2016) **7**:11744. doi:10.1038/ncomms11744

18. He C, Ni X, Ge H, Sun XC, Chen YB, Lu MH, et al. Acoustic topological insulator and robust one-way sound transport. *Nature Phys* (2016) **12**:1124–9. doi:10.1038/nphys3867

19. Peng YG, Qin CZ, Zhao DG, Shen YX, Xu XY, Bao M, et al. Experimental demonstration of anomalous floquet topological insulator for sound. *Nat Commun* (2016) **7**:13368. doi:10.1038/ncomms13368

20. Liu TW, Semperlotti F. Tunable acoustic valley-hall edge states in reconfigurable phononic elastic waveguides. *Phys. Rev. Appl* (2018) **9**:014001. doi:10.1103/physrevapplied.9.014001

21. Geng ZG, Peng YG, Li PQ, Shen YX, Zhao DG, Zhu XF. Mirror-symmetry induced topological valley transport along programmable boundaries in a hexagonal sonic crystal. *J Phys Condens Matter* (2019) **31**(24):245403. doi:10.1088/1361-648x/ab0fcc

22. Fang C, Fu L. Rotation anomaly and topological crystalline insulators. arXiv:1709.01929 (2017)

23. Song ZD, Fang Z, Fang C. (d-2)-dimensional edge states of rotation symmetry protected topological states. *Phys Rev Lett* (2017) **119**:246402. doi:10.1103/physrevlett.119.246402

24. Schindler F, Cook AM, Vergniory MG, Wang Z, Parkin SSP, Bernevig BA, et al. Higher-order topological insulators. *Sci Adv* (2018) **4**:eaat0346. doi:10.1126/sciadv.aat0346

25. Liu YH, Guo QH, Liu HC, Liu CC, Song K, Yang K, et al. Circular-polarization-selective transmission induced by spin-orbit coupling in a helical tape waveguide. *Phys Rev Applied* (2018) **9**:054033. doi:10.1103/physrevapplied.9.054033

26. Yang B, Guo QH, Tremain B, Barr LE, Gao WL, Liu HC, et al. Direct observation of topological surface-state arcs in photonic metamaterials. *Nat Commun* (2017) **8**:97. doi:10.1038/s41467-017-00134-1

27. Ma T, Khanikaev AB, Mousavi SH, Shvets G. Guiding electromagnetic waves around sharp corners: topologically protected photonic transport in metawaveguides. *Phys Rev Lett*(2015) **114**:127401. doi:10.1103/physrevlett.114.127401

28. Kane CL, Mele EJ. Quantum spin hall effect in graphene. *Phys Rev Lett* (2005) **95**:226801. doi:10.1103/physrevlett.95.226801

29. Bernevig BA, Hughes TL, Zhang SC. Quantum spin hall effect and topological phase transition in HgTe quantum wells. *Science* (2006) **314**(5806):1757–61. doi:10.1126/science.1133734

30. Wu LH, Hu X. Scheme for achieving a topological photonic crystal by using dielectric material. *Phys Rev Lett* (2015) **114**:223901. doi:10.1103/physrevlett.114.223901

31. Yang L, Yu K, Wu Y, Zhao R, Liu S. Topological spin-hall edge states of flexural wave in perforated metamaterial plates. *J Phys D Appl Phys* (2018) **51**(32):325302. doi:10.1088/1361-6463/aace49

32. Tzuhsuan M, Shvets G. Scattering-free edge states between heterogeneous photonic topological insulators. *Phys Rev B* (2017) **95**:165102. doi:10.1103/physrevb.95.165102

33. Huo SY, Chen JJ, Huang HB. Topologically protected edge states for out-of-plane and in-plane bulk elastic waves. *J Phys Condens Matter* (2018) **30**:145403. doi:10.1088/1361-648x/aab22a.

34. Xu L, Wang HX, Xu YD, Chen HY, Jiang JH. Accidental degeneracy in photonic bands and topological phase transitions in two-dimensional core-shell dielectric photonic crystals. *Opt Express* (2016) **24**:18059. doi:10.1364/oe.24.018059

35. Xie BY, Su GX, Wang HF, Wang HF, Su H, Shen XP, et al. Visualization of higher-order topological insulating phases in two-dimensional dielectric photonic crystals. *Phys Rev Lett* (2019) **122**:233903. doi:10.1103/physrevlett.122.233903

36. Lu L, Joannopoulos JD, Soljačić M. Topological photonics. *Nat Photon* (2014) **8**:821–29. doi:10.1038/nphoton.2014.248

37. Sun XC, He C, Liu XP, Lu MH, Zhu SN, Chen YF. Two-dimensional topological photonic systems. *Prog Quantum Electron* (2017) **55**:52–73. doi:10.1016/j.pquantelec.2017.07.004

38. Wu Y, Li C, Hu XY, Ao YT, Zhao YF, Gong QH. Applications of topological photonics in integrated photonic devices. *Adv Opt Mater* (2017) **5**(8):1700357. doi:10.1002/adom.201700357

39. Khanikaev AB, Shvets G. Two-dimensional topological photonics. *Nature Photon* (2017) **11**:763–73. doi:10.1038/s41566-017-0048-5

40. Ozawa T, Price HM, Amo A, Goldman N, Hafezi M, Lu L, et al. Topological photonics. *Rev Mod Phys* (2019) **91**:015006. doi:10.1103/RevModPhys.91.015006

41. Haldane FDM, Raghu S. Possible realization of directional optical waveguides in photonic crystals with broken time-reversal symmetry. *Phys Rev Lett* (2008) **100**:013904. doi:10.1103/physrevlett.100.013904

42. Zhang Z, Tian Y, Wang Y, Gao S, Cheng Y, Liu X, et al. Directional acoustic antennas based on valley-hall topological insulators. *Adv Mater* (2018) **30**(36):1803229. doi:10.1002/adma.201803229

43. Wei F, Liu CW, Li D, Wang CY, Zhang HR, Sun JR, et al. Broken mirror symmetry tuned topological transport in PbTe/SnTe heterostructures. *Phys Rev B* (2018) **98**:161301. doi:10.1103/physrevb.98.161301

44. Chaunsali R, Chen CW, Yang J. Subwavelength and directional control of flexural waves in zone-folding induced topological plates. *Phys Rev B* (2018) **97**:054307. doi:10.1103/physrevb.97.054307

45. Fukui T, Hatsugai Y, Suzuki H. Chern numbers in discretized brillouin zone: Efficient method of computing (spin) hall conductances. *J Phys Soc Jpn* (2005) **74**(6):1674–77. doi:10.1143/jpsj.74.1674

Graphene-Based Tunable Wideband Metamaterial Absorber With Polarization Insensitivity and Wide Incident Angle

Liansheng Wang[1]*, Dongyan Xia[2], Quanhong Fu[3], Xueyong Ding[1] and Yuan Wang[1]

[1] Science and Polytechnic Department, Sanya University, Sanya, China, [2] Finance and Economics Department, Sanya University, Sanya, China, [3] Science Department, Northwestern Polytechnical University, Xi'an, China

A graphene-based tunable wideband metamaterial absorber with polarization insensitivity and wide incident angle is presented in this paper. The results show that the absorption is over 90% from 5 to 8 GHz when the Fermi level of graphene is 0.5 eV, and the absorption can be tuned by electrically changing the Fermi level of graphene. The mechanism of wideband and tunable absorption is explained by calculating the normalized input impedance and monitoring the surface current. Finally, the results adequately verify that the absorption of metamaterial absorber has the advantages of polarization insensitivity and wide incident angle. Thus, it holds great potential application value in many fields such as electromagnetic stealth, electromagnetic shielding, communication, and so on.

Keywords: wideband, tunable, graphene, metamaterial absorber, wide-incident-angle

INTRODUCTION

In recent years, metamaterial, a kind of artificially structured material has attracted wide attention due to its unique electromagnetic properties [1–3]. With the development of research on metamaterial, researchers discovered that metamaterial has great potential in the fields of super lens, electromagnetic stealth, optical black hole, polarization converter, perfect electromagnetic absorption, and many more [4–8]. Among the above applications, metamaterial absorber was proposed by Landy et al. [9]. Since then, the research of metamaterial absorber has attracted extensive attention because of its perfect electromagnetic absorption property, ultrathin microstructure, and great potential in military and civil applications. Currently, the research of metamaterial absorber mainly focuses on the wide incident angle, polarization independency, tunability, and multiband absorption [10–14]. However, the wideband metamaterial absorber is more suitable for the application of practical electromagnetic environment. At present, many methods have been used to expand the absorption bandwidth of metamaterial absorber, such as vertical superposition of different resonant units, fractal structure, and magnetic media and so on [15–18]. Among them, the combination of lumped element, plasma Brewster enhancement, and strong coupling effect with metamaterial absorber is a very effective method to realize wideband metamaterial absorber [19–21].

Compared with the traditional passive metamaterial absorber, the active metamaterial absorber can realize the active adjustment of its electromagnetic property by changing the parameters of lumped components or the electromagnetic property of the intermediate medium, so it has more application prospects in practice.

Based on the electrically tunable conductivity of graphene, a graphene-based tunable wideband metamaterial absorber with polarization insensitivity and wide incident angle is designed in this paper. The results show that the absorption of metamaterial absorber is more than 90% from 5 to 8 GHz when the Fermi energy level of graphene is 0.5 eV, and the absorption can be tuned by electrically changing the Fermi level of graphene. Further study shows that the absorption property of metamaterial absorber has the advantages of polarization insensitivity and wide incident angle.

THE ELECTRICALLY TUNABLE CONDUCTIVITY OF GRAPHENE

Graphene is a kind of two-dimensional planar crystal with very high electron and hole mobility. Its conductivity can be regulated by changing the external bias voltage applied on graphene, so graphene is widely used in tunable microwave and terahertz devices. When there is no bias magnetic field applied on graphene, its conductivity from microwave to visible band can be expressed by Kubo formula [22]:

$$\sigma(\omega, \mu_c) = \frac{-ie^2(\omega+i2\Gamma)}{\pi \hbar^2} \left\{ \frac{1}{(\omega+i2\Gamma)^2} \int_0^\infty \varepsilon \left[\frac{\partial f_d(\varepsilon)}{\partial \varepsilon} - \frac{\partial f_d(-\varepsilon)}{\partial \varepsilon} \right] d\varepsilon - \int_0^\infty \varepsilon \left[\frac{f_d(-\varepsilon) - f_d(\varepsilon)}{(\omega+i2\Gamma)^2 - 4(\varepsilon/\hbar)^2} \right] d\varepsilon \right\} \tag{1}$$

$$f_d(\varepsilon) = [\exp(\varepsilon - \mu_c)/(k_B T) + 1]^{-1} \tag{2}$$

In the formulas (1) and (2), k_B is the Boltzmann constant, $\hbar$ is the reduced Dirac constant, $f_d(\varepsilon)$ is the Fermi Dirac distribution function, μ_c is the Fermi level of graphene, T is the Kelvin temperature, and $\Gamma = 5 \times 10^{12} Hz$ is the carrier scattering rate. According to formulas (1) and (2), the calculated conductivity of graphene with different Fermi levels is shown in **Figure 1**.

It can be seen from **Figure 1** that the conductivity of graphene increases with the increasing of its Fermi level. The main method of changing the Fermi level of graphene is applying bias voltage on it. The Fermi level of graphene under different bias voltages applied on can be expressed as:

$$E_{bias} = \frac{e}{\varepsilon_0 \pi \hbar^2 v_F^2} \int_0^\infty \varepsilon [f_d(\varepsilon) - f_d(\varepsilon + 2\mu_c)] d\varepsilon \tag{3}$$

In formula (3), E_{bias} is the bias voltage applied on graphene, $v_F = 10^6 m/s$ is the velocity of the electron. Graphene can be set as a material with the thickness of 0.001 μm, and the conductivity as shown in **Figure 1**.

MODEL DESIGN

The unit cell of our graphene-based tunable wideband metamaterial absorber with polarization insensitivity and wide incident angle is presented in **Figure 2**. The unit cell consists of five layers: fractal tree metal loaded with graphene, FR4 medium (ε=4.3, tan $\delta = 0.025$), cross metal, FR4 medium, and metallic ground, in which the fractal tree metal and cross metal layer are connected by passing metal rods through the middle FR4 layer, as illustrated in **Figure 2**. The metal part of unit cell is composed of copper (). The optimized parameters of the unit cell are $a = b = 9$ mm, $c = d = e = 0.6$ mm, $f = 8.5$ mm, $t_1 = 0.6$ mm, $t_2 = 2$ mm, $t_3 = 0.1$ mm. Doped silicon is used as the electrode to apply bias voltage on graphene.

The modeling and numerical simulation of metamaterial absorber is performed with Microwave Studio CST. At the simulation process, the boundary conditions of x and y directions are set as unit cell, the z direction is set as open, All+Floquet ports are used to simulate the incoming and outgoing waves. The electromagnetic parameters are calculated by using frequency domain electromagnetic solver.

RESULTS AND DISCUSSION

When the incident electromagnetic waves enter into the proposed metamaterial absorber, the magnetic and electric resonances will be produced independently. The electromagnetic power of incident waves gets absorbed gradually by the dielectric loss and the loss of lumped graphene. When the absorption of metamaterial absorber reaches near perfect absorption, it obtains a state such that the permittivity equals the permeability and at the same time matches the impedance to free space. In a more direct perspective, the absorption of metamaterial absorber can be expressed as:
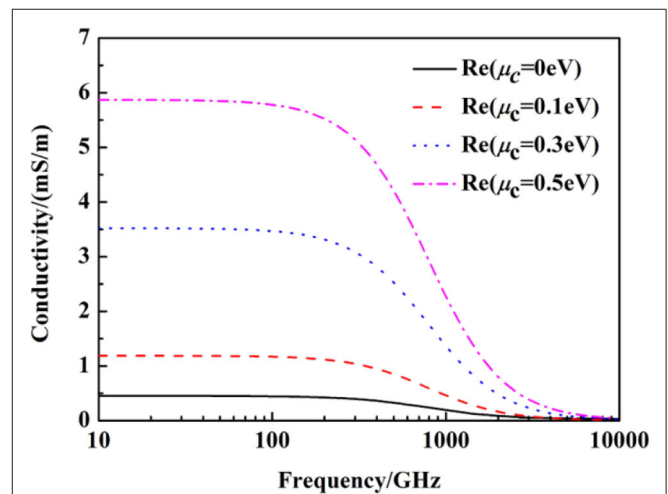
FIGURE 1 | The conductivity of graphene under different Fermi levels.
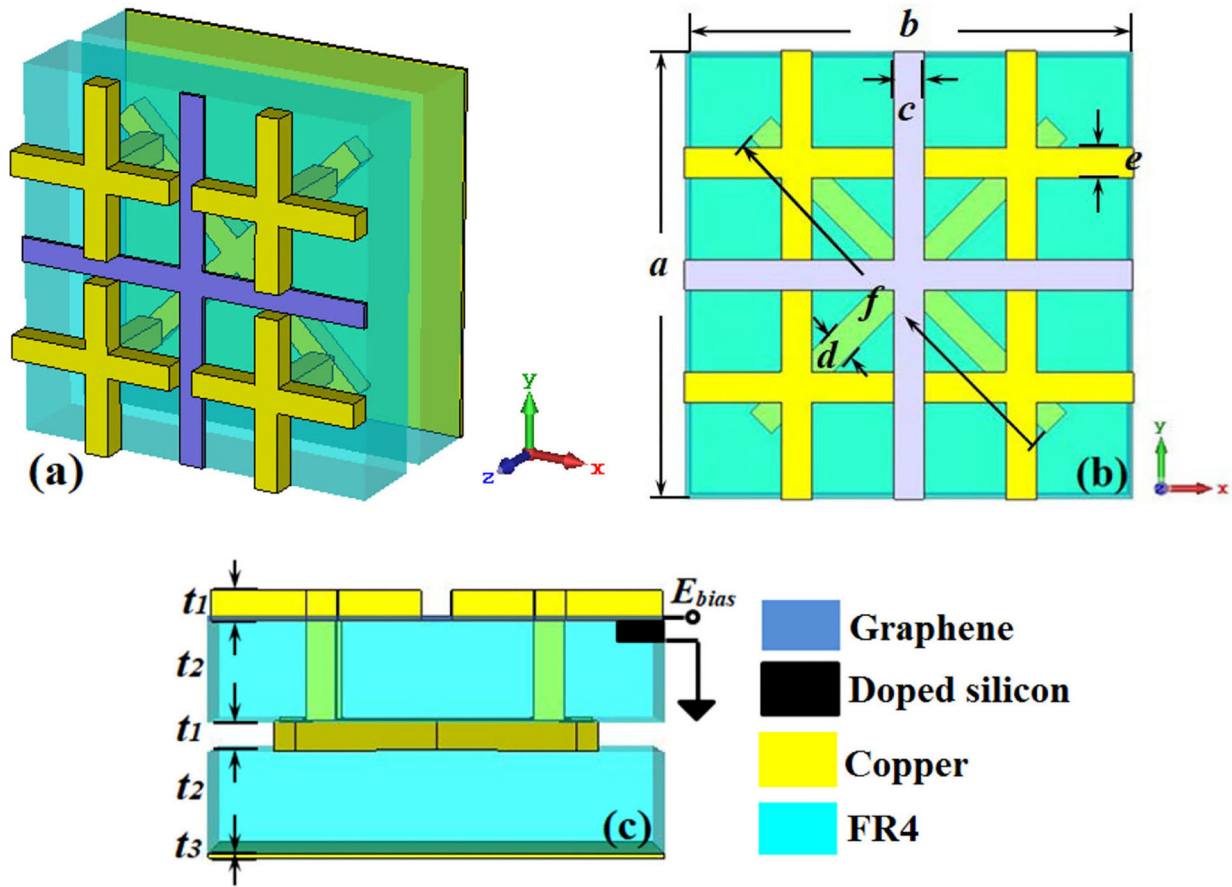
FIGURE 2 | The diagram of the metamaterial absorber unit cell: **(A)** perspective view, **(B)** front view, **(C)** side view.
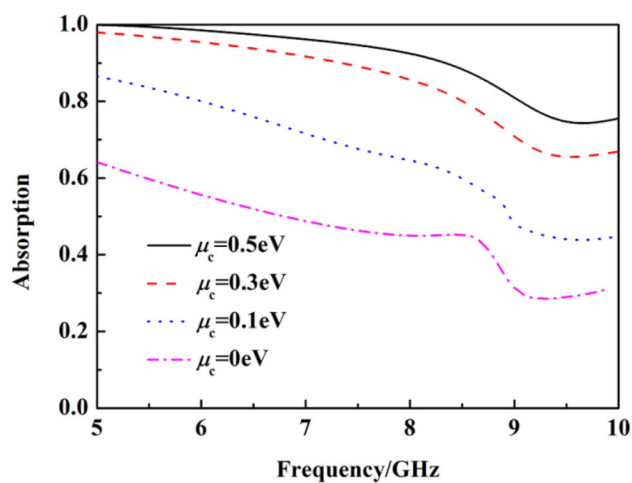
FIGURE 3 | The absorption of the metamaterial absorber under different Fermi levels.
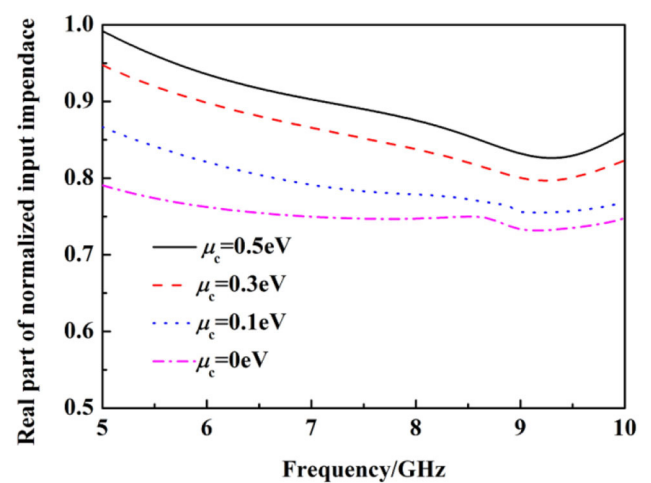
FIGURE 4 | The real part of normalized input impendence of the metamaterial absorber with free space.

FIGURE 5 | (a,b) The surface current distribution of the metamaterial absorber at 5 GHz with the Fermi level of graphene at 0.5 eV.
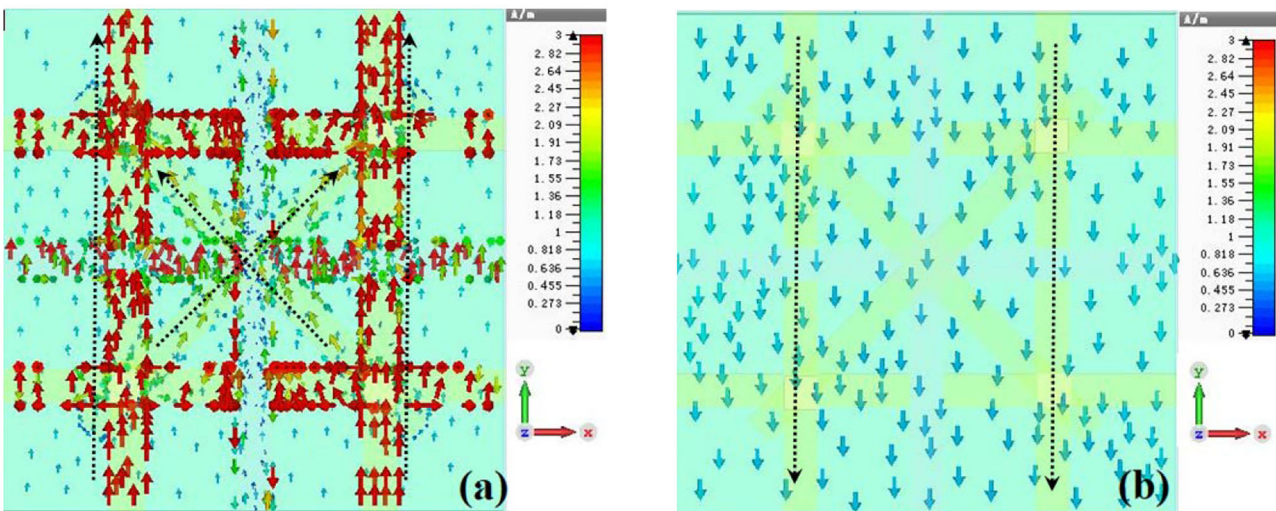
FIGURE 6 | (a,b) The surface current distribution of the metamaterial absorber at 6 GHz with the Fermi level of graphene at 0.5 eV.

$$A(\omega) = 1 - R(\omega) - T(\omega) = 1 - \left|S_{11}(\omega)\right|^2 - \left|S_{21}(\omega)\right|^2 \quad (4)$$

Since the metallic ground of unit cell prevents the incident electromagnetic wave transmission, the above calculation formula of absorption can be simplified as:

$$A(\omega) = 1 - R(\omega) = 1 - \left|S_{11}(\omega)\right|^2 \quad (5)$$

According to formula (5), we calculate the absorption of metamaterial absorber under different Fermi levels, as shown in **Figure 3**. It can be seen from **Figure 3** that the absorption

of metamaterial absorber exceeds 90% from 5 to 8 GHz when the Fermi level of graphene is at 0.5 eV, and the absorption of metamaterial absorber from 5 to 8 GHz gradually decreases with the decreasing of the Fermi level of graphene.

At present, the theory of equivalent medium can effectively explain the physical mechanism of metamaterial absorber [23]. According to the theory of equivalent medium, the metamaterial absorber can be regarded as an equivalent medium, which can be characterized by the equivalent permittivity $\varepsilon(\omega)$ and equivalent permeability $\mu(\omega)$. According to the calculation, formula of normalized input impedance $Z(w)/Z_0 = \sqrt{u(w)/\varepsilon(w)}$, when the equivalent permittivity $\varepsilon(\omega)$ and the equivalent

permeability $\mu(\omega)$ of metamaterial absorber are identical, the normalized input impedance of metamaterial absorber with free space equals one, and then the reflection of metamaterial absorber to the incident wave reaches zero. As an outcome, the perfect absorption of metamaterial absorber will be realized. According to the S_{11} and S_{21} parameters extracted by simulation, the normalized input impedance $Z_1(\omega)$ $(Z_1(\omega)=Z(\omega)/Z_0)$ of metamaterial absorber under different Fermi levels is calculated using the scattering parameter method [24], as shown in **Figure 4**. It can be seen from **Figure 4** that the real part of the normalized input impedance of metamaterial absorber with free space is close to one from 5 to 8 GHz with the Fermi energy level of graphene at 0.5 eV. This indicates that the metamaterial

absorber has a good impedance matching with free space and achieves the condition of perfect absorption. At the same time, the real part of the normalized input impedance of metamaterial absorber with free space decreases gradually with the increasing of frequency, which leads to the decreasing of absorption.

In order to analyze the mechanism of wideband absorption, the surface current distribution of metamaterial absorber at 5, 6, and 7 GHz with the Fermi level of graphene at 0.5 eV is monitored, as shown in **Figures 5**, **7**. It can be seen from **Figures 5A**, **6A**, **7A** that the generated surface current at the top fractal tree metal layer and the middle cross metal layer flows upward (although the surface current of the cross metal structure at 7 GHz is downward, it is very weak). This will lead
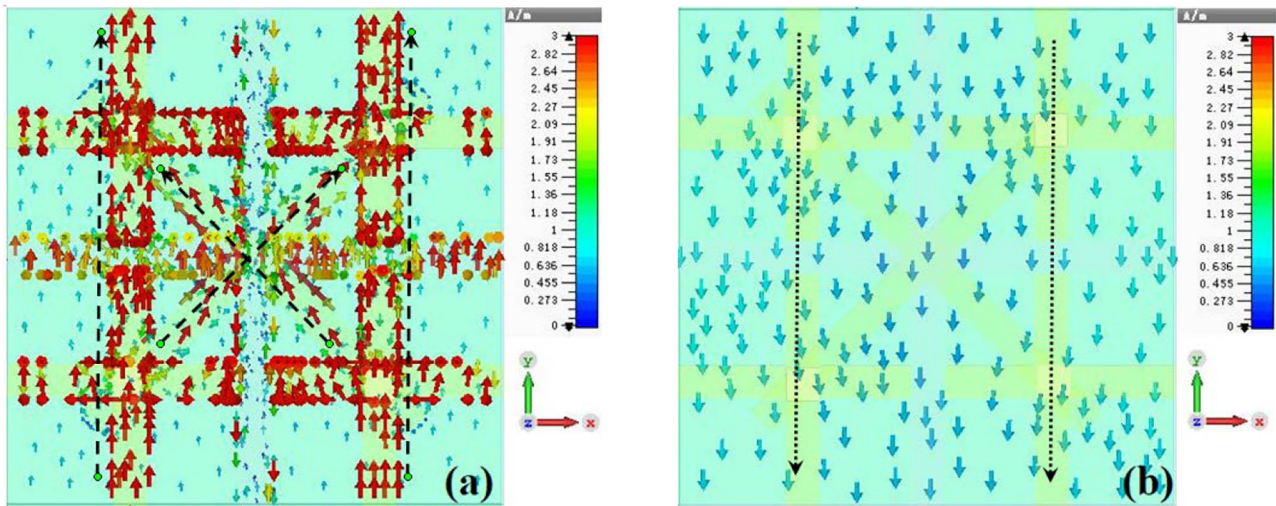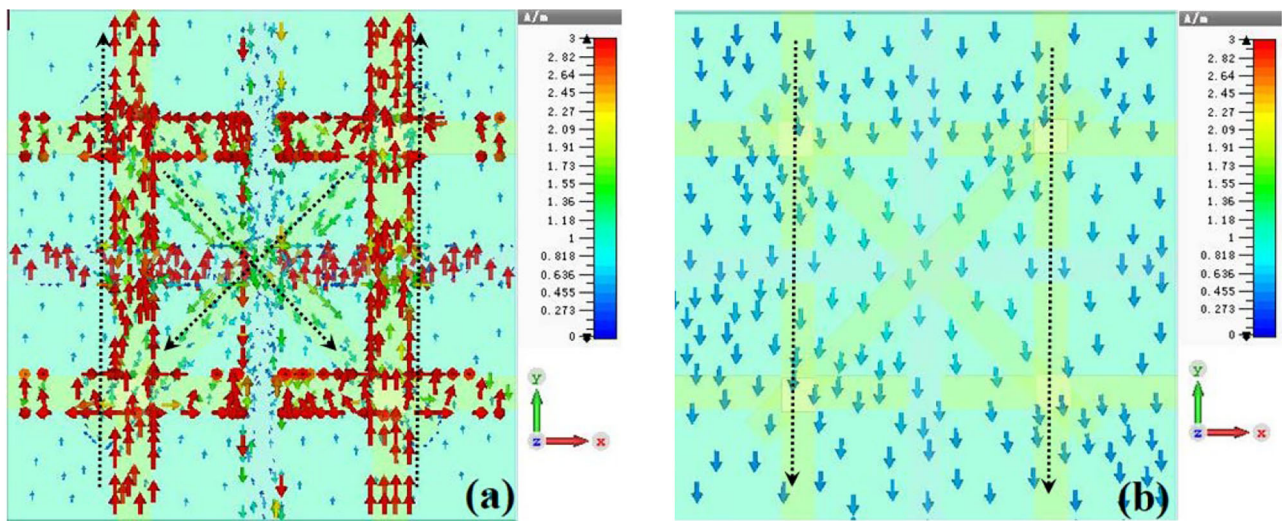

FIGURE 7 | (a,b) The surface current distribution of the metamaterial absorber at 7 GHz with the Fermi level of graphene at 0.5 eV.
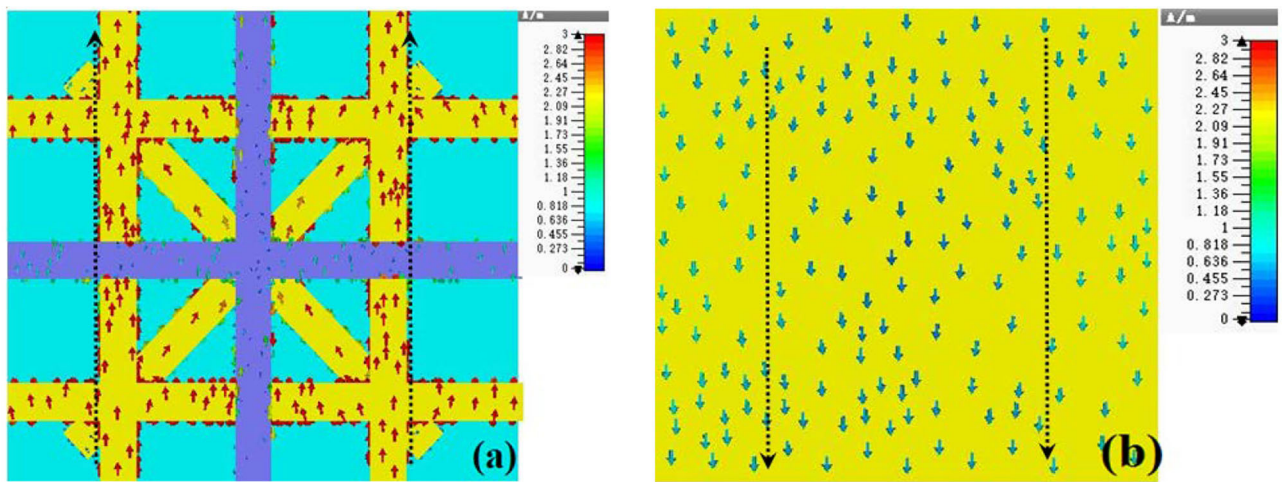
FIGURE 8 | (a,b) The surface current distribution of the metamaterial absorber at 5 GHz with the Fermi level of graphene at 0 eV.

to the alternating accumulation of charges in the y direction, and then form electric dipole resonance [25]. It can be seen from **Figures 5B**, **6B**, **7B** that the generated surface current at the bottom metal substrate flows downward, which is opposite to the current direction of the top fractal tree metal layer and the cross metal layer. This antiparallel current forms a current circuit, which can cause a strong magnetic response resonance [26]. The magnetic resonance and electrical resonance are realized simultaneously at 5, 6, and 7 GHz and achieve the condition of perfect absorption. The wideband absorption is caused by the overlay of different resonance frequencies.

In order to further analyze the mechanism of tunable absorption, the surface current of metamaterial absorber at 5 GHz with the Fermi level of graphene at 0 eV is monitored, as shown in **Figure 8**. It can be seen from **Figure 8** that the metamaterial absorber generates electric resonance and magnetic resonance under the action of incident microwave [25, 26]. However, the excited surface currents on the fractal tree metal layer and the cross metal layer are weaker than the one at Fermi level of 0.5 eV (**Figure 5**), so the generated electromagnetic resonance is very weak, this results in lower absorption.

The absorption of metamaterial absorber under different polarization angles with the Fermi level of graphene at 0.5 eV is calculated, as shown in **Figure 9**. It can be seen from **Figure 9** that the absorption of the metamaterial absorber under different

FIGURE 9 | The absorption of the metamaterial absorber under different polarization states with the Fermi level of graphene at 0.5 eV.

FIGURE 11 | The absorption of the metamaterial absorber under different structural dimension parameters c with the Fermi level of graphene at 0.5 eV.

FIGURE 10 | The absorption of the metamaterial absorber under different incident angles with the Fermi level of graphene at 0.5 eV: **(a)** transverse electric (TE) mode, **(b)** transverse magnetic (TM) mode.

FIGURE 12 | The absorption of the metamaterial absorber under different structural dimension parameters *e* with the Fermi level of graphene at 0.5 eV.

polarization angles is the same due to the rotational symmetry of the unit cell.

The absorption of the metamaterial absorber under different incident angles with the Fermi level of graphene at 0.5 eV is calculated, as shown in **Figure 10**. It can be seen from **Figure 10** that the absorption of the metamaterial absorber from 5 to 8 GHz gradually decreases with the incident angle increasing from 0 to 60° at transverse electric (TE) mode and transverse magnetic (TM) mode, but it can still be up to 90% from 5 to 8 GHz when the incident angle is 60°. The results show that the absorption of metamaterial absorber has the advantage of wide incident angle.

The structural size of the metamaterial absorber has an important influence on its absorption. The absorption of the metamaterial absorber under different graphene width *c* and fractal tree metal linewidth *e* with the Fermi level of graphene at 0.5 eV is calculated, as shown in **Figures 11**, **12**. It can be seen from **Figures 11**, **12** that the absorption of the metamaterial absorber gradually decreases with the increasing of structure size parameters *c* and *e*.

SUMMARY

To summarize, a graphene-based tunable wideband metamaterial absorber with polarization insensitivity and wide incident angle is presented in this paper. The metamaterial absorber provides >90% absorption from 5 to 8 GHz when the Fermi level of graphene is 0.5 eV. The absorption of the metamaterial absorber can be tuned electrically by applying an external bias voltage on graphene. Simulation results unveil that the response of the absorber presents a remarkably high absorption for a wide range of incident angles and is insensitive to polarization angle but has a relationship with its structure size parameters. The metamaterial absorber delivers the advantages of wideband, tunable, polarization insensitivity, and wide incident angle. It has great potential application value in the fields of electromagnetic stealth, electromagnetic shielding, communication, and so on.

DATA AVAILABILITY STATEMENT

The raw data supporting the conclusions of this article will be made available by the authors, without undue reservation.

AUTHOR CONTRIBUTIONS

All authors listed have made a substantial, direct and intellectual contribution to the work, and approved it for publication.

REFERENCES

1. Cui TJ, Smith DR. *Metamaterials: Theory, Design, Applications.* New York, NY: Springer (2010).
2. Alastair P, Hibbins BR, Evans J, Sambles R. Experimental verification of designer surface. *Plasmon Sci.* (2005) 308:670–2. doi: 10.1126/science.1109043
3. Uchida K, Adachi H, Kikuchi D, Ito S, Qiu Z, Maekawa S, et al. Generation of spin currents by surface plasmon resonance. *Nat Commun.* (2015) 6:5910. doi: 10.1038/ncomms6910
4. Quader S, Zhang J, Akram MR, Zhu W. Graphene-based high-efficiency broadband tunable linear-to-circular polarization converter for terahertz waves. *IEEE J Select Topics Quant Electron.* (2020) 26:4501008. doi: 10.1109/JSTQE.2020.2969566
5. Zhang J, Wei X, Rukhlenko ID, Chen HT, Zhu W. Electrically tunable metasurface with independent frequency and amplitude modulations. *ACS Photonics.* (2020) 7:265–71. doi: 10.1021/acsphotonics.9b01532
6. Zhang J, Wei X, Premaratne M, Zhu W. Experimental demonstration of electrically tunable broadband coherent perfect absorber based on graphene-electrolyte-graphene sandwich structure. *Photonics Res.* (2019) 7:868–74. doi: 10.1364/PRJ.7.000868
7. Liu B, Zhu W, Gunapala SD, Stockman MI, Premaratne M. Open resonator electric spaser. *ACS Nano.* (2017) 11:12573–82. doi: 10.1021/acsnano.7b06735

8. Akram MR, Ding G, Chen K, Feng Y, Zhu W. Ultra-thin single layer metasurfaces with ultra-wideband operation for both transmission and reflection. *Adv Mater.* (2020) 32:1907308. doi: 10.1002/adma.201907308
9. Landy NI, Sajuyigbe SJ, Mock J, Smith DR, Padilla WJ. Perfect metamaterial absorber. *Phys Rev Lett.* (2008) 100:207402. doi: 10.1103/PhysRevLett.100.207402
10. Aydin K, Ferry VE, Briggs RM, Atwater HA. Broadband polarization-independent resonant light absorption using ultrathin plasmonic super absorbers. *Nat Commun.* (2011) 2:517. doi: 10.1038/ncomms1528
11. Xu HX, Wang GM, Qi MQ, Liang JG, Gong JQ, Xu ZM. Triple-band polarization insensitive wide-angle ultra-miniature metamaterial transmission line absorber. *Phys Rev B.* (2012) 86:205104. doi: 10.1103/PhysRevB.86.205104
12. Ding F, Cui YX, Ge XC, Jin Y, He SL. Ultra-broadband microwave metamaterial absorber. *Appl Phys Lett.* (2012) 100:103506. doi: 10.1063/1.3692178
13. Argyropoulos C, Le KQ, Mattiucci N. Broadband absorbers and selective emitters based on plasmonic Brewster metasurfaces. *Phys Rev B.* (2013) 87:205112. doi: 10.1103/PhysRevB.87.205112
14. Li L, Yang Y, Liang C. Ultrathin multiband gigahertz metamaterial absorbers. *J Appl Phys.* (2011) 110:063702. doi: 10.1063/1.3608246

15. Othman MAK, Guclu C, Capolino F. Graphene-based tunable hyperbolic metamaterials and enhanced near-field absorption. *Opt Express*. (2013) 21:7614–32. doi: 10.1364/OE.21.007614

16. Cao T, Wei C, Simpson RE, Zhang L, Cryan MJ. Rapid phase transition of a phase-change metamaterial perfect absorber. *Opt Mater Express*. (2013) 3:1101–10. doi: 10.1364/OME.3.001101

17. Kebin F, Strikwerda AC, Zhang X, Averitt RD. Three-dimensional broadband tunable terahertz metamaterials. *Phys Rev B*. (2013) 87:161104. doi: 10.1103/PhysRevB.87.161104

18. Hedayati MK, Zillohu AU, Strunskus T, Faupel F, Elbahri M. Plasmonic tunable metamaterial absorber as ultraviolet protection film. *Appl Phys Lett*. (2014) 104:041103. doi: 10.1063/1.4863202

19. Huang Y, Wen G, Zhu W, Li J, Si LM, Premaratne M. Experimental demonstration of a magnetically tunable ferrite based metamaterial absorber. *Opt Express*. (2014) 22:16408–17. doi: 10.1364/OE.22.016408

20. Wang P, Casadei F, Shan S, Weaver JC, Bertoldi K. Harnessing buckling to design tunable locally resonant acoustic metamaterials. *Phys Rev Lett*. (2014) 113:014301. doi: 10.1103/PhysRevLett.113.014301

21. Tuong PV, Park JW, Rhee JY, Kim KW, Jang WH, Cheong H, et al. Polarization-insensitive and polarization-controlled dual-band absorption in metamaterials. *Appl Phys Lett*. (2013) 102:081122. doi: 10.1063/1.4794173

22. Fallahi A, Perruisseau-Carrier J. Design of tunable biperiodic graphene metasurfaces. *Phys Rev B*. (2012) 86:195408. doi: 10.1103/PhysRevB.86.195408

23. Chen HT. Interference theory of metamaterial perfect absorbers. *Opt Express*. (2012) 20:7165–72. doi: 10.1364/OE.20.007165

24. Smith DR, SchultzS. Determination of negative permittivity and permeability of metamaterials from reflection and transmission coefficients. *Phys Rev B*. (2002) 65:195104. doi: 10.1103/PhysRevB.65.195104

25. Chen JF, Huang XT, Zerihun G. Polarization-independent, thin, broadband metamaterial absorber using double-circle rings loaded with lumped resistances. *J Electron Mater*. (2015) 44:4269–74. doi: 10.1007/s11664-015-3951-x

26. Bhattacharyya S, Ghosh S, Srivastava KV. Triple band polarization-independent metamaterial absorber with bandwidth enhancement at X-band. *J Appl Phys*. (2013) 114:094514. doi: 10.1063/1.4820569

Stereo Perfect Metamaterial Absorber Based on Standing Gear-Shaped Resonant Structure With Wide-Incident-Angle Stability

Guangsheng Deng, Kun Lv, Hanxiao Sun, Zhiping Yin and Jun Yang*

Special Display and Imaging Technology Innovation Center of Anhui Province, Academy of Opto-Electronic Technology, Hefei University of Technology, Hefei, China

In this work, a single-band metamaterial absorber (MA) based on a three dimensional (3D) resonant structure is presented. The unit cell is composed of a standing gear-shaped resonator, which is embedded in the dielectric substrate. The proposed 3D MA is ultrathin with a total thickness of 2.3 mm, corresponding $0.077\lambda_0$ at its center frequency. The simulation results demonstrate a high absorption peak at 10.1 GHz with absorptivity of 99.9%. The proposed 3D MA is insensitive to the polarization of the incident wave due to its rotationally symmetric structure. Moreover, the proposed 3D MA exhibits a wide-incident-angle stability, as absorptivity of more than 85% can be achieved for both TE and TM incidences with incident angle up to 60°. Most importantly, multiband electromagnetic wave absorption of the stereo MA can be enabled by adjusting the structural parameters of the standing gear. The proposed structure is compatible with 3D printing technology and has potential applications in electromagnetic shielding.

Keywords: metamaterial, absorber, three dimension, single-band, wide-incident-angle stability

INTRODUCTION

Electromagnetic (EM) metamaterials that consist meta-molecules arranged in an array of subwavelength pe have attracted intense attention due to their unique properties, such as negative refractive index [1] and inverse Doppler effects [2]. Recently, the perfect absorber has been closely related to metamaterials, which has potential applications in biological sciences [3], sensing [4, 5], communications [6, 7] and solar energy harvesting [8].

The perfect metamaterial absorber (MA) was firstly presented by Landy et al. [9]. Since then the MAs have been designed to exhibit different characteristics such as single-band [10, 11], dual-band [12, 13], multiband absorption [14–17] and broadband absorption [18–21]. Till now, most of the reported MAs are based on planar resonators (2D structure) [11, 22–24]. However, the absorbing performance of the planar design will deteriorate significantly under oblique incidences with large incident angles.

Recently, the 3D printing technology [25] has experienced significant development and paved a way for the design and fabrication of 3D structures. One of the advantages of the 3D design scheme is that it can improve the design flexibility of the MA by providing additional freedom in structure design. Hence a 3D MA can enable higher absorption at oblique incidences. For instance, Wu et al. presented a symmetric all-metal three-dimensional (3D) MA by using two orthogonally oriented copper stand-up spilt ring resonators at THz frequency and obtained more than 90% THz wave
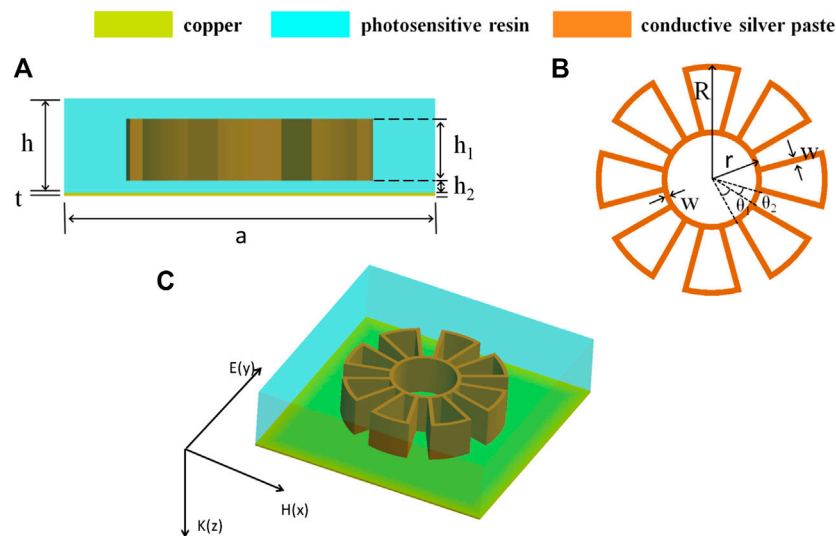
FIGURE 1 | Schematic geometry of a unit cell for the proposed 3D MA **(A)** Front view **(B)** layout of the gear-shaped resonator, and **(C)** perspective view of the unit cell.

absorption for both TE and TM polarization with incident angle up to 60° [26]. Lv et al. [27] proposed a three-dimensional ultra-broadband metamaterial absorber with full graphite structure that exhibited excellent absorption properties at large incident angles.

In this paper, a novel single-band and polarization-insensitive MA based on a 3D gear-shaped resonant structure is presented and near unity (99.9%) absorption at absorption peak frequency of 10.1 GHz under normal incidence is numerically demonstrated. Here, we introduce a new strategy on the design of 3D MAs by extruding planar resonator along its normal direction. Compared with the original planar resonant structure, the proposed structure can offer higher absorption for both TE and TM-polarized waves with large incident angles. The surface current and the field density distributions are investigated to explore the absorption mechanism of the 3D structure. Moreover, by adjusting the number of gear teeth, perfect single- or multi-band absorption can be achieved based on the stereo resonant structure. The proposed MA has the potential to be applied in the energy-harvesting and EM shielding applications.

STRUCTURE DESIGN AND SIMULATION

Figure 1 shows the geometry of a unit cell of the proposed single-band 3D MA. The standing gear-shaped 3D resonator made of silver ink with an electrical conductivity of $\sigma = 5.88 \times 10^5$ S/m, is embedded in the dielectric substrate. Here, we select silver ink to construct metallic standing gear, as it is perfectly compatible with 3D printing technology. The substrate is realized on photosensitive resin with a relative permittivity of 2.9 and a loss tangent of 0.02. Moreover, in order to eliminate the EM wave transmission through the structure, a 0.017 mm thick copper

TABLE 1 | Dimensions and parameters of the proposed 3D MA.

Parameter	Value (mm)	Parameter	Value (mm)	Parameter	Value (mm)
a	9	h	2.3	w	0.15
R	3	h_1	1.5	θ_1	30°
r	1.3	h_2	0.1	θ_2	15°
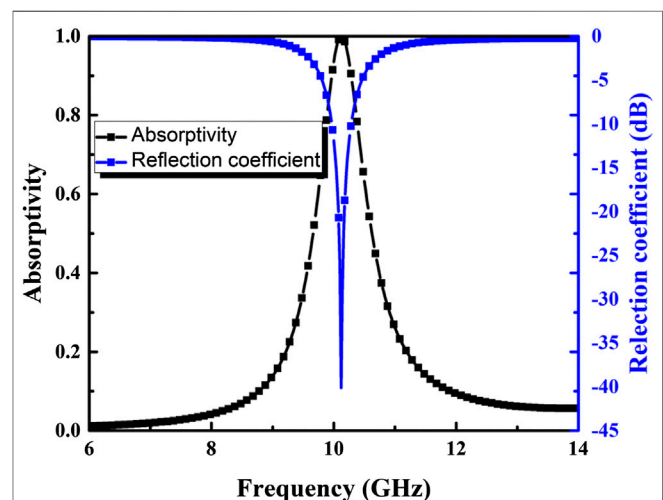
FIGURE 2 | Absorption and reflection spectrum of the proposed MA under normal incidence.

plate with an electric conductivity of 5.8×10^7 S/m is covered on the bottom of the structure as a ground plane. **Figure 1** shows the configuration of the unit cell structure, while the optimized parameters of the 3D MA are listed in **Table 1**. The simulation results were obtained using a finite-element method
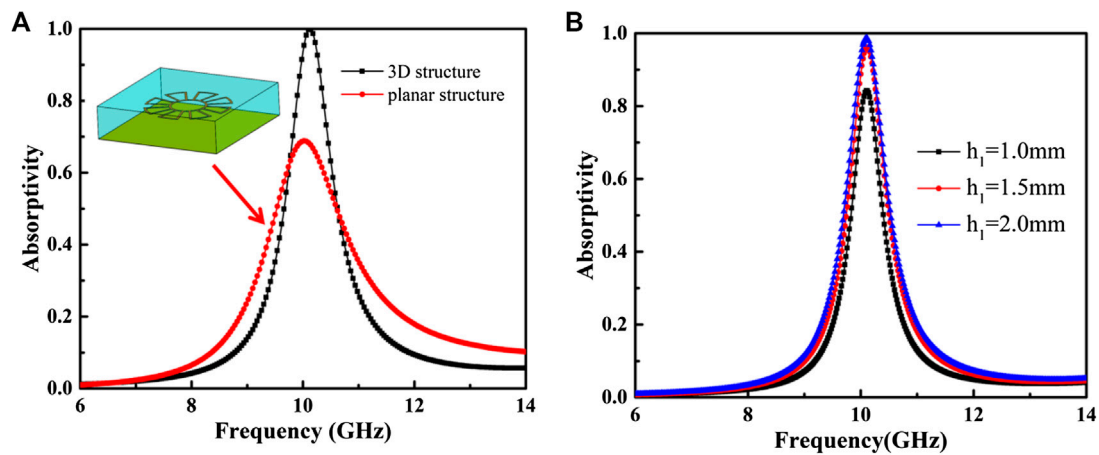
FIGURE 3 | (A) Comparison of the absorption spectrum of the proposed 3D MA and the planar design under normal incidence **(B)** Absorption spectrum dependency on the thickness of the standing gear-shaped structure at incidence angle of 45°.
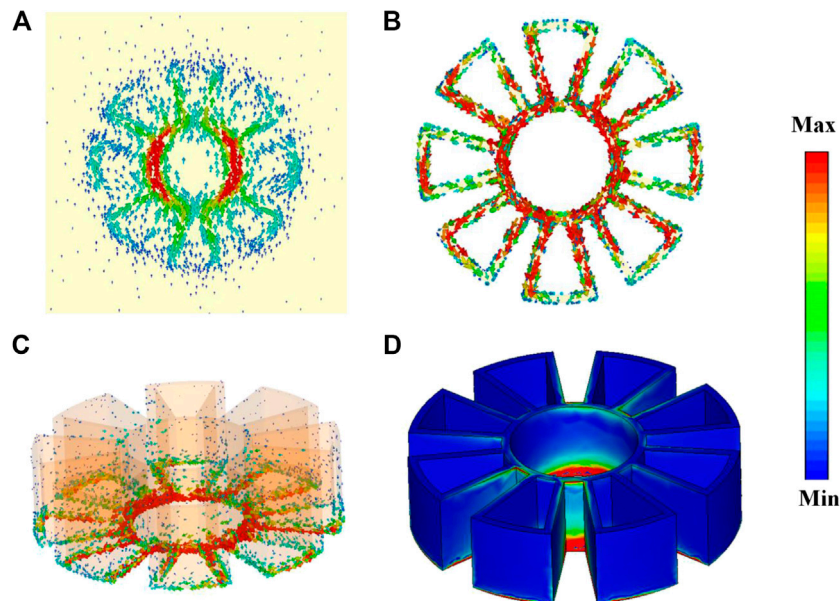
FIGURE 4 | Simulated surface current distribution on **(A)** bottom ground layer **(B)** 3D resonator on top view, and **(C)** 3D resonator on perspective view, and **(D)** distribution of the power loss on the 3D resonator.
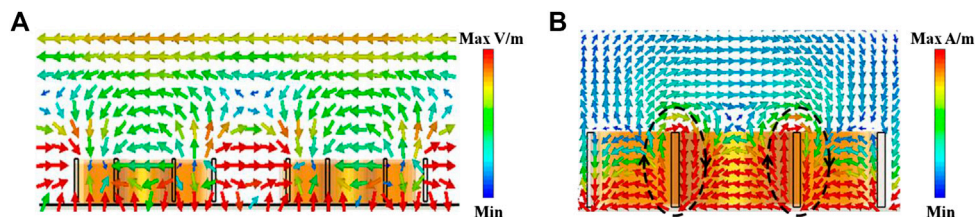
FIGURE 5 | Simulated **(A)** electric, and **(B)** magnetic field distributions within the 3D MA.
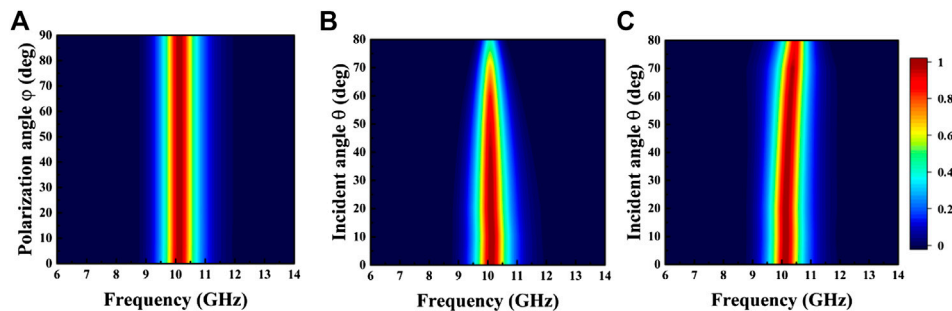
FIGURE 6 | Absorption spectra for **(A)** different polarization angles φ and different incidence angles θ for **(B)** TE, and **(C)** TM polarization.
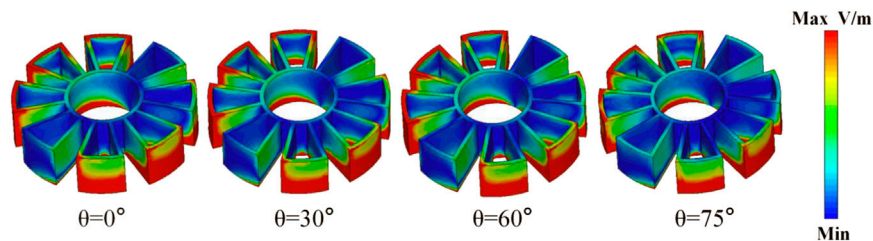
FIGURE 7 | Simulated electric field distributions for TM polarization under different incident angles θ.

(FEM). In the simulation, the unit cell boundary conditions were applied in x and y directions, and the open space boundary condition was utilized in the z direction. The absorptivity (A) can be defined as $A(\omega) = 1 - R(\omega) - T(\omega) = 1 - |S_{11}(\omega)|^2 - |S_{21}(\omega)|^2$, where $S_{11}(\omega)$ and $S_{21}(\omega)$ are the reflection and the transmission coefficients, respectively. The transmission coefficient $S_{21}(\omega)$ is zero due to the existence of copper ground. Therefore, the absorptivity can be simplified as $A(\omega) = 1 - |S_{11}(\omega)|^2$.

The simulated absorption spectrum of the proposed 3D MA under normal incidence is shown in **Figure 2**. It can be seen from **Figure 2** that there exists a sharp absorption peak located at 10.1 GHz with an absorptivity of 99.9%. Hence, the proposed MA exhibits perfect single band incident electromagnetic wave absorption.

RESULTS AND DISCUSSION

Figure 3A compares the absorptivity of the proposed stereo structure and the planar design under normal incidence. It can be seen from the figure that the absorptivity of the stereo MA is much larger than that of the planar structure at peak resonant frequency. In order to analyze the dependence of the height of the stereo resonant structure (h_1) on the EM wave absorption under oblique incidence, the influence of h_1 on absorption spectrum at wave incident angle of 45° is simulated and the results are shown in **Figure 3B**. From **Figure 3B**, the absorptivity increases till a nearly perfect absorption with the increase of h_1, which demonstrates the outstanding absorbing performance of the proposed stereo structure at wide incidence angles.

The surface current distribution on the gear-shaped 3D resonator and the copper ground under the TM-polarized incidence at peak resonant frequency of 10.1 GHz are depicted in **Figure 4**. It can be seen from **Figure 4A** that the surface current on the stereo structure flows in the same direction along the E-field vector of the incident wave, where the electric resonance can be excited within the MA. Meanwhile, **Figure 4B** shows that the current is mainly concentrated in the inner ring of the standing gear-shaped structure, and the current flow direction in the copper ground is in reverse with that in the stereo resonant structure, as the anti-parallel current will lead to a magnetic resonance. Hence, both magnetic and electric resonances are responsible for EM wave absorption under normal incidence. **Figure 4C** illustrates the perspective view of the current distribution on the stereo gear-shaped resonator. Although the surface current is strongly concentrated in the bottom of the gear, the current flow on the side wall of the standing sectors also contributes the power consumption as shown in **Figure 4C**. The power loss distribution shown in **Figure 4D** confirms that the extra power consumption on the standing walls is responsible for the stronger absorption compared with planar structure. Moreover, from **Figure 4D**, one can anticipate more power dissipation on the walls by increasing the height of the standing gear, which is in accordance with our previous discussion of the absorption dependence on gear height h_1.

Figure 5 shows the electric and magnetic field distributions to further explain the mechanism of the enhanced absorption of the stereo structure. It can be seen from the electric field distribution shown in **Figure 5A** that the strong coupling between adjacent

References	Structure	Normal	Absorption at 20°		Absorption at 40°		Absorption at 60°		Polarization insensitive
			TE	TM	TE	TM	TE	TM	
[25]	2D	95.8	>90	90	>90	80	>90	75	Yes
[26]	3D	99.6	>90	>90	>90	>90	>90	>90	Yes
[28]	2D	97.5	>90	>90	>90	>90	72	>90	Yes
[29]	2D	97	>95	>95	>95	>95	92	>95	Yes
This work	3D	99.9	99	99	98	99	86	99	Yes

TABLE 2 | The comparison of the absorption between the proposed MA and some reported MAs at different incident angles.

standing elements will enhance the intensity of electric resonance within the structure. Moreover, the magnetic field distribution illustrated in **Figure 5B** suggests that there exist two pairs of co-directional magnetic field rings due to the introduction of the standing walls. Since the magnetic rings can be regarded as an electric dipole, the oscillation of the dipole results in a strong electric response of the MA which further enhances the EM wave absorption.

ABSORPTION SPECTRUM DEPENDENCE ON WAVE POLARIZATION AND INCIDENT ANGLE

In many practical applications, the characteristic of polarization-independent is an important criterion to evaluate the absorption performance of the MAs. **Figure 6A** illustrates the simulated absorption maps of the proposed MA under different polarization angles. It can be observed that the absorption of the MA is insensitive to different polarization angles, which is attributed to the rotationally symmetric layout of the cell structure.

The absorbing performance of the stereo MA is further investigated for TE- and TM-polarized incidences at different incident angles, and the simulated results are shown in **Figures 6B,C**, respectively. For the TE-polarized incidence, the absorptivity remains above 85% with incident angle θ up to 60°. However, the further increase of θ leads to a dramatically degradation of EM wave absorption. For the TM-polarized incidence, the absorptivity remains greater than 90% when incident angle θ reaches up to 80°. However, the absorption peak frequency slightly blue-shifted with the increase of θ. Hence, the proposed structure exhibits wide-incident-angle stability for both TE and TM polarizations. In order to gain the electromagnetic response of the stereo structure under oblique incidences, the electric field distributions for TM-polarized incidence with incident angle $\theta = 0°$, 30°, 60° and 75° are shown in **Figure 7**. It can be seen from the figure that both the distribution and the intensity of the electric field are insensitive to wave incident angle. Thus, the proposed stereo MA has a good capacity on effective EM wave absorption at wide incident angles. The equivalent circuit model for analysis of the absorption peaks under oblique incidence is not given in this paper. However, the mechanism can be briefly illustrated as follow: the impedance matching of free space and the input impedance of the stereo structure, which determines the absorptivity, is strongly dependent on the EM wave incident angle. Compared with the planar structure, the standing walls of the gear enables an extra compensation of impedance matching at wide incident angles, hence enhancing the wave absorption. In **Table 2**, we compared the performance of the proposed MA with some reported MAs at different incident angles. As it can be seen that our proposed structure exhibits stronger incident wave absorption under oblique incidences for both TE and TM polarization.

Another advantage of the proposed standing gear-shaped resonant structure is the adjustable perfect single- or multi-band absorption. In general, by increasing the amount of the
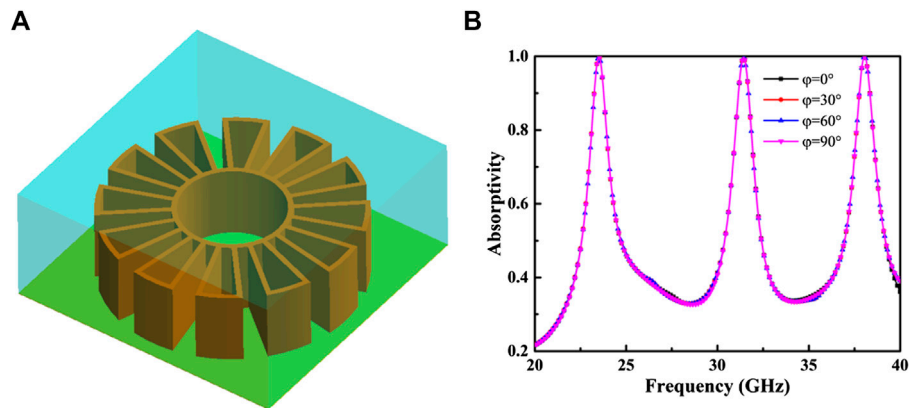
FIGURE 8 | (A) Configuration of the triple-band 3D MA **(B)** Simulated absorption spectrum under normal incidence with different polarization angles φ.

TABLE 3 | Dimensions and parameters of the triple-band 3D MA.

Parameter	Value (mm)	Parameter	Value (mm)	Parameter	Value (mm)
A	8	h	3.4	W	0.15
R	3.6	h_1	2.1	θ_1	20°
R	1.6	h_2	0	θ_2	10°
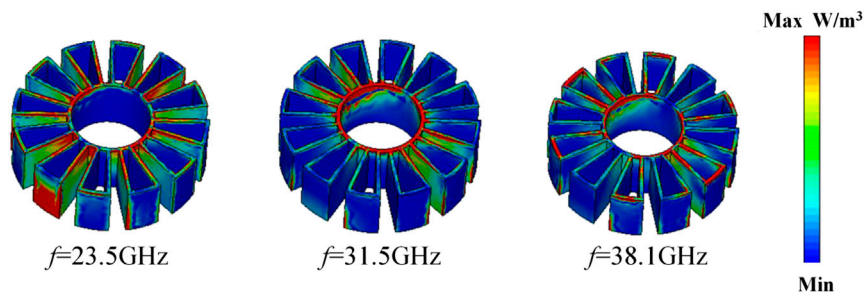
FIGURE 9 | Power loss density distributions on the 3D resonator at three peak absorption frequencies.

gear teeth, the resonant modes within the structure will also increase due to the enhanced coupling between these adjacent teeth. Hence, one can anticipate more absorption peaks with lager counts of gear teeth. For instance, a perfect triple-band absorption can be achieved by optimizing the structural parameters of the stereo structure. The layout and the absorption spectrum of the triple-band MA are illustrated in **Figure 8**, while the detailed parameter dimensions of the unit cell structure are listed in **Table 3**. The simulation results demonstrate three distinct absorption peaks at 23.5, 31.5, and 38.1 GHz with absorption of 99.9, 99.5, and 99.9%, respectively. **Figure 9** shows the power loss density distributions of the stereo triple-band MA for TE-polarized incidence at three resonant frequencies. It can be seen from **Figure 9** that the incident power is significantly consumed at the side wall and the top plane of the standing gear-shaped resonator for these three resonant peaks, which is different from the absorption mechanism discussed earlier in the article. Hence, the stereo

structure provides more degree of freedom in constructing multi-functional MAs compared with the planar design.

CONCLUSION

A standing gear-shaped perfect metamaterial absorber with wide-incident-angle stability is presented in this paper. The stereo resonator that is constructed with conductive silver ink, can be embedded into the substrate using 3D printing technology. The rotationally symmetric structure enables the polarization-independent absorption of the proposed MA under normal incidence, while the stereo resonator also endows the MA with good absorbing capacity at wide incident angles. The simulation results demonstrate and validate that the proposed MA exhibits near unity single-band absorption under normal incidence. Moreover, for oblique incidences, the proposed MA maintains

absorptivity above 85 and 95% up to incident angles of 60° and 80° for TE and TM polarizations, respectively. In addition, a perfect multi-band absorption can be achieved by adjusting the structural parameters of the stereo structure. The stereo absorber has potential applications in the energy harvesting and stealth fields.

DATA AVAILABILITY STATEMENT

The raw data supporting the conclusions of this article will be made available by the authors, without undue reservation.

REFERENCES

1. Smith DR, Pendry JB, Wiltshire MCK. Metamaterials and negative refractive index. *Science* (2004) 305:788–92. doi:10.1126/science.1096796
2. Seddon N, Bearpark T. Observation of the inverse Doppler effect. *Science* (2003) 302:1537–40. doi:10.1126/science.1089342
3. Marin BC, Ramirez J, Root SE, Aklile E, Lipomi DJ. Metallic nanoislands on graphene: a metamaterial for chemical, mechanical, optical, and biological applications. *Nanoscale Horizons* (2017) 2:311–8. doi:10.1039/c7nh00095b
4. Yi Z, Huang J, Cen CL, Chen XF, Zhou ZG, Tang YJ, et al. Nanoribbon-ring cross perfect metamaterial graphene multi-band absorber in THz range and the sensing application. *Results Phys* (2019) 14:102367. doi:10.1016/j.rinp.2019.102367
5. Sang T, Wang R, Li JL, Zhou JY, Wang YK. Approaching total absorption of graphene strips using a c-Si subwavelength periodic membrane. *Optic Commun* (2018) 413:255–60. doi:10.1016/j.optcom.2017.12.065
6. Yang W, Lin YS. Tunable metamaterial filter for optical communication in the terahertz frequency range. *Optics Express* (2020) 28: 17620–9. doi:10.1364/Oe.396620
7. Yu BY, Zhao YJ, Chen JQ, Ge Y, Chen XF. Broadband transparent metamaterial absorber in wireless communication band based on indium tin oxide film. *Int J RF Microw Comput-Aid Eng* (2019) 29:e219551. doi:10.1002/mmce.21955
8. Hossain MJ, Faruque MRI, Islam MT. Perfect metamaterial absorber with high fractional bandwidth for solar energy harvesting. *PLoS ONE* (2018) 13: e0207314. doi:10.1371/journal.pone.0207314
9. Landy NI, Sajuyigbe S, Mock JJ, Smith DR, Padilla WJ. Perfect metamaterial absorber. *Phys Rev Lett* (2008) 100:279–82. doi:10.1103/PhysRevLett.100.207402
10. Cheng YZ, Yang HL, Cheng ZZ, Wu N. Perfect metamaterial absorber based on a split-ring-cross resonator. *Appl Phys Mater Sci Process* (2011) 102:99–103. doi:10.1007/s00339-010-6022-4
11. Lim D, Lee D, Lim S. Angle- and polarization-insensitive metamaterial absorber using Via array. *Sci Rep* (2016) 6:39686. doi:10.1038/srep39686
12. Wang BX, He YH, Xu NX, Wang XY, Wang YC, Cao JJ. Design of dual-band polarization controllable metamaterial absorber at terahertz frequency. *Results Phys* (2020) 17:103077. doi:10.1016/j.rinp.2020.103077
13. Wang CC, Huang MH, Zhang Z, Xu W. Dual band metamaterial absorber: combination of plasmon and Mie resonances. *J Mater Sci Technol* (2020) 53: 37–40. doi:10.1016/j.jmst.2020.02.058
14. Cheng YZ, Cheng ZZ, Mao XS, Gong RZ. Ultra-thin multi-band polarization-insensitive microwave metamaterial absorber based on multiple-order responses using a single resonator structure. *Materials* (2017) 10:1241. doi:10.3390/ma10111241
15. Tran CM, Pham HV, Nguyen HT, Nguyen TT, Vu D, Do TH. Creating multiband and broadband metamaterial absorber by multiporous square layer structure. *Plasmonics* (2019) 14:1587–92. doi:10.1007/s11468-019-00953-6
16. Wang BX, Wang GZ, Sang T, Wang LL. Six-band terahertz metamaterial absorber based on the combination of multiple-order responses of metallic patches in a dual-layer stacked resonance structure. *Sci Rep* (2017) 7:41373. doi:10.1038/srep41373
17. Zhao Y, Fu CJ. Design of multiband selective near-perfect metamaterial absorbers with SiO$_2$ cylinder/rectangle shell horizontally embedded in

opaque silver substrate. *Int J Heat Mass Tran.* (2017) 113:281–5. doi:10.1016/j.ijheatmasstransfer.2017.05.090
18. Yu P, Besteiro LV, Huang YJ, Wu J, Fu L, Tan HH, et al. Broadband metamaterial absorbers. *Adv Opt Mater* (2019) 7:1800995. doi:10.1002/adom.201800995
19. Zou JH, Yu P, Wang WH, Tong X, Chang L, Wu C. Broadband mid-infrared perfect absorber using fractal Gosper curve. *J Phys D Appl Phys* (2020) 53: 10516. doi:10.1088/1361-6463/ab57ea
20. Du XM, Yan FP, Wang W, Tan SY, Zhang LN, Bai ZY, et al. A polarization- and angle-insensitive broadband tunable metamaterial absorber using patterned graphene resonators in the terahertz band. *Optic Laser Technol* (2020) 132:106513. doi:10.1016/j.optlastec.2020.106513
21. Akafzade H, Sharma SC. New metamaterial as a broadband absorber of sunlight with extremely high absorption efficiency. *AIP Adv* (2020) 10: 035209. doi:10.1063/1.5131630
22. Lee D, Hwang JG, Lim D, Hara T, Lim S. Incident angle- and polarization-insensitive metamaterial absorber using circular sectors. *Sci Rep* (2016) 6: 27155. doi:10.1038/srep27155
23. Huang YJ, Wen GJ, Zhu WR, Li J, Si LM, Premaratne M. Experimental demonstration of a magnetically tunable ferrite based metamaterial absorber. *Optics Express* (2014) 22:16408–17. doi:10.1364/Oe.22.016408
24. Wu KM, Huang YJ, Wanghuang TL, Chen WJ, Wen GJ. Numerical and theoretical analysis on the absorption properties of metasurface-based terahertz absorbers with different thicknesses. *Appl Opt* (2015) 54:299–305. doi:10.1364/Ao.54.000299
25. Lu YJ, Chi BH, Liu DY, Gao S, Gao P, Huang Y, et al. Wideband metamaterial absorbers based on conductive plastic with additive manufacturing technology. *ACS Omega* (2018) 3:11144–50. doi:10.1021/acsomega.8b01223
26. Wu M, Zhao XG, Zhang JD, Schalch J, Duan GW, Cremin K, et al. A three-dimensional all-metal terahertz metamaterial perfect absorber. *Appl Phys Lett* (2017) 111:051101. doi:10.1063/1.4996897
27. Lv F, Xiao ZY, Lu XJ, Chen MM. Three-dimensional ultra-broadband metamaterial absorber with full graphite structure. *J Electron Mater* (2020) 49:689–94. doi:10.1007/s11664-019-07735-0
28. Yoo M, Kim HK, Lim S. Angular- and polarization-insensitive metamaterial absorber using subwavelength unit cell in multilayer technology. *IEEE Antenn Wireless Propag Lett* (2016) 15:414–7. doi:10.1109/Lawp.2015.2448720
29. Zhu B, Wang Z, Huang C, Feng Y, Zhao J, Jiang T. Polarization insensitive metamaterial absorber with wide incident angle. *Prog Electromagn Res Pier* (2010) 101:231–9. doi:10.2528/Pier10011110

AUTHOR CONTRIBUTIONS

GD conceived the research, wrote the manuscript; KL and HS conducted simulations and analysis, ZY and JY conducted analysis; KL wrote the manuscript.

FUNDING

Electromagnetic Metasurfaces and Reconfigurable Metasurfaces: A Review

Sidrish Zahra, Liang Ma, Wenjiao Wang, Jian Li*, Dexu Chen, Yifeng Liu, Yuedan Zhou, Na Li, Yongjun Huang* and Guangjun Wen

School of Information and Communication Engineering/Sichuan Provincial Engineering Research Center of Communication Technology for Intelligent IoT, University of Electronic Science and Technology of China, Chengdu, China

Metamaterial is a kind of material/structure that is artificially designed and has exceptional electromagnetic properties and/or other physical properties, not found in nature. A class of electromagnetic metamaterial with only one or a few layers of periodic or aperiodic arranged cell structures in the direction of electromagnetic waves propagation can be referred to as a metasurface. Metasurface can be considered as a two-dimensional representation of metamaterial and can realize the controlling of the amplitude, phase, and polarization state/direction of the incident electromagnetic wave. According to the novel electromagnetic characteristics of metasurface and its big advantages, a series of new planar devices and systems based on metasurface can be developed. The goal of this review article is firstly to provide introductions for basic metasurface, its significance properties, and application principles. Meanwhile, the main research progresses of regular metasurfaces and the newly developed reconfigurable metasurfaces are analyzed, focusing on the types of amplitude modulation, phase modulation, polarization modulation, and multidimensional modulation. Finally, the research significances of metasurface development trend and important engineering practical applications are analyzed in the end.

Keywords: metamaterial, metasurface, reconfigurable, wave-front manipulation, applications

INTRODUCTION

Metamaterial is a kind of synthetic structural *material* with singular electromagnetic, acoustic, or mechanical characteristics [1–6]. One can select the appropriate substrate types according to different application requirements and design subwavelength-scale structure (meta-atom) with different shapes, sizes, and rotation directions. According to the subwavelength period or nonperiodic array arrangements, the designed metamaterial can control independently/coherently the amplitude, phase, polarization state/direction, and other parameters of the incident electromagnetic/acoustic wave as needed. In correspondence to this, novel planar functional devices and systems working in different frequency bands such as low frequency, high frequency, microwave, THz, and visible light can be developed [7–16]. Therefore, metamaterials have important application prospects in the fields of science and engineering such as acoustics/mechanics, electromagnetics, optics, and thermodynamics. A class of *electromagnetic* metamaterial consisting of only one layer or a few layers of periodic or aperiodic elements in the direction of electromagnetic wave propagation is also called electromagnetic metasurface [17–21]. The electromagnetic metasurface has subwavelength thickness in the direction of electromagnetic

wave propagation, small size, and light weight, but it can realize the similar electromagnetic wave characteristic controlling abilities as the classical three-dimensional electromagnetic metamaterial. In recent years, therefore, the research on metasurface has become one of the hotspots in the academic and industry areas [22–35].

Based on the Huygens' principle, each subwavelength structure unit of the electromagnetic metasurface will generate a spherical wave packet at the metasurface-air interface under the action of incident electromagnetic waves. The spherical wave packets generated by all metasurface units form a new electromagnetic wave-fronts [36]. Therefore, each metasurface unit can be reversely designed according to the required electromagnetic wave-fronts. And accordingly the electromagnetic wave-fronts can be controlled by adjusting the shape, size, and direction of the metasurface unit [36–40]. Different from conventional large-scale planar optical components or microwave phased array antennas, the metasurface can control and adjust the characteristics of near-field electromagnetic wave in the subwavelength range. It is possible to develop several new high-performance thin-film, ultraminiature planar electromagnetic or optical devices including spatial filters [41, 42], focusing lens [43, 44], beam polarization deflection/converters [45, 46], special beam shaping devices [47, 48], and holographic imaging plates [49, 50]. Therefore, it is of great scientific value to explore and develop a new mechanism, new method, and process technology of artificially synthesized electromagnetic metasurface in the advanced electromagnetic community. In the past decade, many good review articles have been published to summarize the developments of metasurfaces [40, 51–60]. However, those review articles only focused on some parts of the research aspects, like the fundamentals and the specific applications. Most importantly, only a few review articles summarized the research developments of the basic metasurfaces and the tunable/reconfigurable metasurfaces. In this review, therefore, we would like to summarize the recently developed different kinds of electromagnetic metasurfaces and reconfigurable electromagnetic metasurfaces and devise some new research directions.

Research Progress on Basic Metasurfaces

The main technical realization ways of synthetizing metasurface can be divided into plasmonic-like structure based on metallic materials [36, 37], full dielectric photonic structure based on high refractive index materials [33, 38–40], and other novel structures based on novel thin film materials, semiconductor materials, quantum dots, etc. [33, 36–40, 61, 62]. Most of the reported metasurfaces are used to realize the manipulations of the amplitude, phase, and polarization together with other parameters of the incident electromagnetic waves.

Metasurface for Amplitude Modulation

The metasurface that realizes the amplitude control of electromagnetic waves is mainly used to reflect, absorb, or transmit the incident electromagnetic wave energy. In recent years, a large number of related results have been reported, such

as the broadband metasurface absorber [12–15, 63], metasurface space filter [64, 65], metasurface color printing [66], graphene metasurface anomalous refraction plate [67], dielectric metasurface for selective diffraction [68], and metasurface for near-field plasmonic beam engineering [69], as concluded in **Figure 1**.

Specifically, the representative broadband metasurface absorber shown in **Figure 1A** is fabricated on a flexible substrate by using the nanoscale metal particles arranged in a nonperiodic manner so that the entire metasurface can be conformally mounted on a nonplanar carrier [63]. When the metal particles resonate, the equivalent impedance of the entire metasurface is matched with the free-space wave impedance. The high dielectric loss and magnetic loss generated by the resonance absorb the incident electromagnetic wave energy and the square metal particles have polarization insensitive ability. Thereby the entire metasurface absorber can achieve high-performance absorptions in the near-infrared band and wide angle of incidence. The structure in **Figure 1B** consists of a layer of dielectric metasurface and two layers of distributed Bragg reflectors which can be integrated into various planar optical components [64]. The upper and lower distributed Bragg reflectors form a typical Fabry–Pérot resonator. The metasurface of the middle layer realizes the control of the resonance frequency and constitutes a high-performance (high frequency-selectivity) space electromagnetic wave signal filter. The metasurface in **Figure 1C** consists of a metal plasmonic cell that reproduces the color pattern captured by the camera [66]. Each metal unit resonates with different electromagnetic wave reflection coefficients in the visible frequency region so the human eye can observe different colors. Based on this characteristic, the original color pattern can be reproduced by designing the corresponding metal unit and array, according to the color information of each pixel in the previously taken color photograph.

Moreover, as can be seen in **Figure 1D**, an active metasurface can be formed by integrating graphene into a U-shaped aperture size via a single layer configuration [67]. The hybrid graphene metasurface composed of the artificially constructed two-dimensional metal hole array at the subwavelength scale and the naturally occurring graphene constitutes an electrically steerable amplitude anomalous refraction. Based on the Pancharatnam–Berry phase and the suitable spatially linear phase differences, the amplitude modulation for circularly polarized terahertz wave with anomalous refraction can also be achieved by the effective modulation of the gate voltage. Advanced applications for the dynamic control of electromagnetic waves by electrically tunable graphene metasurfaces such as amplitude tunable active focusing lenses are proposed [67]. More research progress for the dynamic controllable metasurfaces will be discussed in details in the next section. In **Figure 1E**, a complex amplitude modulation based on the ultrathin dielectric metasurface is used to create a new method for independently selecting diffraction orders based on the adjustment of the geometric parameters of the custom nanostructures [68]. **Figure 1F** also shows a near-field plasma beam engineering of metasurface using nanoaperture
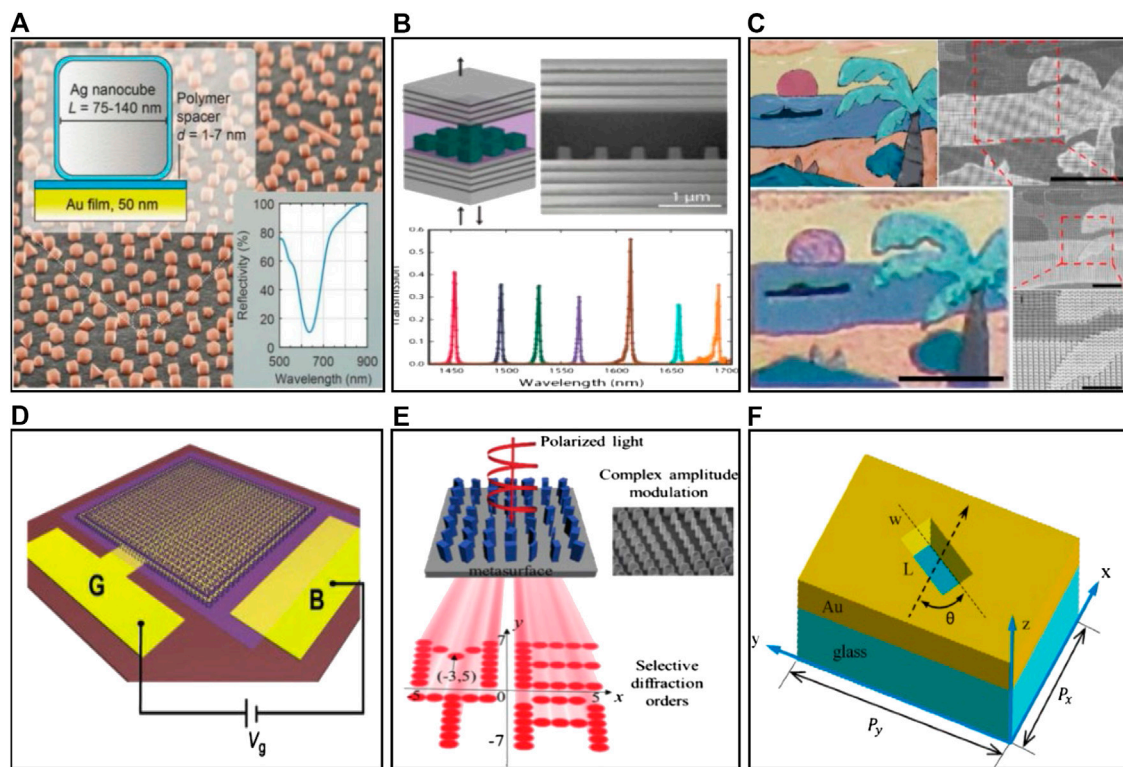
FIGURE 1 | Amplitude-modulated metasurface design and its typical applications. **(A)** Broadband absorber [63], **(B)** spatial filter [64], **(C)** color printing [66], **(D)** graphene metasurfaces [67], **(E)** selective diffraction with a dielectric metasurface [68], and **(F)** a single nanoaperture in one period [69].

arrays to effectively control the complex amplitude of the surface plasmon polaritons in the near-field region [69]. In such a design, each individual nanoaperture is determined pixel by pixel. As a result, the amplitude can be determined by the different lengths of the nanoaperture and the complex amplitude modulation of the surface plasmon polaritons is realized.

Those metasurfaces mentioned above are designed according to the specific application requirements. Each metasurface unit is arranged in a periodic or aperiodic manner to realize the control of the amplitude of the electromagnetic wave. However, when such metasurfaces are designed and developed, their electromagnetic wave amplitude control characteristics are fixed and cannot be changed.

Metasurface for Phase Modulation

On the other hand, the phase response characteristics of metasurface are also closely related to the size, shape, rotation mode, and the substrate material type of the metasurface unit. Therefore, each metasurface unit can be reversely optimized as well as designed according to the specific phase distribution requirements to achieve the phase control of the electromagnetic wave. As early as 2011, N. Yu et al. used eight metasurface elements of different shapes to effectively achieve phase manipulation in the range of 0-2π based on the principle as shown in **Figure 2A** [70]. And a metasurface having flat focusing function and vortex electromagnetic wave generating function

based on the phase manipulation has been developed as can be seen in **Figure 2B** [36, 70, 71].

The phase-modulated metasurface initially reported controls only the crosspolarization component of the incident electromagnetic wave, but most of the common polarization components of the incident electromagnetic wave are not effectively utilized. As a consequence, its electromagnetic wave conversion efficiency is extremely low [62, 72]. To solve this problem, researchers have proposed several kinds of new structures such as Pancharatnam-Berry (P-B) phase metasurface, reflective-type metasurface, Huygens' metasurface, double-layer and multilayer metasurface to realize high-efficient electromagnetic wave manipulation.

P-B phase metasurface. The P-B phase metasurface is a type of structure that can continuously control the phase of electromagnetic waves by changing the rotation angle of the metasurface unit. In 2015, X. Ding et al. designed the P-B phase metasurface structure as shown in the first subplot in **Figure 2C**, and a high-performance flat-focus lens has been developed which achieves nearly 25% electromagnetic wave control efficiency [73]. The same year D. Wen et al. designed a high-efficient holographic imaging plate based on another P-B phase metasurface structure [74], as shown in the second subplot of **Figure 2C**. Moreover, based on the geometric P-B phase, the intracavity laser mode is controlled topologically to achieve a high modulus purity of ~95% [75]. Following the transmissive ultrathin P-B metasurfaces, the photonic spin Hall (PHSE)
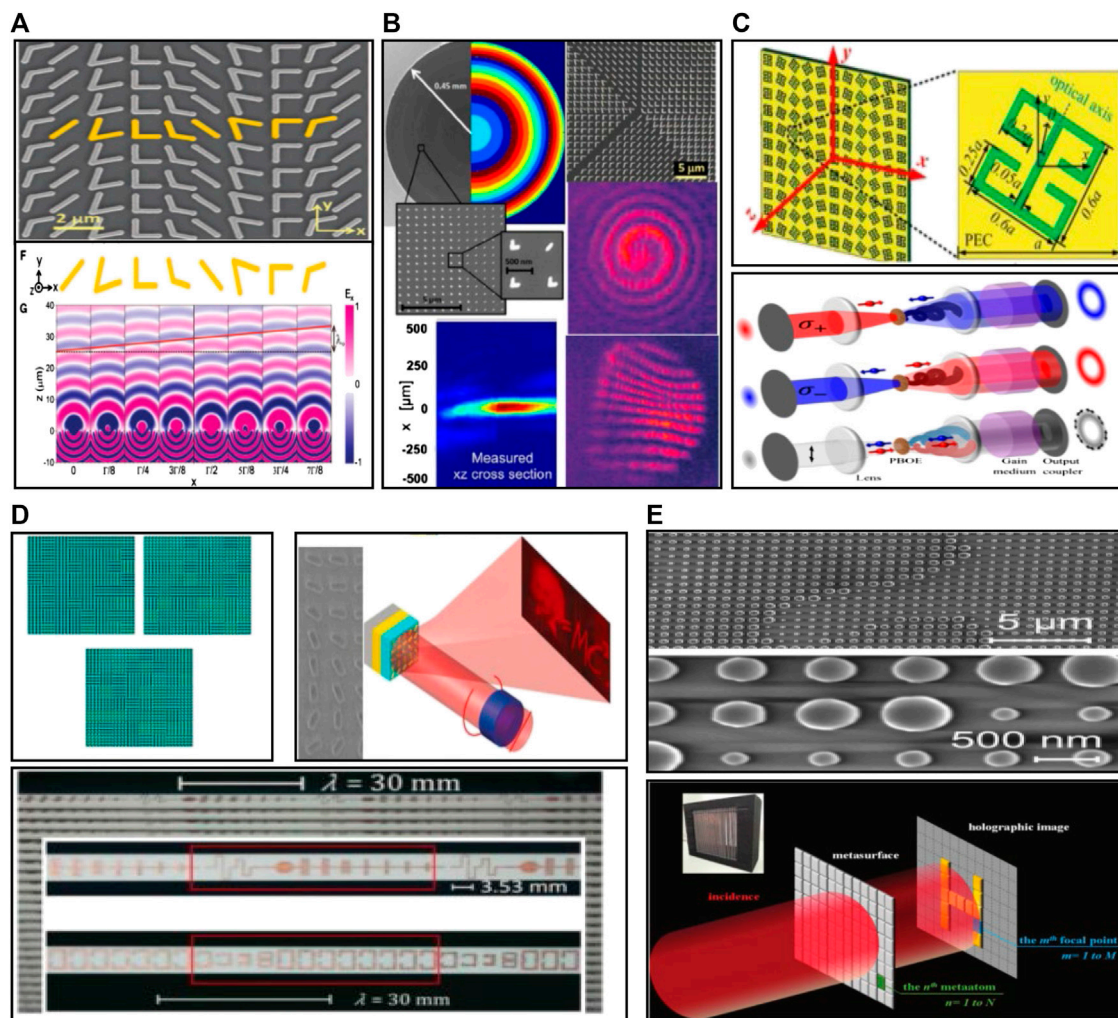
FIGURE 2 | Phase-modulated metasurface design and its typical applications. **(A)** Basic metasurface [70], **(B)** metasurface with focusing and vortex electromagnetic wave generation [36, 70, 71], and **(C)**,**(D)**,**(E)** several examples of high efficiency metasurface design [73, 74, 77–79, 81, 82].

effect can be observed and the efficiency is close to 100%. At the same time, the microwave metasurface with a three-layer structure (total thickness still much smaller than the operating wavelength) is designed (the maximum PSHE efficiency can reach up to 91%), stimulating other P-B metadevices with high efficiency and high performance [76].

Reflective-type metasurface. Moreover, the magnetic resonance characteristics can be formed between the metasurface unit and the metal back-plate in the reflective-type metasurface structures so that the control efficiency of incident electromagnetic waves can be greatly improved. Based on the previously reported P-B phase, a reflective-type P-B phase metasurface with different phases is used combined with different predesigned coding sequences to control the terahertz wave. The coded P-B phase metasurface provides the ability to reduce broadband radar cross section and proposes a flexible way to manipulate reflected terahertz waves [77] as shown in the first subplot of **Figure 2D**. In 2015, G. Zheng et al. designed an I-shaped reflective-type metasurface holographic imaging plate as can be seen in the second subplot of **Figure 2D**, which realized phase control of incident electromagnetic waves with its control efficiency reaching up to 80% [78].

Huygens' metasurface. Based on the Huygens' principle, the Huygens' metasurface which can produce both electric and magnetic resonance was designed to control the electric and magnetic field components of the incident electromagnetic wave. As a result, it has a nearly nonreflecting and completely matching transmission characteristics to maximize the control efficiency of the electromagnetic wave. In 2013, within this frame, C. Pfeiffer et al. designed and developed a Huygens' metasurface with electromagnetic wave control efficiency up to 86% in microwave frequency band [79], as shown in the last subpicture of **Figure 2D**. They also realized the transmission direction control of electromagnetic beam and the Gauss-Bessel beam conversion. Subsequently, C. Pfeiffer et al. further developed a Huygens' metasurface in the near infrared band
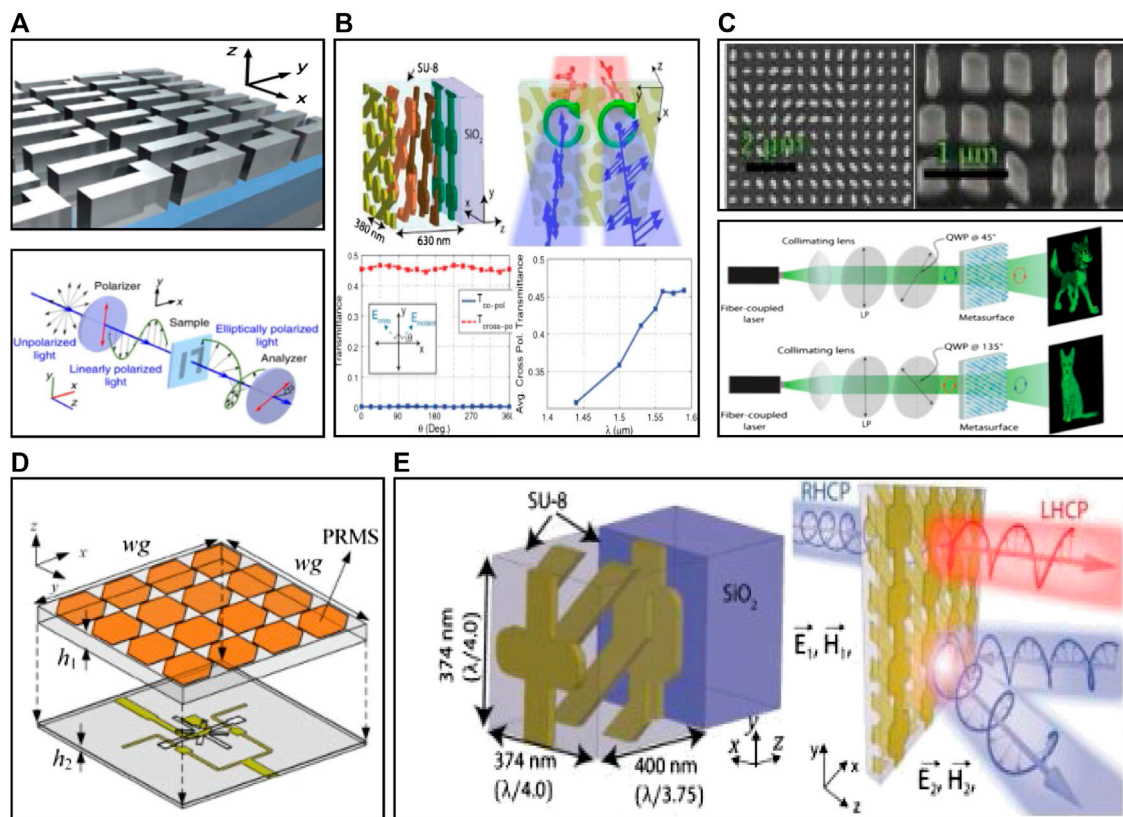
FIGURE 3 | Polarization-modulated metasurface design and its typical applications. **(A)** All-dielectric metasurface [85], **(B),(E)** multilayer metasurface [86, 87], **(C)** holographic metasurfaces that depend on polarization [88], and **(D)** topology of metasurface antenna [90].

[80]. In 2016, L. Wang et al. designed a grayscale metahologram as can be seen in the first subpicture of **Figure 2E**, based on the Huygens' principle. They realized phase control and its control efficiency is up to 99% [81]. In 2018, following the developments of Huygens' metasurface with complete phase shift coverage, Z. Wang et al. proposed a novel Huygens' metasurface hologram at microwave frequency, with detailed studies for the electromagnetic field distribution at the control interface and the energy distribution between the modulation focal points and microwave imaging. This proposed Huygens' metasurface extends the approach of holographic microwave applications [82] as shown in the last subpicture of **Figure 2E**.

In recent years, researchers have also proposed double-layer and multilayer metasurface designs, for further improving the efficiency of controlling the phase of electromagnetic waves. A variety of flat functional devices are reported, e.g., in [83, 84].

As can be seen above, a variety of novel planar devices with beam focusing, transmission direction control, vortex electromagnetic wave generation, holographic imaging, and other functions have been developed using phase-modulated metasurfaces. It is the most well-developed metasurface research areas in recent years. However, the phase-modulated metasurfaces and the realized electromagnetic wave control characteristics based on the planar functional devices have also been defined to be incapable of real-time dynamic tuning.

Metasurface for Polarization Modulation

By designing an asymmetric metasurface unit, the phase difference of the transmitted or reflected electromagnetic waves in the orthogonal direction can be realized. As a result, the control of the polarization direction of the electromagnetic wave and the conversion between various polarization states of the electromagnetic wave were achieved [62, 72]. For example, in 2014, C. Wu et al. developed an all-dielectric metasurface as shown in **Figure 3A** which has Fano's asymmetric resonance characteristics. It can convert linear polarization wave into circular polarization wave radiation [85]. In the same year, C. Pfeiffer et al. developed a multilayer metasurface unit structure as can be seen in **Figure 3B** which can realize the asymmetric transmission of circularly polarized waves and achieve the reversal of polarization states [86]. In 2016, C. Pfeiffer et al. continued to develop a multilayer metasurface structure as shown in **Figure 3E** which can realize the control of the polarization direction of linear polarization waves [87]. In 2017, based on this type of metasurface, J. Mueller et al. designed a holographic metasurface that exhibits different response characteristics for different polarized electromagnetic wave excitations [88] as directed in **Figure 3C**. In the same year, based on the anisotropic metasurfaces, X. Huang et al. achieved the polarization of circularly polarized waves with high conversion efficiency over a wide frequency range [89]. In 2018, W. Yang

et al. proposed a low-profile broadband double-circularly polarized metasurface antenna and thus it can be extended to construct a 2×2 dual circularly polarized antenna array [90] as shown in **Figure 3D**. The working state of the above-reported metasurface, however, also fails to achieve on-demand real-time dynamic tuning.

Metasurface for Multidimensional Modulation

All the above-mentioned metasurfaces are only able to control one single degree of freedom, e.g., amplitude, phase, or polarization of incident electromagnetic waves. In order to achieve more precise control of electromagnetic waves for high-performance holographic imaging and special beam generation, it is necessary to simultaneously control the amplitude and phase (or phase and polarization) of incident electromagnetic waves. For examples, in 2014, L. Liu et al. proposed a combination of amplitude-modulated metasurface units with phase-modulated metasurface units to achieve simultaneous control of amplitude and phase of electromagnetic wave and also developed a broadband metasurface in the THz band [91]. Subsequently, Z. Li et al. designed and developed the nondiffracting beam radiation metasurface in the near-infrared frequency band [92, 93] based on I-shaped metasurface units and C-shaped metasurface units for simultaneous control of electromagnetic wave amplitude and phase. In 2018, G. Lee et al. proposed a new metasurface consisting of X-shaped meta-atoms to achieve full complex amplitude and phase modulation in the broadband visible wavelength region. It was almost comparable to an ideal 3D hologram, and the beam shaping, 3D bioimaging, optical computing, and optical chips can be developed based on such kind of metasurface [94].

Furthermore, in 2015, J. Li et al. proposed a metasurface unit with different rectangular channels which can control simultaneously the polarization and phase of electromagnetic waves so that the circularly polarized incident electromagnetic waves can be converted to linearly polarized waves after passing through such metasurfaces and can deflect the transmission direction of the linear polarized wave [95]. In the same year, A. Arbabi et al. proposed an elliptical all-dielectric metasurface unit structure by designing the ellipticity and with different rotation angles of the metasurface unit. Moreover, they adopted the honeycomb periodic arrangement to realize precise control of the phase and polarization of electromagnetic waves. Based on this metasurface configuration, a variety of high-performance planar functional devices with electromagnetic wave utilization efficiency of up to 97% have been developed, which can realize polarization separation and focusing, polarization transformation and focusing, holographic imaging, and vortex electromagnetic wave generation functions [61].

In 2018, Y. Zhou et al. used lattice design and different arrangements to achieve multifunction reconfigurable metasurface based on amplitude, phase, and polarization modulation fully reflecting the control ability of

electromagnetic wave [96]. At the same time, H. Xu et al. developed a multilayer C-shaped chiral metasurface structure, which was able to control the amplitude, phase, and polarization parameters of electromagnetic waves independently, and proposed several functional flat structures, such as dual focus prisms, airy beams, and multibeam shaping [97]. However, these metasurfaces with multidimensional parameters control ability still cannot achieve real-time dynamic control of incident electromagnetic waves.

Research Progress on Reconfigurable Metasurfaces

The above-reported metasurfaces can control the amplitude, phase, polarization, and other parameters of the electromagnetic wave as needed, and, therefore, it can develop various planar functional devices with novel functions at different frequency regions. However, when those metasurfaces are designed and fabricated, their specific electromagnetic wave characteristic control abilities are limited and cannot be changed, as concluded in previous section. In recent years, in order to achieve higher degree-of-freedom electromagnetic wave control and utilization, active tunable/reconfigurable/ programmable metasurfaces, nonlinear metasurface concepts and design techniques have been proposed [62, 98–103]. As mentioned in the beginning of this review, the electromagnetic response characteristics of the metasurfaces are closely related to the size, shape, rotation direction, and substrate material type of the metasurface unit. As a consequence, the electromagnetic response characteristics of the metasurface can be dynamically controlled by additionally adjusting the metasurface unit structure and the substrate material properties. In turn, the modulations of electromagnetic waves are controlled in real time, that means achieving active tunable, reconfigurable, programmable, and other versatile metasurfaces and versatile optoelectronic devices and systems based on such metasurfaces. The active tunable/reconfigurable metasurface structures that have been reported in recent years include electronic control, light control, temperature control, mechanical control, and power control, which will be discussed in detail in following parts.

Electrically Reconfigurable Metasurfaces

For the tunable metasurfaces loaded by diodes [104], transistors [105], MEMS [106–108], graphene [109], and liquid crystals [110, 111], etc., the electromagnetic response characteristics can be dynamically controlled by adjusting the applied bias voltage on the materials/components in those metasurfaces. For examples, in 2017, K. Chen et al. achieved the electromagnetic response characteristic tuning by biasing voltage on each cell in the reconfigurable metasurface array loaded by the independent/ joint control diodes. Furthermore, the on-demand controlling of the metasurface to the incident electromagnetic wave front was realized and the adjustable focal length was developed [104] as shown in **Figure 4A**. In 2018, O. Yurduseven et al. utilized a PIN diode to dynamically tune the "ON" and "OFF" transition states of a slot-type subwavelength metamaterial unit. The waveguide mode was converted to free-space radiation using a binary
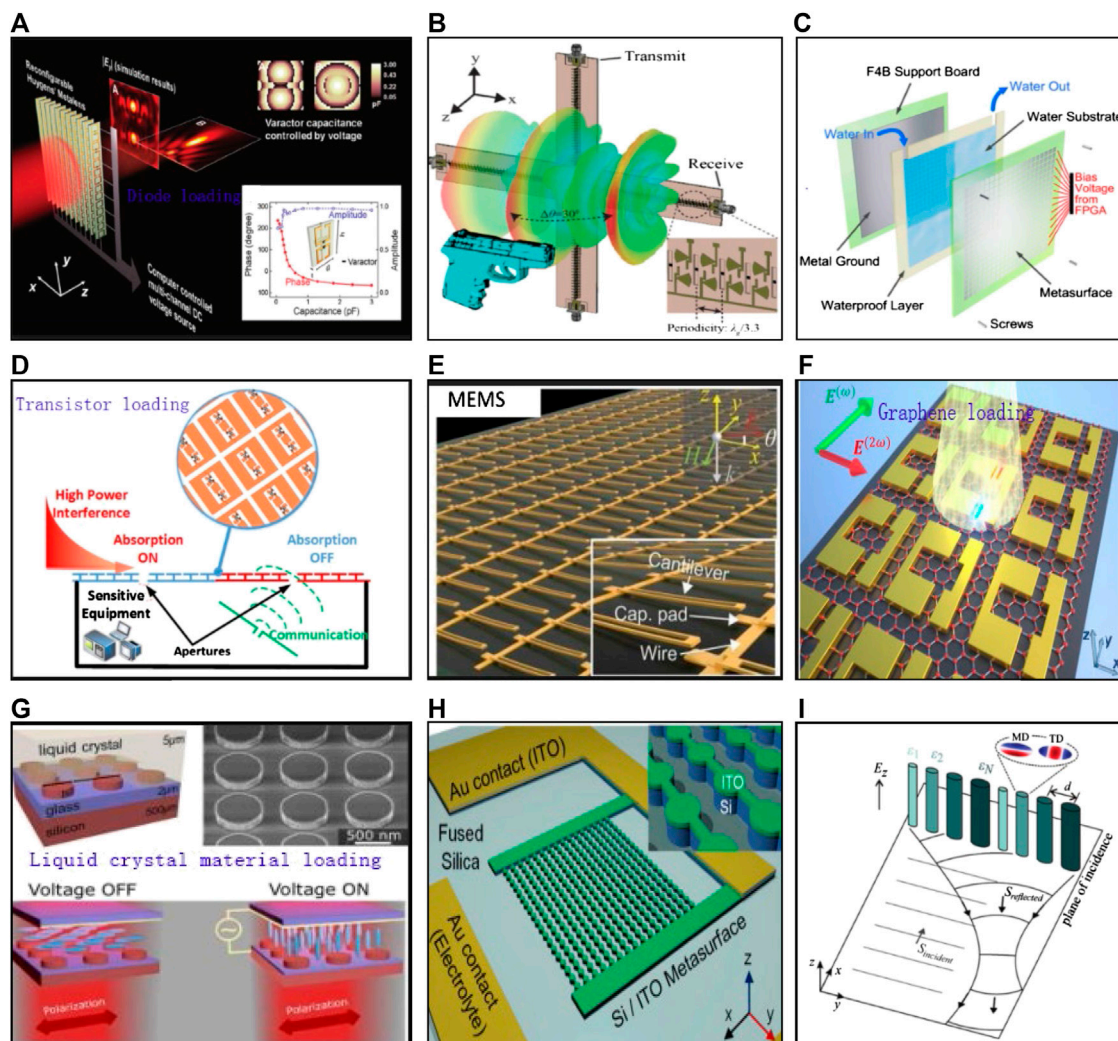
FIGURE 4 | A variety of electrically reconfigurable metasurface designs. **(A)** Loaded with diodes for focal length control [104], **(B)** loaded with PIN diodes for microwave camera [112], **(C)** loaded with PIN diodes and water for X-stage wave front control [114], **(D)** loaded with transistor switchable absorbing control [105], **(E)** loaded with MEMS for polarization control [106], **(F)** loaded with graphene for different functions switching [109], **(G)** loaded with liquid crystal for reconfigurable multiband spin-selective light absorption [110, 111], **(H)** loaded with ITO for focus control [125], and **(I)** loaded with magnetic dipole for reconfigurable wave front manipulation [126].

adjustment to form a target radiation pattern. Then a dynamically reconfigurable holographic metasurface aperture that allows for electron beam steering purposes was designed. And a synthetic K-band Mills-Cross monochrome microwave camera can be set up to achieve high fidelity images [112], seen in **Figure 4B**. In 2018, X. Gao et al. proposed an active metasurface composed of a butterfly-shaped unit cells embedded with the voltage-controlled varactor diodes. The reconfigurable polarization converter was dynamically converted from linear to linear, linear to elliptical, and linear to circular by adjusting the bias voltage of the varactor [113]. In 2019, L. Chen et al. proposed a reconfigurable metasurface using the voltage control of the PIN diode and the control of the salinity of the water matrix so that the metasurface can flexibly control the amplitude and deflection angle of the scattered beam. In turn, the X-stage wave front of the

reconfigurable water-based metasurface was controlled [114], as shown in **Figure 4C**. Moreover, in 2017, A. Li et al. developed a broadband absorbing material with adjustable switch control and absorbing power by loading transistors in the absorbing metasurface unit and adjusting the bias voltage applied to each transistor [105], as shown in **Figure 4D**.

Moreover, in 2018, X. Zhao et al first designed a MEMS-loaded reconfigurable metasurface as can be seen in **Figure 4E** by controlling the resonant characteristics of the metasurface unit through adjusting the magnitude of the bias voltage, thereby, achieving the control of the polarization state of the incident electromagnetic wave [106]. E. Arbabi et al. prepared a metasurface lens on the MEMS cantilever and controlled the position of the transmitted electromagnetic wave focus by adjusting the bias voltage [107], and, at the same time,
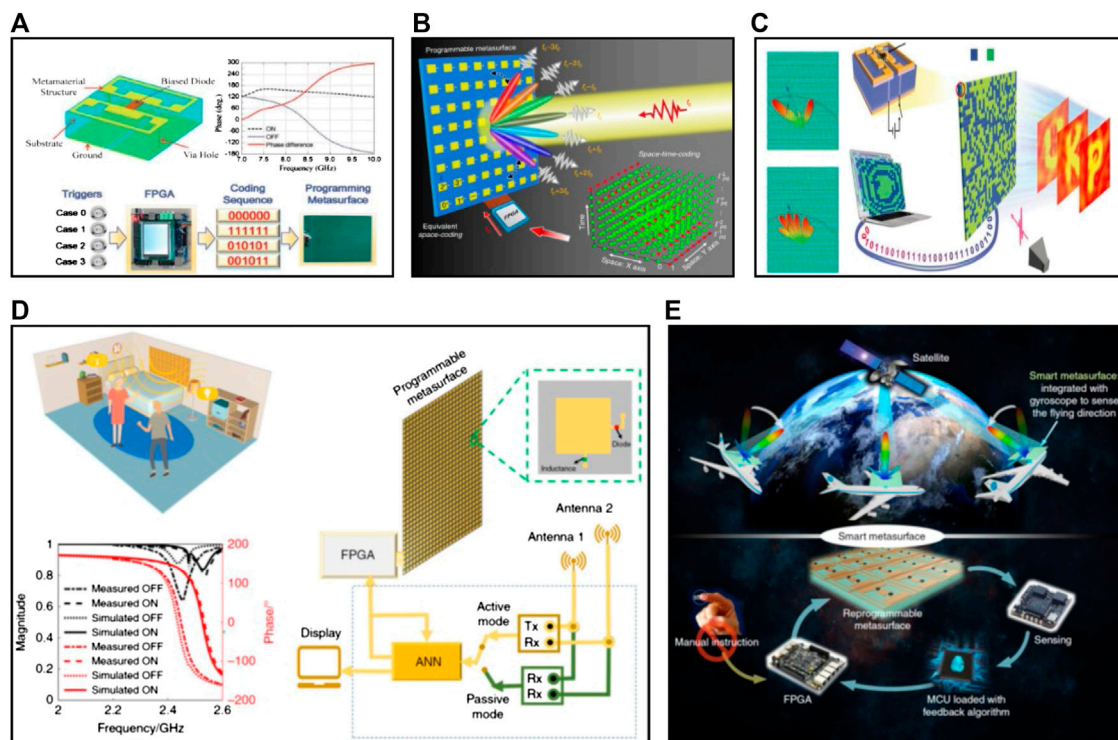
FIGURE 5 | Coding and programmable metasurface structure and its application. **(A)** Basic programmable metasurface [99], **(B)** space-time modulated digital coding metasurface [127], **(C)** reconfigurable holographic imaging metasurface [128], and **(D),(E)** smart metasurface [129, 130].

M. Manjappa et al. realized a simple logic signal processing in the THz band based on the MEMS-loaded dual SRR metasurface structure [108].

In addition, S. R. Biswas et al. theoretically proved that when the graphene material was loaded into the reflective metasurface, by changing the bias voltage of the graphene, the on-demand switching between the beam orientation/focus and electromagnetic cloak can be realized [109], seen in **Figure 4F**. As a result, the tunable frequency and/or amplitude modulation can be achieved [115, 116]. After that, many high-performance graphene-based tunable/reconfigurable metasurfaces are reported with different kinds of functions, including the tunable polarization switching/converting and beam steering [117, 118], broadband and tunable perfect absorber [119–122], and even programmable metasurface [123, 124] which will be discussed later. Moreover, A. Komar et al. and D. Xiao et al. have proposed the designs for integrating liquid crystals into metasurface arrays. By adjusting the bias voltage applied to the liquid crystals, the controlling of the metasurface resonance frequency as well as the on-demand selective absorption of electromagnetic waves of different polarizations was achieved [110, 111], as shown in **Figure 4G**. A. Howes et al. loaded the ITO material layer in the metasurface array and realized the electromagnetic wave transmittance controlling by adjusting the bias voltage on the ITO material. Finally they realized the reconfigurable focus beam [125], seen **Figure 4H**. In 2018, O. Tsilipakos et al. used a magnetic dipole with a ring dipole

resonator in the metasurface unit made of an elliptical dielectric rod. When the rod dielectric constant is changed, the effect of accurately matching the two resonances can be achieved, realizing the manipulation of constructing a tunable gradient metasurface and reconfiguring its wave front [126], seen in **Figure 4I**.

This type of reconfigurable metasurface is voltage controlled and has the characteristics of simple tuning abilities. However, it is difficult to achieve on-demand independent control of each single metasurface unit for material-loaded metasurfaces discussed above. Therefore, there are no reports of metasurface applications with better functional performance. Fortunately, in view of the engineering feasibility of electronically controlled reconfigurable metasurface loaded by diodes, the researchers further proposed the idea of coding and reprogrammable metasurface designs. Quite recently, researchers from Southeast University in China have systematically studied the working principle as well as design method of digital coding metasurface and reprogrammable metasurface [99], as shown in **Figure 5A**. For example, in 2018, L. Zhang et al. proposed the concept of space-time modulated digital coding metasurface to achieve the simultaneous manipulation of electromagnetic wave frequency domain and space; thereby, harmonic beam control was achieved [127], as shown in **Figure 5B**. The design principle of the space-time digital coded metasurface can be applied to various aspects such as wireless
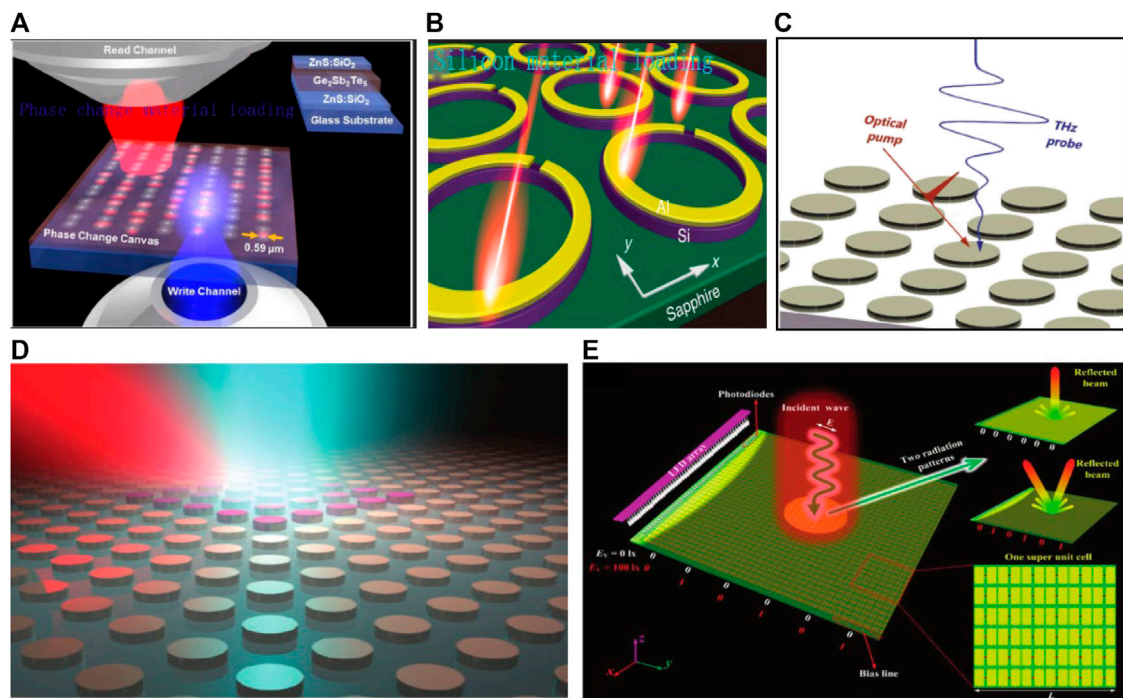
FIGURE 6 | Optically reconfigurable metasurface. **(A)** Loaded with phase change material [131], **(B)** loaded with additional silicon ring layer [132], **(C)** loaded with ion-implanted silicon layer [133], **(D)** loaded with specific dielectric materials [134], and **(E)** loaded with photodiodes [135].

communication and holographic imaging. Other functional devices such as reconfigurable holographic imaging metasurfaces with transformable multibeam radiation have also been developed [128] as shown in **Figure 5C**. Based on the breakthroughs obtained by the T. Cui's research group, the smart metasurface imager and recognizer empowered by a network of artificial neural network (ANNs) for the adaptive control data flow and the smart metasurface that has self-adaptive reprogrammable functions without human participation have been designed [129, 130], as shown in **Figures 5D and 5E**.

Optically Reconfigurable Metasurface

In recent years, researchers have also proposed to load photosensitive materials as well as devices into metasurface structures to achieve optically reconfigurable metasurface by adjusting the intensity of light sources. For examples, in 2016, Q. Wang et al. used a phase change material (chalcogenide GST) as the metasurface substrate material to realize a light-controlled dual-focus reconfigurable metasurface structure [131], seen in **Figure 6A**. In 2018, L. Cong et al. used a layer of silicon ring between a conventional C-shaped metasurface unit and a sapphire substrate, as shown in **Figure 6B**. By changing the intensity of the pump light, fast switching of the polarization state of the incident electromagnetic wave and rapid separation of the copolarized/cross-polarized wave were achieved [132]. In the same year, H. Cai et al. designed an ultrafast tunable metasurface consisting of an array of ion-implant combined with annealed silicon disk using optical pump terahertz probe

spectroscopy to perform ultrafast and efficient all-optical tuning of silicon-based metasurfaces, seen in **Figure 6C**, in turn, achieving ultra-fast effective all-optical modulation of THz waves [133].

In 2018, K. Fan et al. overcame the static geometric tuning characteristics of traditional dielectric metasurfaces, by controlling the resonant eigenmodes through optical excitation. The optically tunable characteristics of the dynamic dielectric Huygens' metasurface were proposed and verified, which has great significance for the application of metasurface reconfigurability, as shown in **Figure 6D** [134]. In addition, the T. Cui's group from Southeast University integrated the photodiode into the metasurface array to develop the light-controlled reconfigurable metasurface structure by digitally encoding the LED illumination state, as shown in **Figure 6F** [135]. However, the use of additional light sources to control the electromagnetic response characteristics of metasurface unit to achieve reconfigurable function increases the complexity as well as cost of the system to some extent.

Thermally Reconfigurable Metasurface

It is well known that some of the substrate materials described above such as silicon, liquid crystal, and phase change material GST are sensitive to bias voltage, light intensity, and also the background temperature. Based on the temperature sensitivity of these materials, researchers have proposed thermally reconfigurable metasurfaces in recent years. As can be seen in **Figures 7A** and **7B**, the Y. Kivshar's Group of the Australian National University has used silicon and liquid crystal as the
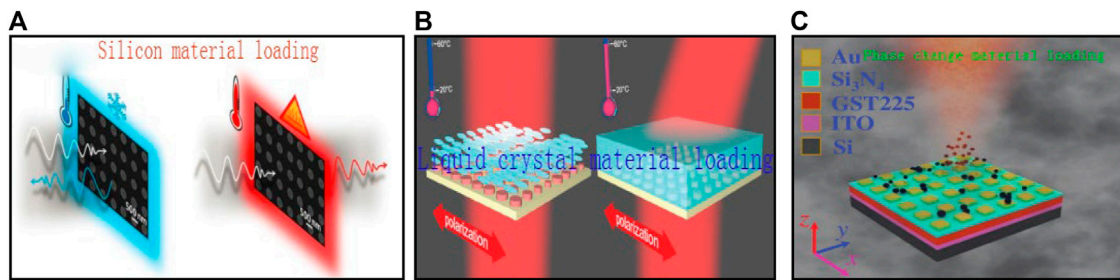
FIGURE 7 | Thermally reconfigurable metasurface. **(A)** Loaded with silicon [136], **(B)** loaded with liquid crystal [137], and **(C)** loaded with phase change material [140].
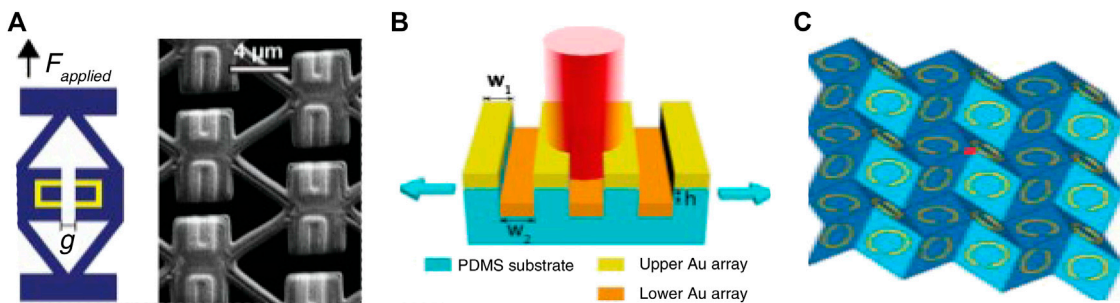

FIGURE 8 | Mechanical reconfigurable metasurface [132–134].

substrate material of the metasurface. By adjusting the temperature around the metasurface, it can realize the dynamic control of the reflection/transmission of incident electromagnetic waves and dynamic control of the transmission direction of incident electromagnetic waves [136, 137]. W. Dong et al. achieved the adjustment of the transmitted electromagnetic wave operating band by using the temperature-sensitive phase-change material GST loaded into metasurface [138]. In 2018, H. Cai et al. proposed a vanadium dioxide-based hybrid metasurface and the hybrid metasurface can realize the control of transmission of terahertz waves by heating, or optical pumping [139]. In the same year, J. Tian et al. used a phase change material such as $Ge_2Sb_2Te_5$ (GST) to switch the material phase state between a crystal and an amorphous crystal by changing the temperature to switch the response of the meta-atom between an electric and a magnetic dipole. The phase shift generated by the multistage resonance realizes wave front manipulation. It will contribute to the development of future optical communication networks [140]. At the same time, X. Chen et al. used shape memory alloy as the metasurface substrate material and changed the shape of the memory alloy by adjusting the ambient temperature to develop a transmissive metasurface structure with tunable working frequency band [141]. The thermally reconfigurable metasurface provides a solution to a certain extent, but the prepared metasurface was greatly affected by

the environmental temperature changings. Aside from that, its practicability and operability are limited.

Mechanically Reconfigurable Metasurface

When the metasurface array was prepared on the elastic/flexible substrate material, the shape of the elastic/flexible substrate material can be mechanically adjusted. As a result, the electromagnetic response of the metasurface unit could also be changed, to achieve a mechanically reconfigurable metasurface. In 2018, J. Reeves et al. designed a metasurface as directed in **Figure 8A**. The C-shaped metasurface unit was prepared on a soft polymer scaffold by additional stretching/compression soft polymerization. The object holder can control the spacing of two C-shaped units in the metasurface unit to realize the mechanical reconfigurable metasurface structure [142]. X. Liu et al. also proposed a noncoplanar metasurface structure as shown in **Figure 8B**. The two-layer metasurface array was fabricated on a PDMS flexible substrate. The mechanically reconfigurable metasurface was achieved by stretching the PDMS flexible material to change the coupling characteristics between the two metasurface arrays [143].

In addition, Z. Wang et al. prepared a C-shaped metasurface unit on a foldable dielectric substrate as can be seen in **Figure 8C**. Different chiral responses to incident electromagnetic waves were achieved by changing the folding mode of the dielectric substrate [144]. L. Chen et al. changed the distance of the reflective surface
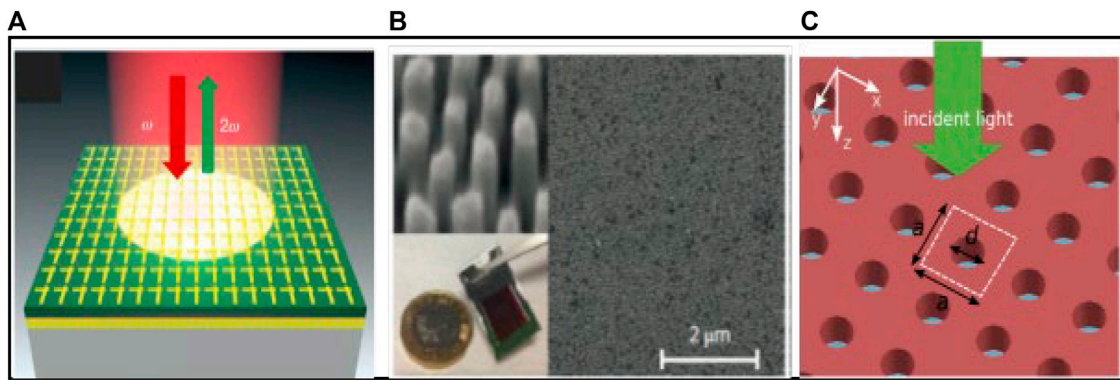
FIGURE 9 | Nonlinear metasurface and power reconfigurable metasurface [136–138].

of the metasurface metal reflective surface from the metasurface layer by mechanical means to realize the reconfigurable function of the reflected beam [145]. The mechanical reconfigurable metasurface provides a feasible solution for real-time dynamic control of electromagnetic waves. However, its mechanical control system is complex and it is difficult to achieve precise control with the high-performance metasurface applications.

Power Reconfigurable Metasurface

In addition, researchers have proposed the design idea of nonlinear metasurface to achieve the generation of higher harmonics and manipulation of its characteristics [100]. In 2014, J. Lee et al. developed an asymmetric cross-shaped unit and a metasurface array using the principle of electron complementary band transition in a semiconductor heterostructure. As a result, a second-order nonlinear harmonic output with high conversion efficiency was achieved [146] as shown in **Figure 9A**. In 2017, based on the relationship between electromagnetic response characteristics of the nonlinear metasurface and the incident electromagnetic wave intensity, L. Nicholls et al. designed a metasurface that can quickly adjust the polarization direction of the electromagnetic wave as shown in **Figure 9B**. The nonlinear metasurface was able to realize the polarization deflection of electromagnetic waves of up to 60° under the excitation of electromagnetic waves with different intensities [147]. In 2018, Y. Xu et al. used chalcogenide glass to prepare a full-dielectric metasurface as can be seen in **Figure 9C**. Based on the high nonlinearity of chalcogenide glass, the switching control of the vortex electromagnetic wave state was achieved by adjusting the incident electromagnetic wave intensity [148]. In 2018, L. Wang et al. proposed a nonlinear all-dielectric metasurface which generates a third harmonic signal and efficiently controls the nonlinear wave front of any complex parameter wave generated by it. Its control efficiency can reach up to 92% [149]. The nonlinear metasurface energy can realize the reconfigurable property of the electromagnetic wave self-control ability simply by adjusting the incident electromagnetic wave intensity. However, in the reported nonlinear metasurface, it is difficult to effectively control each single metasurface unit, so a more versatile reconfigurable metasurface structure is hard to be realized.

In recent years, optomechanical nonlinear metasurfaces [149–151] have received wide attention as a new class of nonlinear metasurfaces. The metal/nonmetal resonant unit in the optomechanical metasurface is prepared on the elastic material matrix or the resonant unit itself is suspended to form an elastic structure. Under the excitation of the incident electromagnetic wave, the field-structure interaction will generate optical gradient force, electromagnetic induction force, and/or thermal expansion force. The optomechanical metasurface can control the self-polarization state of incident electromagnetic waves by adjusting the intensity of incident electromagnetic waves [150, 151]. The nonlinear characteristics of optomechanical metasurfaces are derived from the mutual coupling effect of incident electromagnetic wave energy and metasurface unit structure potential energy.

DISCUSSION AND PERSPECTIVE

As can be seen above, the researches on electromagnetic metasurface have made remarkable progress in mechanism discovery, analytical theory breakthrough, application innovation, etc. In recent years, a variety of metasurface implementation methods have been proposed to design metasurfaces with various electromagnetic wave response characteristics to achieve the electromagnetic wave amplitude, phase, polarization direction/ state, orbital angular momentum, and spin angular momentum control. Based on the metasurfaces breakthrough, a variety of novel planar function devices and systems with microwave, THz, and optical frequency bands have been developed. For the various metasurfaces, especially the active tunable/reconfigurable/ programmable ones, some of them already realized to independently control each metasurface unit.

In the near future, the metasurface can be further widely developed, with more efficient [24, 31, 76, 97, 118], wider operating bandwidth [12, 42, 118, 119] and easier fabrication and lower cost [152, 153]. Most importantly, metasurface can be designed based the cutting-edge techniques, including the artificial intelligent, to achieve the intelligent metasurface and smart metasurface, which are proposed in the past two years

[129, 130, 154–157]. This should be the most exciting research area in the metasurface research community.

CONCLUSION

This review firstly discussed the previously well-developed electromagnetic metasurfaces, in terms of the different kinds of modulations, including the magnitude, phase, and/or polarization modulations. Then, based on the analysis of the aforementioned metasurfaces which cannot realize the dynamic control, the active/tunable/reconfigurable metasurfaces based on various materials/components loadings are analyzed, in terms of the different kinds of control methods, including the electrically, optically, thermally, mechanically, and power reconfigurable/ control techniques. In the end, the cutting-edge metasurface design idea based on mechanical learning, deep learning, is pointed out. This review concluded the main research directions in the past several years and it has important value for the metasurface research community.

AUTHOR CONTRIBUTIONS

SZ, LM, WW, JL, and YH discussed together and proposed the review content. LM, YH, and GW modified the review frame. DC, YL, YZ, and NL finished the references collection and figure preparation. SZ and WW finished the whole manuscript writing, and LM, JL, YH, and GW carried out the whole manuscript modification and finalization. All authors contributed to the proofreading. SZ and LM contributed equally to this work.

FUNDING

REFERENCES

1. Cui TJ, Smith DR, Liu R. *Metamaterials: theory, design and applications*. New York, NY: Spring-Verlag (2010).
2. Sakai O, Tachibana K. Plasmas as metamaterials: a review. *Plasma Sources Sci Technol* (2012) 21(1):013001. doi:10.1088/0963-0252/21/1/013001
3. Wang Z, Cheng F, Winsor T, Liu Y. Optical chiral metamaterials: a review of the fundamentals, fabrication methods and applications. *Nanotechnology* (2016) 27(41):412001. doi:10.1088/0957-4484/27/41/412001
4. Ren X, Das R, Tran P, Ngo TD, Xie YM, et al. Auxetic metamaterials and structures: a review. *Smart Materials Structures* (2018) 27(2):023001. doi:10.1088/1361-665X/aaa61c
5. Cummer SA, Christensen J, Alù A. Controlling sound with acoustic metamaterials. *Nat Rev Materials* (2016) 1(3):1–13. doi:10.1038/natrevmats.2016.1
6. Yu X, Zhou J, Liang H, Jiang Z, Wu L. Mechanical metamaterials associated with stiffness, rigidity and compressibility: a brief review. *Prog Mater Sci* (2018) 94:114–73. doi:10.1016/j.pmatsci.2017.12.003
7. Chen HT, Padilla WJ, Zide JM, Gossard AC, Taylor AJ, Averitt RD. Active terahertz metamaterial devices. *Nature* (2006) 444(7119):597–600. doi:10.1038/nature05343
8. Dong Y, Itoh T. Metamaterial-based antennas. *Proc IEEE* (2012) 100(7):2271–85. doi:10.1109/JPROC.2012.2187631
9. Oliveri G, Werner DH, Massa A. Reconfigurable electromagnetics through metamaterials: a review. *Proc IEEE* (2015) 103(7):1034–56. doi:10.1109/JPROC.2015.2394292
10. Huang Y, Wu Z, Li J, Lv W, Xie F, Wen G, et al. Dynamics analysis of a pair of ring resonators in liquid media. *Phys Rev Appl* (2018) 10:044026. doi:10.1103/PhysRevApplied.10.044026
11. Lv W, Xie F, Huang Y, Li J, Fang X, Rashid A, et al. Nonlinear coupling states study of electromagnetic force actuated plasmonic nonlinear metamaterials. *Optic Express* (2018) 26:3211–20. doi:10.1364/OE.26.003211
12. Yu P, Besteiro LV, Huang Y, Wu J, Fu L, Tan HH, et al. Broadband metamaterial absorbers. *Adv Opt Mater* (2019) 7:1800995. doi:10.1002/adom.201800995
13. Yu P, Besteiro LV, Wu J, Huang Y, Wang Y, Govorov AO, et al. Metamaterial perfect absorber with unabated size-independent absorption. *Optic Express* (2018) 26:20471–80. doi:10.1364/OE.26.020471
14. Huang Y, Wen G, Zhu W, Li J, Si LM, Premaratne M. Experimental demonstration of a magnetically tunable ferrite based metamaterial absorber. *Optic Express* (2014) 22:16408–17. doi:10.1364/OE.22.016408
15. Zhu W, Huang Y, Rukhlenko I, Wen G, Premaratne M. Configurable metamaterial absorber with pseudo wideband spectrum. *Optic Express* (2012) 20(6):6616–21. doi:10.1364/OE.20.006616
16. Li Y, Zhu KJ, Peng YG, Li W, Yang T, Xu HX, et al. Thermal meta-device in analogue of zero-index photonics. *Nat Mater* (2019) 18(1):48–54. doi:10.1038/s41563-018-0239-6
17. Luo X. Subwavelength optical engineering with metasurface waves. *Adv Opt Mater* (2018) 6:1701201. doi:10.1002/adom.201701201
18. Kildishev AV, Boltasseva A, Shalaev VM. Planar photonics with metasurfaces. *Science* (2013) 339(6125):1232009–6. doi:10.1126/science.1232009
19. Lin D, Fan P, Hasman E, Brongersma ML. Dielectric gradient metasurface optical elements. *Science* (2014) 345(6194):298–302. doi:10.1126/science.1253213
20. Holloway CL, Kuester EF, Gordon JA, O'Hara J, Booth J, Smith DR. An overview of the theory and applications of metasurfaces: the two-dimensional equivalents of metamaterials. *IEEE Antenn Propag Mag* (2012) 54(2):10–35. doi:10.1109/MAP.2012.6230714
21. Fan Y, Shen N, Zhang F, Zhao Q, Wei Z, Zhang P, et al. Photoexcited graphene metasurfaces: significantly enhanced and tunable magnetic resonances. *ACS Photon* (2018) 5(4):1612–1618. doi:10.1021/acsphotonics.8b00057
22. Huang Y, Yang L, Li J, Wang Y, Wen G. Polarization conversion of metasurface for the application of wide band low-profile circular polarization slot antenna. *Appl Phys Lett* (2016) 109:054101. doi:10.1063/1.4960198

23. Li Z, Premaratne M, Zhu W. Advanced encryption method realized by secret shared phase encoding scheme using a multi-wavelength metasurface. *Nanophotonics* (2020) 9:20200298. doi:10.1515/nanoph-2020-0298

24. Bai X, Kong F, Sun Y, Wang G, Qian J, Li X, et al. High-efficiency transmissive programmable metasurface for multimode OAM generation. *Adv Opt Mater* (2020) 8:202000570. doi:10.1002/adom.202000570

25. Akram MR, Ding G, Chen K, Feng Y, Zhu W. Ultrathin single layer metasurfaces with ultra-wideband operation for both transmission and reflection. *Adv Mater* (2020) 32(12):e1907308. doi:10.1002/adma.201907308

26. Hu G, Hong X, Wang K, Wu J, Xu HX, Zhao W, et al. Coherent steering of nonlinear chiral valley photons with a synthetic Au–WS 2 metasurface. *Nat Photon* (2019) 13(7):467–72. doi:10.1038/s41566-019-0399-1

27. Xu HX, Han L, Li Y, Sun Y, Zhao J, Zhang S, et al. Completely spin-decoupled dual-phase hybrid metasurfaces for arbitrary wavefront control. *ACS Photon* (2018) 6(1):211–20. doi:10.1021/acsphotonics.8b01439

28. Li C, Yu P, Huang Y, Zhou Q, Wu J, Li Z, et al. Dielectric metasurfaces: from wavefront shaping to quantum platforms. *Prog Surf Sci* (2020) 95(2):100584. doi:10.1016/j.progsurf.2020.100584

29. Huang Y, Li J, Xu HX, Yu H, Yang Z, Yu P, et al. Experimental demonstration of microwave two-dimensional Airy beam generation based on single-layer metasurface. *IEEE Trans Antenn Propag* (2020) 68(11):7507–16. doi:10.1109/TAP.2020.2996826

30. Xu HX, Hu G, Jiang M, Tang S, Wang Y, Wang C, et al. Wavevector and frequency multiplexing performed by a spin-decoupled multichannel metasurface. *Advan Mater Tech* (2020) 5(1):1900710. doi:10.1002/admt.201900710

31. Dai JY, Yang LX, Ke JC, Chen MZ, Tang W, Li X, et al. High-efficiency synthesizer for spatial waves based on space-time-coding digital metasurface. *Laser Photon Rev* (2020) 14(6):1900133. doi:10.1002/lpor.201900133

32. Li H, Li YB, Shen JL, Cui TJ. Low-profile electromagnetic holography by using coding fabry–perot type metasurface with in-plane feeding. *Advan Optical Mater* (2020) 8(9):1902057. doi:10.1002/adom.201902057

33. Zhang XG, Yu Q, Jiang WX, Sun YL, Bai L, Wang Q, et al. Polarization-controlled dual-programmable metasurfaces. *Advan Sci* (2020) 7(11):1903382. doi:10.1002/advs.201903382

34. Wu RY, Bao L, Wu LW, Wang Z, Ma Q, Wu JW, et al. Independent control of copolarized amplitude and phase responses via anisotropic metasurfaces. *Advan Optical Mater* (2020) 8(9):1902126. doi:10.1002/adom.201902126

35. Zhang XG, Jiang WX, Jiang HL, Wang Q, Tian H, Bai L, et al. An optically driven digital metasurface for programming electromagnetic functions. *Nat Electron* (2020) 3(3):165–71. doi:10.1038/s41928-020-0380-5

36. Yu N, Capasso F. Flat optics with designer metasurfaces. *Nat Mater* (2014) 13(2):139–50. doi:10.1038/nmat3839

37. Meinzer N, Barnes WL, Hooper IR (2014). Plasmonic meta-atoms and metasurfaces. *Nat Photon.* 8(12):889–98. doi:10.1038/nphoton.2014.247

38. Khorasaninejad M, Capasso F. Perfect anomalous reflection with a bipartite Huygens' metasurface. *Science* (2017) 358:eaam8100. doi:10.1126/science.aam8100

39. Wong AMH, Eleftheriades GV. Perfect anomalous reflection with a bipartite Huygens' metasurface. *Phys Rev X* (2018) 8(1):11036. doi:10.1103/PhysRevX.8.011036

40. Kamali SM, Arbabi E, Arbabi A, Faraon A. A review of dielectric optical metasurfaces for wavefront control. *Nanophotonics* (2018) 7(6):1041–68. doi:10.1515/nanoph-2017-0129

41. Nagarajan A, van Erve K, Gerini G. Ultra-narrowband polarization insensitive transmission filter using a coupled dielectric-metal metasurface. *Optic Express* (2020) 28(1):773–87. doi:10.1364/OE.383781

42. Sun D, Qi L, Liu Z. Terahertz broadband filter and electromagnetically induced transparency structure with complementary metasurface. *Results Phys* (2020) 16:102887. doi:10.1016/j.rinp.2019.102887

43. Zhang Z, Yang Q, Gong M, Chen M, Long Z. Metasurface lens with angular modulation for extended depth of focus imaging. *Opt Lett* (2020) 45(3):611–4. doi:10.1364/OL.382812

44. Sung J, Lee GY, Lee B. Progresses in the practical metasurface for holography and lens. *Nanophotonics* (2019) 8(10):1701–18. doi:10.1515/nanoph-2019-0203

45. Yuan Y, Zhang K, Ratni B, Song Q, Ding X, Wu Q, et al. Independent phase modulation for quadruplex polarization channels enabled by chirality-assisted geometric-phase metasurfaces. *Nat Commun* (2020) 11(1):4186–9. doi:10.1038/s41467-020-17773-6

46. Yuan Y, Sun S, Chen Y, Zhang K, Ding X, Ratni B, et al. A fully phase-modulated metasurface as an energy-controllable circular polarization router. *Adv Sci* (2020) 7(18):2001437. doi:10.1002/advs.202001437

47. Castaldi G, Zhang L, Moccia M, Hathaway AY, Tang W, Cui TJ, et al. Joint multi-frequency beam shaping and steering via space-time-coding digital metasurfaces. *Adv Funct Mater* (2020) 2020:2007620. doi:10.1002/adfm.202007620

48. Wei Q, Huang L, Zentgraf T, Wang Y. Optical wavefront shaping based on functional metasurfaces. *Nanophotonics* (2020) 9:478. doi:10.1515/nanoph-2019-0478

49. Ren H, Briere G, Fang X, Ni P, Sawant R, Héron S, et al. Metasurface orbital angular momentum holography. *Nat Commun* (2019) 10(1):2986–8. doi:10.1038/s41467-019-11030-1

50. Hermon S, Ma A, Yue F, Kubrom F, Intaravanne Y, Han J, et al. Metasurface hologram for polarization measurement. *Opt Lett* (2019) 44(18):4436–8. doi:10.1364/OL.44.004436

51. Hedayati MK, Elbahri M. Review of metasurface plasmonic structural color. *Plasmonics* (2017) 12(5):1463–79. doi:10.1007/s11468-016-0407-y

52. Imani MF, Gollub JN, Yurduseven O, Diebold AV, Boyarsky M, Fromenteze T, et al. Review of metasurface antennas for computational microwave imaging. *IEEE Trans Antenn Propag* (2020) 68(3):1860–75. doi:10.1109/TAP.2020.2968795

53. Amer AAG, Sapuan SZ, Nasimuddin N, Alphones A, Zinal NB. A comprehensive review of metasurface structures suitable for RF energy harvesting. *IEEE Access* (2020) 8:76433–52. doi:10.1109/ACCESS.2020.2989516

54. Bukhari SS, Vardaxoglou JY, Whittow W. A metasurfaces review: definitions and applications. *Appl Sci* (2019) 9(13):2727. doi:10.3390/app9132727

55. Ding F, Bozhevolnyi SI. A review of unidirectional surface plasmon polariton metacouplers. *IEEE J Sel Top Quant Electron* (2019) 25(3):1–11. doi:10.1109/JSTQE.2019.2894067

56. Ding F, Pors A, Bozhevolnyi SI. Gradient metasurfaces: a review of fundamentals and applications. *Rep Prog Phys* (2017) 81(2):026401. doi:10.1088/1361-6633/aa8732

57. Ding F, Yang Y, Deshpande RA, Bozhevolnyi SI. A review of gap-surface plasmon metasurfaces: fundamentals and applications. *Nanophotonics* (2018) 7(6):1129–56. doi:10.1515/nanoph-2017-0125

58. Hu J, Bandyopadhyay S, Liu Y. A review on metasurface: from principle to smart metadevices. *Front Phys* (2020) 8:502. doi:10.3389/fphy.2020.586087

59. Chen HT, Taylor AJ, Yu N. A review of metasurfaces: physics and applications. *Rep Prog Phys* (2016) 79(7):076401. doi:10.1088/0034-4885/79/7/076401

60. Deng ZL, Li G. Metasurface optical holography. *Mater Today Phys* (2017) 3:16–32. doi:10.1016/j.mtphys.2017.11.001

61. Arbabi A, Horie Y, Bagheri M, Faraon A. Dielectric metasurfaces for complete control of phase and polarization with subwavelength spatial resolution and high transmission. *Nat Nanotechnol* (2015) 10(11):937–43. doi:10.1038/nnano.2015.186

62. Shaltout AM, Kinsey N, Kim J, Chandrasekar R, Ndukaife JC, Boltasseva A, et al. Development of optical metasurfaces: emerging concepts and new materials. *Proc IEEE* (2016) 104(12):2270–87. doi:10.1109/JPROC.2016.2590882

63. Akselrod GM, Huang J, Hoang TB, Bowen PT, Su L, Smith DR, et al. Large-area metasurface perfect absorbers from visible to near-infrared. *Adv Mater Weinheim* (2015) 27(48):8028–34. doi:10.1002/adma.201503281

64. Horie Y, Arbabi A, Arbabi E, Kamali SM, Faraon A. Wide bandwidth and high resolution planar filter array based on DBR-metasurface-DBR structures. *Optic Exp* 24 (2016) 11677–82. doi:10.1364/OE.24.011677

65. Sun H, Wen G, Huang Y, Li J, Zhu W, Si LM. Tunable band notch filters by manipulating couplings of split ring resonators. *Appl Optic* (2013) 52(31):7517–22. doi:10.1364/AO.52.007517

66. Li Z, Wang W, Rosenmann D, Czaplewski DA, Yang X, Gao J. All-metal structural color printing based on aluminum plasmonic metasurfaces. *Optic Exp* (2016) 24(18):20472. doi:10.1364/OE.24.020472

67. Kim TT, Kim H, Kenney M, Park HS, Kim HD, Min B, et al. Amplitude modulation of anomalously refracted terahertz waves with gated-graphene

metasurfaces. *Adv Opt Mater* (2018) 6(1):201700507. doi:10.1002/adom. 201700507

68. Song X, Huang L, Tang C, Li J, Li X, Liu J, et al. Selective diffraction with complex amplitude modulation by dielectric metasurfaces. *Adv Opt Mater* (2018) 6(4):1701181. doi:10.1002/adom.201701181

69. Song X, Huang L, Sun L, Zhang X, Zhao R, Li X, et al. Near-field plasmonic beam engineering with complex amplitude modulation based on metasurface. *Appl Phys Lett* (2018) 112:73104. doi:10.1063/1.5013327

70. Yu N, Genevet P, Kats MA, Aieta F, Tetienne JP, Capasso F, et al. Light propagation with phase discontinuities: generalized laws of reflection and refraction. *Science* (2011) 334(6054):333–7. doi:10.1126/science.1210713

71. Aieta F, Genevet P, Kats MA, Yu N, Blanchard R, Gaburro Z, et al. Aberration-free ultrathin flat lenses and axicons at telecom wavelengths based on plasmonic metasurfaces. *Nano Lett* (2012) 12(9):4932–6. doi:10.1021/nl302516v

72. Zhang L, Mei S, Huang K, Qiu CW. Advances in full control of electromagnetic waves with metasurfaces. *Adv Opt Mater* (2016) 4(6):818–33. doi:10.1002/adom.201500690

73. Ding X, Monticone F, Zhang K, Zhang L, Gao D, Burokur SN, et al. Ultrathin pancharatnam-berry metasurface with maximal cross-polarization efficiency. *Adv Mater Weinheim* (2015) 27(7):1195–200. doi:10.1002/adma.201405047

74. Wen D, Yue F, Li G, Zheng G, Chan K, Chen S, et al. Helicity multiplexed broadband metasurface holograms. *Nat Commun*, 6 (2015)(6) 8241–7. doi:10.1038/ncomms9241

75. Maguid E, Chriki R, Yannai M, Kleiner V, Hasman E, Friesem AA, et al. Topologically controlled intracavity laser modes based on pancharatnam-berry phase. *ACS Photon* (2018) 5(5):1817–21. doi:10.1021/acsphotonics.7b01525

76. Luo W, Sun S, Xu HX, He Q, Zhou L. Transmissive ultrathin pancharatnam-berry metasurfaces with nearly 100% efficiency. *Phys Rev Appl* (2017) 7(4):44033. doi:10.1103/PhysRevApplied.7.044033

77. Li J, Yao J. Manipulation of terahertz wave using coding pancharatnam-berry phase metasurface. *IEEE Photonics J* (2018) 10:5900512. doi:10.1109/JPHOT.2018.2866490

78. Zheng G, Mühlenbernd H, Kenney M, Li G, Zentgraf T, Zhang S. Metasurface holograms reaching 80% efficiency. *Nat Nanotechnol* (2015) 10(4):308–12. doi:10.1038/nnano.2015.2

79. Pfeiffer C, Grbic A. Metamaterial Huygens' surfaces: tailoring wave fronts with reflectionless sheets. *Phys Rev Lett* (2013) 110(19):197401–5. doi:10.1103/PhysRevLett.110.197401

80. Pfeiffer C, Boltasseva A. Efficient light bending with isotropic metamaterial Huygens' surfaces. *Nano Lett* (2014) 14:2491–7. doi:10.1021/nl5001746

81. Wang L, Kruk S, Tang H, Li T, Kravchenko I, Neshev DN, et al. Grayscale transparent metasurface holograms. *Optica* (2016) 3(12):1504. doi:10.1364/OPTICA.3.001504

82. Wang Z, Ding X, Zhang K, Ratni B, Burokur SN, Gu X, et al. Huygens metasurface holograms with the modulation of focal energy distribution. *Adv Opt Mater* (2018) 6:1800121. doi:10.1002/adom.201800121

83. Qin F, Ding L, Zhang L, Monticone F, Chum CC, Deng J, et al. Hybrid bilayer plasmonic metasurface efficiently manipulates visible light. *Sci Adv* (2016) 2: e1501168. doi:10.1126/sciadv.1501168

84. Arbabi A, Arbabi E, Horie Y, Kamali SM, Faraon A. Planar metasurface retroreflector. *Nat Photon* (2017) 11(7):415–20. doi:10.1038/nphoton.2017.96

85. Wu C, Arju N, Kelp G, Fan J, Dominguez J, Gonzales E, et al. Spectrally selective chiral silicon metasurfaces based on infrared Fano resonances. *Nat Commun* (2014) 5:3892. doi:10.1038/ncomms4892

86. Pfeiffer C, Zhang C, Ray V, Guo LJ, Grbic A. High performance bianisotropic metasurfaces: asymmetric transmission of light. *Phys Rev Lett* (2014) 113(2):023902–5. doi:10.1103/PhysRevLett.113.023902

87. Pfeiffer C, Zhang C, Ray V, Guo LJ, Grbic A. Polarization rotation with ultra-thin bianisotropic metasurfaces. *Optica* (2016) 3(4):427–32. doi:10.1364/OPTICA.3.000427

88. Balthasar Mueller JP, Rubin NA, Devlin RC, Groever B, Capasso F. Metasurface polarization optics: independent phase control of arbitrary orthogonal states of polarization. *Phys Rev Lett* (2017) 118(11):113901–5. doi:10.1103/PhysRevLett.118.113901

89. Huang X, Chen J, Yang H. High-efficiency wideband reflection polarization conversion metasurface for circularly polarized waves. *J Appl Phys* (2017) 122(4):043102. doi:10.1063/1.4996643

90. Yang W, Meng Q, Che W, Gu L, Xue Q. Low-profile wideband dual-circularly polarized metasurface antenna array with large beamwidth. *IEEE Antenn Wireless Propag Lett* (2018) 17(9):1613–6. doi:10.1109/LAWP.2018.2857625

91. Liu L, Zhang X, Kenney M, Su X, Xu N, Ouyang C, et al. Broadband metasurfaces with simultaneous control of phase and amplitude. *Adv Mater Weinheim* (2014) 26(29):5031–6. doi:10.1002/adma.201401484

92. Li Z, Cheng H, Liu Z, Chen S, Tian J. Plasmonic airy beam generation by both phase and amplitude modulation with metasurfaces. *Adv Opt Mater* (2016) 4(8):1230–5. doi:10.1002/adom.201600108

93. Song EY, Lee GY, Park H, Lee K, Kim J, Hong J, et al. Compact generation of airy beams with C-aperture metasurface. *Adv Opt Mater* (2017) 5(10):1601028. doi:10.1002/adom.201601028

94. Lee GY, Yoon G, Lee SY, Yun H, Cho J, Lee K, et al. Complete amplitude and phase control of light using broadband holographic metasurfaces. *Nanoscale* (2018) 10(9):4237–45. doi:10.1039/c7nr07154j

95. Li J, Chen S, Yang H, Li J, Yu P, Cheng H, et al. simultaneous control of light polarization and phase distributions using plasmonic metasurfaces. *Adv Func Mater* (2015) 25(5):704–10. doi:10.1002/adfm.201403669

96. Zhou Y, Cao X, Gao J, Yang H, Li S. Reconfigurable metasurface for multiple functions: magnitude, polarization and phase modulation. *Optic Express* (2018) 26(22):29451–9. doi:10.1364/OE.26.029451

97. Xu HX, Hu G, Lei H, Jiang M, Huang Y, Li Y, et al. Chirality-Assisted high-efficiency metasurfaces with independent control of phase, amplitude, and polarization. *Adv Opt Mater* (2018) 7:1801479. doi:10.1002/adom.201801479

98. Shaltout AM, Kildishev AV, Shalaev VM. Evolution of photonic metasurfaces: from static to dynamic. *J Opt Soc Am B* (2016) 33(3):501. doi:10.1364/JOSAB.33.000501

99. Liu S, Cui TJ. Concepts, working principles, and applications of coding and programmable metamaterials. *Adv Opt Mater* (2017) 5(22):1700624. doi:10.1002/adom.201700624

100. Krasnok A, Tymchenko M, Alù A. Nonlinear metasurfaces: a paradigm shift in nonlinear optics. *Mater Today* (2018) 21(1):8–21. doi:10.1016/j.mattod.2017.06.007

101. Kafaie Shirmanesh G, Sokhoyan R, Pala RA, Atwater HA. Dual-gated active metasurface at 1550 nm with wide (>300°) phase tunability. *Nano Lett* (2018) 18(5):2957–63. doi:10.1021/acs.nanolett.8b00351

102. Nemati A, Wang Q, Hong M, Teng J. Tunable and reconfigurable metasurfaces and metadevices. *Opto-Electronic Adv* (2018) 1(5): 18000901–25. doi:10.29026/oea.2018.180009

103. Liu F, Pitilakis A, Mirmoosa MS, Tsilipakos O, Wang X, Tasolamprou AC, et al. Programmable metasurfaces: state of the art and prospects. In: 2018 IEEE International Symposium on Circuits and Systems (ISCAS); 2018 May 27–30; Florence, Italy. New York, NY: IEEE (2018). p. 1–5.

104. Chen K, Feng Y, Monticone F, Zhao J, Zhu B, Jiang T, et al. A reconfigurable active Huygens' metalens (2017). Available at: https://arxiv.org/abs/1702.01920.

105. Li A, Kim S, Luo Y, Li Y, Long J, Sievenpiper DF. High-power transistor-based tunable and switchable metasurface absorber. *IEEE Trans Microw Theor Tech* (2017) 65(8):2810–8. doi:10.1109/TMTT.2017.2681650

106. Zhao X, Schalch J, Zhang J, Seren H, Duan G, Averitt R, et al. Electromechanically tunable metasurface transmission waveplate at terahertz frequencies. *Optica* (2018) 5:303–10. doi:10.1364/OPTICA.5.000303

107. Arbabi E, Arbabi A, Kamali SM, Horie Y, Faraji-Dana M, Faraon A. MEMS-tunable dielectric metasurface lens. *Nat Commun* (2018) 9, 812. doi:10.1038/s41467-018-03155-6

108. Manjappa M, Pitchappa P, Singh N, Wang N, Zheludev NI, Lee C, et al. Reconfigurable MEMS Fano metasurfaces with multiple-input-output states for logic operations at terahertz frequencies. *Nat Commun* (2018) 9(1):4056–10. doi:10.1038/s41467-018-06360-5

109. Biswas SR, Gutiérrez CE, Nemilentsau A, Lee IH, Oh SH, Avouris P, et al. Tunable graphene metasurface reflectarray for cloaking, illusion, and focusing. *Phys Rev Appl* (2018) 9(3):34021. doi:10.1103/PhysRevApplied.9.034021

110. Komar A, Fang Z, Bohn J, Sautter J, Decker M, Miroshnichenko A, et al. Electrically tunable all-dielectric optical metasurfaces based on liquid crystals. *Appl Phys Lett* (2017) 110(7):071109. doi:10.1063/1.4976504

111. Xiao D, Liu YJ, Yin S, Liu J, Ji W, Wang B, et al. Liquid-crystal-loaded chiral metasurfaces for reconfigurable multiband spin-selective light absorption. *Optic Express* (2018) 26(19):25305–14. doi:10.1364/OE.26.025305

112. Yurduseven O, Marks D, Fromenteze T, Smith D. Dynamically reconfigurable holographic metasurface aperture for a mills-cross monochromatic microwave camera. *Optic Express* (2018) 26:5281–91. doi:10.1364/OE.26.005281

113. Gao X, Yang WL, Ma HF, Cheng Q, Yu XH, Cui TJ, et al. A reconfigurable broadband polarization converter based on an active metasurface. *IEEE Trans Antenn Propag* (2018) 66:6086–95. doi:10.1109/TAP.2018.2866636

114. Chen L, Ma HL, Ruan Y, Cui HY. Dual-manipulation on wave-front based on reconfigurable water-based metasurface integrated with PIN diodes. *J Appl Phys* (2019) 125(2):23107. doi:10.1063/1.5078660

115. Zhang J, Wei X, Rukhlenko ID, Chen HT, Zhu W. Electrically tunable metasurface with independent frequency and amplitude modulations. *ACS Photon* (2019) 7(1):265–71. doi:10.1021/acsphotonics.9b01532

116. Han S, Kim S, Kim S, Low T, Brar VW, Jang MS. Complete complex amplitude modulation with electronically tunable graphene plasmonic metamolecules. *ACS Nano* (2020) 14(1):1166–75. doi:10.1021/acsnano.9b09277

117. Chen D, Yang J, Huang J, Bai W, Zhang J, Zhang Z, et al. The novel graphene metasurfaces based on split-ring resonators for tunable polarization switching and beam steering at terahertz frequencies. *Carbon* (2019) 154:350–6. doi:10.1016/j.carbon.2019.08.020

118. Quader S, Zhang J, Akram MR, Zhu W. Graphene-based high-efficiency broadband tunable linear-to-circular polarization converter for terahertz waves. *IEEE J Sel Top Quant Electron* (2020) 26(5):1–8. doi:10.1109/JSTQE.2020.2969566

119. Zhang J, Wei X, Premaratne M, Zhu W. Experimental demonstration of an electrically tunable broadband coherent perfect absorber based on a graphene–electrolyte–graphene sandwich structure. *Photon Res* (2019) 7(8):868–74. doi:10.1364/PRJ.7.000868

120. Chen X, Tian Z, Lu Y, Xu Y, Zhang X, Ouyang C, et al. Electrically tunable perfect terahertz absorber based on a graphene salisbury screen hybrid metasurface. *Advan Optical Mater* (2020) 8(3):1900660. doi:10.1002/adom.201900660

121. Islam MS, Sultana J, Biabanifard M, Vafapour Z, Nine MJ, Dinovitser A, et al. Tunable localized surface plasmon graphene metasurface for multiband superabsorption and terahertz sensing. *Carbon* (2020) 158:559–67. doi:10.1016/j.carbon.2019.11.026

122. Yuan Y, Sun S, Chen Y, Zhang K, Ding X, Ratni B, et al. A fully phase-modulated metasurface as an energy-controllable circular polarization router. *Adv Sci* (2020) 7(18):2001437. doi:10.1002/advs.202001437

123. Chen H, Lu WB, Liu ZG, Geng MY (2020). Microwave programmable graphene metasurface. *ACS Photonics*. 7, 1425–35. doi:10.1021/acsphotonics.9b01807

124. Hosseininejad SE, Rouhi K, Neshat M, Faraji-Dana R, Cabellos-Aparicio A, Abadal S, et al. Reprogrammable graphene-based metasurface mirror with adaptive focal point for THz imaging. *Sci Rep* (2019) 9(1):2868–9. doi:10.1038/s41598-019-39266-3

125. Howes A, Wang W, Kravchenko I, Valentine J (2018). Dynamic transmission control based on all-dielectric Huygens metasurfaces. *Optica* 5(7):787–92. doi:10.1364/OPTICA.5.000787

126. Tsilipakos O, Tasolamprou A, Koschny T, Kafesaki M, Economou E, Soukoulis C. Pairing toroidal and magnetic dipole resonances in elliptic dielectric rod metasurfaces for reconfigurable wavefront manipulation in reflection. *Adv Opt Mater* (2018) 6:1800633. doi:10.1002/adom.201800633

127. Zhang L, Chen XQ, Liu S, Zhang Q, Zhao J, Dai JY, et al. Space-time-coding digital metasurfaces. *Nat Commun* (2018) 9:4334. doi:10.1038/s41467-018-06802-0

128. Li L, Jun Cui T, Ji W, Liu S, Ding J, Wan X, et al. Electromagnetic reprogrammable coding-metasurface holograms. *Nat Commun* (2017) 8, 197. doi:10.1038/s41467-017-00164-9

129. Li L, Shuang Y, Ma Q, Li H, Zhao H, Wei M, et al. Intelligent metasurface imager and recognizer. *Light Sci Appl* (2019) 8(1):97. doi:10.1038/s41377-019-0209-z

130. Ma Q, Bai GD, Jing HB, Yang C, Li L, Cui TJ. Smart metasurface with self-adaptively reprogrammable functions. *Light Sci Appl* (2019) 8(1):98. doi:10.1038/s41377-019-0205-3

131. Wang Q, Rogers ETF, Gholipour B, Wang CM, Yuan G, Teng J, et al. Optically reconfigurable metasurfaces and photonic devices based on phase change materials. *Nat Photon* (2016) 10(1):60–5. doi:10.1038/nphoton.2015.247

132. Cong L, Srivastava YK, Zhang H, Zhang X, Han J, Singh R. All-optical active THz metasurfaces for ultrafast polarization switching and dynamic beam splitting. *Light Sci Appl* (2018) 7(1):28. doi:10.1038/s41377-018-0024-y

133. Cai H, Huang Q, Hu X, Liu Y, Fu Z, Zhao Y, et al. All-optical and ultrafast tuning of terahertz plasmonic metasurfaces. *Adv Opt Mater* (2018) 6:1800143. doi:10.1002/adom.201800143

134. Fan K, Zhang J, Liu X, Zhang GF, Averitt RD, Padilla WJ. Phototunable dielectric Huygens' metasurfaces. *Adv Mater* (2018) 30(22):1800278. doi:10.1002/adma.201800278

135. Zhang XG, Tang WX, Jiang WX, Bai GD, Tang J, Bai L, et al. Light-controllable digital coding metasurfaces. *Adv Sci* (2018) 5(11):1801028. doi:10.1002/advs.201801028

136. Rahmani M, Xu L, Miroshnichenko AE, Komar A, Camacho-Morales R, Chen H, et al. Reversible thermal tuning of all-dielectric metasurfaces. *Adv Funct Mater* (2017) 27(31):1700580. doi:10.1002/adfm.201700580

137. Komar A, Paniagua-Domínguez R, Miroshnichenko A, Yu YF, Kivshar YS, Kuznetsov AI, et al. Dynamic beam switching by liquid crystal tunable dielectric metasurfaces. *ACS Photon* (2018) 5(5):1742–8. doi:10.1021/acsphotonics.7b01343

138. Dong W, Qiu Y, Zhou X, Banas A, Banas K, Breese M, et al. Tunable mid-infrared phase-change metasurface. *Adv Opt Mater* (2017) 6:201701346. doi:10.1002/adom.201701346

139. Cai H, Chen S, Zou C, Huang Q, Liu Y, Hu X, et al. Multifunctional hybrid metasurfaces for dynamic tuning of terahertz waves. *Adv Opt Mater* (2018) 6(14):1800257. doi:10.1002/adom.201800257

140. Tian J, Li Q, Lu J, Qiu M. Reconfigurable all-dielectric antenna-based metasurface driven by multipolar resonances. *Optic Express* (2018) 26(18):23918–25. doi:10.1364/OE.26.023918

141. Chen X, Gao J, Kang B. Achieving a tunable metasurface based on a structurally reconfigurable array using SMA. *Optic Express* (2018) 26(4):4300–8. doi:10.1364/OE.26.004300

142. Reeves JB, Jayne RK, Stark TJ, Barrett LK, White AE, Bishop DJ. Tunable infrared metasurface on a soft polymer scaffold. *Nano Lett* (2018) 18(5):2802–6. doi:10.1021/acs.nanolett.7b05042

143. Liu X, Huang Z, Zhu C, Wang L, Zang J. Out-of-Plane designed soft metasurface for tunable surface plasmon polariton. *Nano Lett* (2018) 18(2):1435–41. doi:10.1021/acs.nanolett.7b05190

144. Wang Z, Jing L, Yao K, Yang Y, Zheng B, Soukoulis CM, et al. Origami-based reconfigurable metamaterials for tunable chirality. *Adv Mater* (2017) 29(27):1–7. doi:10.1002/adma.201700412

145. Chen L, Ma HL, Cui HY. Wavefront manipulation based on mechanically reconfigurable coding metasurface. *J Appl Phys* (2018) 124(4):43101. doi:10.1063/1.5039679

146. Lee J, Tymchenko M, Argyropoulos C, Chen PY, Lu F, Demmerle F, et al. Giant nonlinear response from plasmonic metasurfaces coupled to intersubband transitions. *Nature* (2014) 511(7507):65–9. doi:10.1038/nature13455

147. Nicholls LH, Rodríguez-Fortuño FJ, Nasir ME, Córdova-Castro RM, Olivier N, Wurtz GA, et al. Ultrafast synthesis and switching of light polarization in nonlinear anisotropic metamaterials. *Nat Photon* (2017) 11(10):628–33. doi:10.1038/s41566-017-0002-6

148. Xu Y, Sun J, Frantz J, Shalaev MI, Walasik W, Pandey A, et al. Reconfiguring structured light beams using nonlinear metasurfaces. *Optic Express* (2018) 26(23):30930–43. doi:10.1364/OE.26.030930

149. Zhu H, Yi F, Cubukcu E. Plasmonic metamaterial absorber for broadband manipulation of mechanical resonances. *Nat Photon* (2016) 10(11):709–14. doi:10.1038/nphoton.2016.183

150. Ou JY, Plum E, Zhang J, Zheludev NI. Giant nonlinearity of an optically reconfigurable plasmonic metamaterial. *Adv Mater Weinheim* (2016) 28(4):729–33. doi:10.1002/adma.201504467

151. Zanotto S, Tredicucci A, Navarro-Urrios D, Cecchini M, Biasiol G, Mencarelli D, et al. Optomechanics of chiral dielectric metasurfaces. *Adv Opt Mater* (2019) 8(4):1901507. doi:10.1002/adom.201901507

152. Zhang M, Ma X, Pu M, Liu K, Guo Y, Huang Y, et al. Large-area and low-cost nanoslit-based flexible metasurfaces for multispectral electromagnetic wave manipulation. *Adv Optical Mater* (2019) 7(23):1900657. doi:10.1002/adom.201900657

153. Long Z, Liang Y, Feng L, Zhang H, Liu M, Xu T. Low-cost and high sensitivity glucose sandwich detection using a plasmonic nanodisk metasurface. *Nanoscale* (2020) 12(19):10809–15. doi:10.1039/d0nr00288g

154. Tang W, Chen MZ, Dai JY, Zeng Y, Zhao X, Jin S, et al. Wireless communications with programmable metasurface: new paradigms, opportunities, and challenges on transceiver design. *IEEE Wireless Commun* (2020) 27(2):180–7. doi:10.1109/MWC.001.1900308

155. Li L, Ruan H, Liu C, Li Y, Shuang Y, Alù A, et al. Machine-learning reprogrammable metasurface imager. *Nat Commun* (2019) 10(1):1082–8. doi:10.1038/s41467-019-09103-2

156. Qian C, Zheng B, Shen Y, Li J, Li E, Shen H, et al. Deep-learning-enabled self-adaptive microwave cloak without human intervention. *Nat Photon* (2020) 14(6):383–90. doi:10.1038/s41566-020-0604-2

157. Qian C, Lin X, Lin X, Xu J, Sun Y, Li E, et al. Performing optical logic operations by a diffractive neural network. *Light Sci Appl* (2020) 9(1):59. doi:10.1038/s41377-020-0303-2

Theoretical Investigation of the Passive Transmitter Based on Reconfigurable Metasurface

Shuai Yang, Kuang Zhang, Xumin Ding, Guohui Yang and Qun Wu *

Department of Microwave Engineering, Harbin Institute of Technology, Harbin, China

Wireless communication has become a standard solution to satisfy the ever-increasing demands of information transfer in our daily life. Furthermore, reconfigurable metasurfaces comprised of multiple tunable unitcells have drawn significant attention due to their superior electromagnetic performance, while the desired electromagnetic response can be controlled by computer. We therefore present a prototype of a wireless communication system based reconfigurable metasurface that works in the microwave frequency range. A 2-D periodical array of a reconfigurable metasurface is loaded with a varactor diode to effectively adjust the in-band transmission and reflection coefficients that maintain different far-field electromagnetic characteristics. The reconfigurable metasurface does not radiate electromagnetic waves and only carries information by adjusting its reflection and transmission coefficients. With this reconfigurable metasurface, a passive communication method can be realized.

Keywords: reconfigurable metasurface, wireless communication, reconfigurable transmission surface, active frequency selective surface, software defined radio

1 INTRODUCTION

It is foreseen that the commercial service of the fifth-generation (5G) of mobile communications will be launched on a worldwide scale starting in 2020. The application of the Internet of Things as an important part of the fifth-generation of mobile communication has a very broad development prospect [1]. At present, wireless sensors in IoT devices are facing two major problems: power consumption and transmission distance [2]. The server's increasing demands are driven by various intelligent devices, such as smart meters, telemedicine, virtual reality, and autonomous driving, all of which include a lot of wireless sensor devices. With the growth of these mobile Internet services, the requirements for sensor power consumption have become increasingly higher. Currently, short-range wireless communication methods mainly include near-field communication (NFC), Bluetooth, and Zigbee, and most of these methods mainly work with frequency types such as S-band. A metasurface, composed of sub-wave-length resonators in 2-D plane [3–6], can provide a new way to control electromagnetics (EM) in terms of propagation modes, polarization, and wave-fonts [7–12], and recently an active anisotropic metasurface whose reflection phases can be electrically and independently tuned for two orthogonal polarized waves was reported [13]. Due to their unique EM properties, we propose a passive transmitter, using a reconfigurable metasurface design work in 2.4 GHz, to reduce the transmitter's power consumption and to make the metasurface compatible with the standard IEEE 802.11ac. IEEE 802.11ac is a wireless networking standard in the 802.11 set of protocols (which is part of the Wi-Fi networking family), providing high-throughput wireless local area networks (WLAN) on the 2.4 GHz and 5 GHz band.
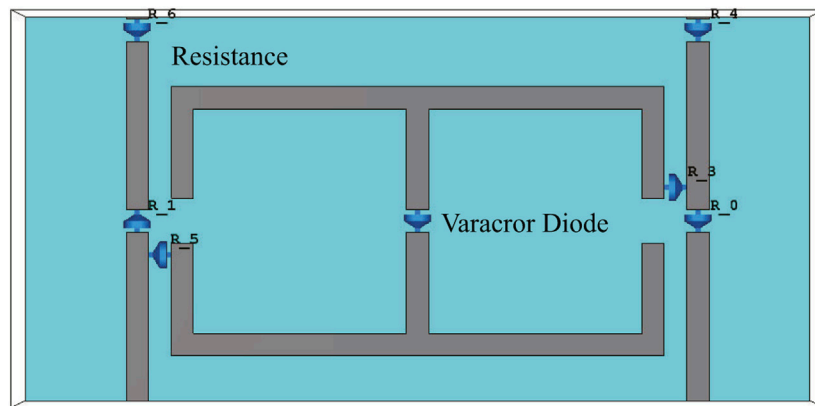
FIGURE 1 | The tunable unit of reconfigurable metasurface.

In this paper, a single layer reconfigurable metasurface has been presented with the aim of reducing power consumption. The proposed geometry consists of periodic metallic Patterns imprinted on the top of the dielectric substrate, where varactor diodes are mounted in the center of each unit cell. The reconfigurable metasurface has been constructed such that it can integrate two different characteristics (single band reflection and transmission) with independent control of the biasing states of the varactor diodes. In order to communicate with the passive transmitter a receiver has been designed with a software-defined radio (SDR) [14–18]. A software-defined radio is a radio communication system where components that have been traditionally implemented in hardware are instead implemented by means of software on a personal computer or an embedded system. While the concept of SDR is not new, the receiver in this paper only provided a method to verify this design. The varactors in the reconfigurable metasurface are controlled by the base band signal.

The remainder of this paper is organized as follows. **Section 2** presents the proposed design concept for a passive transmitter, then describes the system composition and characteristics of power consumption. **Section 3** discusses the theoretical investigation of this design and show the simulation results. Finally, concluding remarks and a comparison of the proposed passive transmitter to the traditional short-range wireless communication methods are presented in the last section.

2 RECONFIGURABLE METASURFACE PASSIVE TRANSMITTER

2.1 The Design of Unitcell

The reconfigurable metasurface is a lattice of 2-D subwave-length meta-atoms loaded with varactor diodes [14–23]. The Schematic view of the unitcell is illustrated in **Figure 1**. It includes one metallic layer that is placed on one substrate (F4B with a dielectric constant of 2.65 and loss tangent of 0.001). On the top layer is a "E" shape metallic strip combined by a varactor diode surrounded by metallic strips. The Structural parameters are chosen as

follows: The width of the unitcell $W = 35 mm$, the height of the unitcell $H = 17\,mm$, the strip width $l = 1\,mm$, the width of 'E' strip $X = 18\,mm$, the height of "E" shape strip $Y_1 = 5.5\,mm$, and the gap of the varactor diode $g = 1\,mm$, in other words, the total height of the central patch $Y_2 = 12\,mm$ and the thickness of the substrate $t = 0.8mm$. The varactor diode is placed across the gap on the top layer, and six resistors with a resistance of 10 K ohms are placed symmetrically, as shown in **Figure 1**, to limit the bias current and to isolate the surface current. By tuning the reverse DC bias voltage across the varactor V_b, the reflection coefficient of the reconfigurable metasurface is manipulated. In this work we select the varactor diode infineon BB857, whose services resistance $R_s = 1.5\,\Omega$, inductance $L_s = 0.7\,nH$, and capacitance C ranges from 0.54 to 6.6 pF when its reverse biasing voltage changes from 28 to 0 V. In this unitcell we know that the gap of the "E" shape strips the metallic wires on the top layer combined by a varactor, so that the varactor is a parallel connection. The transmitter properties of the unitcell is a function of the biasing voltage V_b. The resonance moves from low to high frequencies when V_b decreases from 28 to 0 V.

2.2 System Model

A Full structure sample containing 5×9 unitcells are placed on the EM absorbing material, as shown in **Figure 2**. Then we change the resonance frequencies, the metasurface can work as an absorber and reflector. The receiver in this system will continuously radiate horizontally polarized EM waves. In this paper, a software-defined radio is used to implement a continuous wave radar working at 2.4 GHz as a signal receiver, which is illustrated in **Figure 3**.

In this passive transmitter radio frequency (RF) source and amplifier is not employed, so the transmission coefficient is obtained as

$$\Gamma = S_{21} - S_{21air} \tag{1}$$

where S_{21} is the transmission coefficient through the reconfigurable metasurface and S_{21air} is the coefficient when the EM waves through the air.
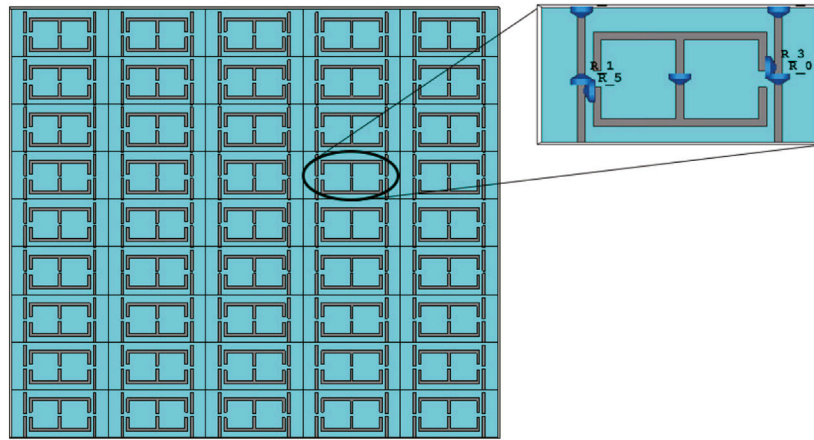
FIGURE 2 | Schematic of the reconfigurable metasurface with a periodic structure.
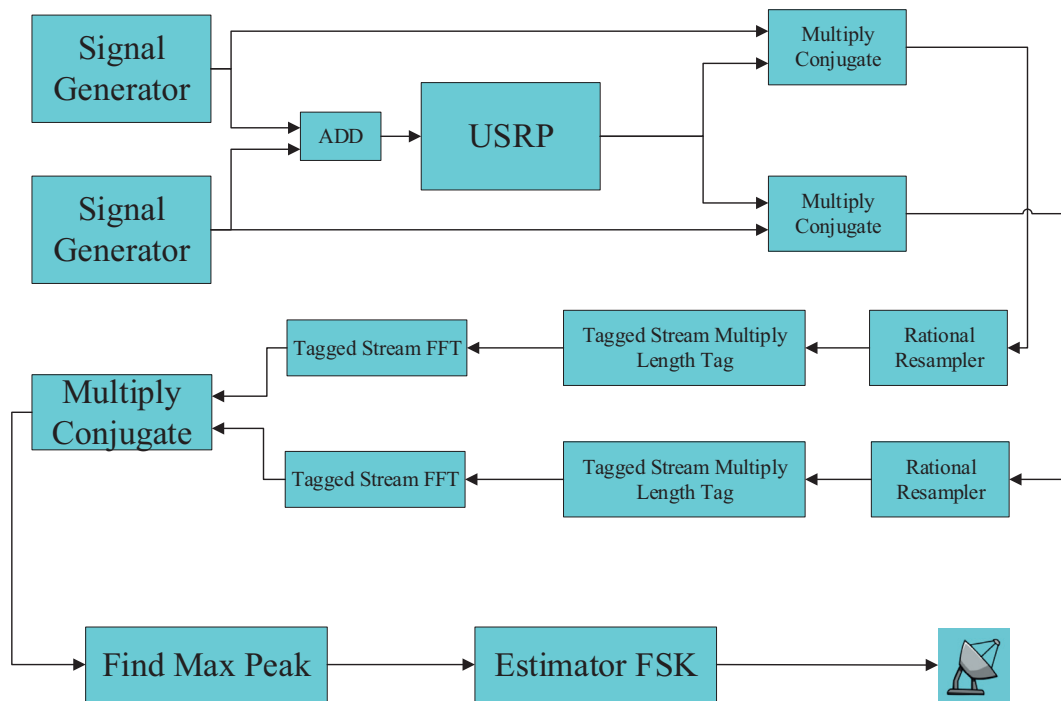

FIGURE 3 | The block diagram of the receiver based on the software defined radio.

For simplicity, let us assume that a wireless source emits a seemingly random signal $s(t)$, and the received sequence of binary digital information is $r(\tau)$, we refer to the time τ in $r(\tau)$. In an analogy with continuous-wave radar $s(t)$ and $g(\tau)$ can be correspondingly regarded as the launch wave and radar echo. We need to convert the $g(\tau)$ into that of the distinguishable carry wave control coding patterns of the reconfigurable metasurface $\Gamma(\tau)$. At any given time τ_0, if $\Gamma(\tau_0) = \Gamma_0$, the stray received sequence $g(\tau_0) = s(t) \times \Gamma_0$. So, the received sequence with the information modulated by coding patterns.

When the metasurface is driven by the EM wave E_i, normally incident from the top toward the metasurface at f_i, the response can be represented as

$$E_r = \Gamma \times E_i = \Gamma \times e^{j2\pi f_i t} \quad (2)$$

where E_r stands for the reflected wave. From the theory of Fourier transform, the frequency response can be expressed as

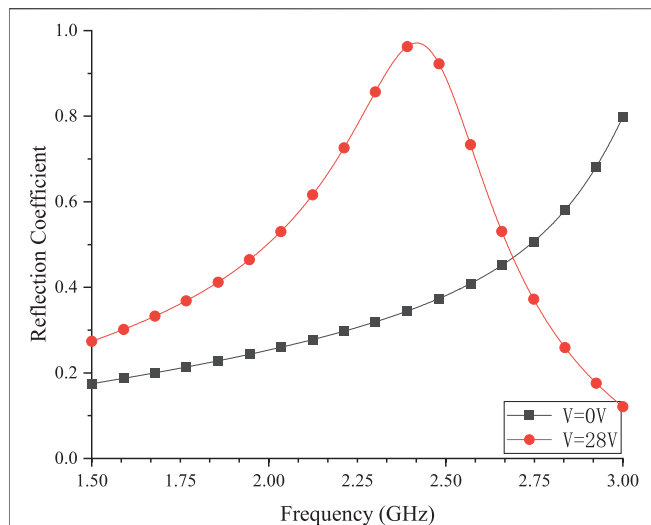$$E_r(f) = \Gamma(f) * [\delta(f - f_i)] = \Gamma(f - f_i) \quad (3)$$

FIGURE 4 | The reflection coefficient of a reconfigurable metasurface at different voltages.
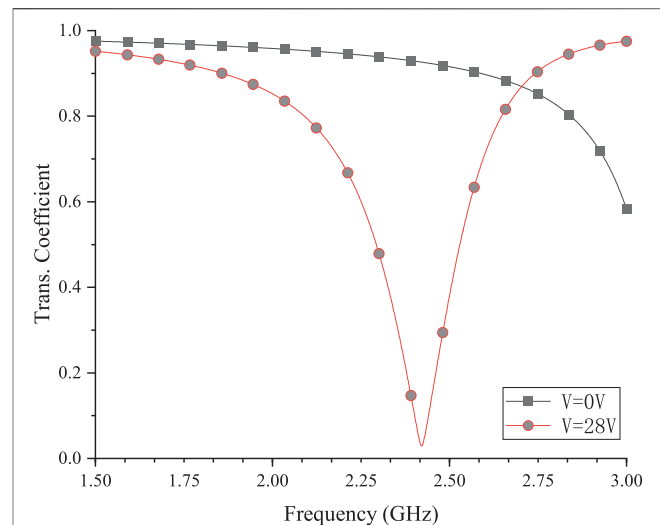

FIGURE 5 | The transmission coefficient of a reconfigurable metasurface at different voltages.

where $*$ stands for the convolution operation, and δ is the Dirac delta function, respectively. We know that the reflection responses are highly dependent on the transmission coefficient's frequency response from **Eq. 2**.

In this work, the varactor diodes are working at two states, one is without biasing voltage ($V = 0V, C = 6.6pF$) and the other is with biasing voltage ($V = 28V, C = 0.54pF$). In this case we can realize a 1-bit digital codes, the reflector state is defined as the code "1" and the transmission state is defined as the code "0". So, a Frequency-shift keying (FSK) transmitter can be realized based on this reconfigurable metasurface.

3 SIMULATIONS AND DISCUSSION

To verify the performance of the proposed metasurface, Frequency domain simulations are performed using the CST studio and GNUradio software. In our Simulations, the unitcells are driven by the horizontal polarized wave from 1.5 GHz to 3 GHz. The reflection and transmission coefficient are shown in **Figure 4** and **Figure 5**. As an illustrative example, we find that the reconfigurable metasurface worked at 2.4 GHz by adjusting the biasing voltage, and the EM resonance changes as expected.

Furthermore, we simulated the reconfigurable metasurface's farfield properties. From the farfield simulation results, it can be intuitively seen that the main lobe of the reconfigurable metasurface covers half of the space and the amplitude of the backward radiation is very low. In this case, its farfield reflection properties can be well modulated.

Particularly, the reflectivity and phase difference of the two elements under the illumination of forward x-polarized incidence are depicted in **Figure 6**, respectively. It is clearly shown that the complete reflection with direction difference

approximately approaching 180°, is well kept in 2.4 GHz. The transmitter is composed of 9×5 unitcells. Since the varactor diodes works at 0v and 28 V reverses the bias state, its reverse current is about 10 nA, the power consumption of a single structural unit is about 300 nW, and its total power consumption is less than 1 mW. The power consumption comparison of communication is shown in **Table 1**.

Based on the design proposed above, we can combine it into a new communication system. The reconfigurable metasurface whose biasing voltage are controlled by the base band signal plays the role of transmitter. The continuous wave radar designed by GNUradio is used as a receiver. In this communication system the transmitter does not radiate any EM wave, which is of great significance for EM silence. In IoT applications, a large part of the sensor data transmission is unidirectional, and the power is limited. The passive trans proposed in this paper may solve these problems.

4 CONCLUSION

In summary, we provided a theoretical framework for modulation, and simulated a prototype system tailored to the use of ambient commodity 2.4 GHz Wi-Fi signals. The proposed design is comprised of switchable active comments mounted across the metallic grids, and with base band control of the biasing conditions of the varactor diodes, the metasurface realized different modes of operation. For different biasing voltages the reconfigurable metasurface showed different electromagnetic characteristics, and then used these characteristics to achieve information transmission and reduced the power consumption of this kind of transmitter. At present, traditional short-range communication methods such as Bluetooth consume more
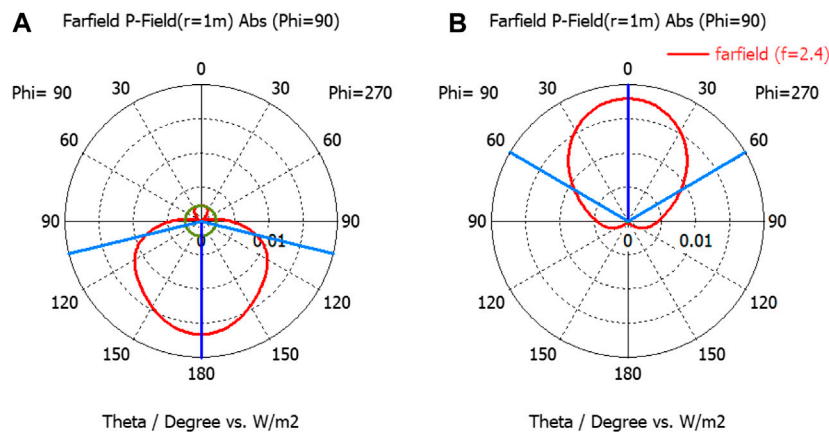
FIGURE 6 | Simulation results of the reconfigurable metasurface's far-field radiation properties. **(A)** V = 0 V the metasurface working as a reflector. **(B)** V = 28 V the metasurface working in the transmission state, which can be regarded as an absorber due to the combination with the absorber placed behind the metasurface.

TABLE 1 | Comparison of wireless technologies' power consumption.

Wireless technologies	Power consumption	Communication distance
ZigBee	100 mW	100 m
Wi-Fi	>100 mW	1000 m
Bluetooth	10 mW	10 m
Passive transmitter	<1 mW	Depends on the receiver's resolution

than 10 mW. The passive transmitter based on a reconfigurable metasurface proposed in this article works in the reverse bias state of the varactor. The power consumption is therefore less than 1 mW and the distance of communication depends on the receiver's resolution. It will also have applicational prospects in confidential communications. We believe that our passive transmitter, based on a reconfigurable metasurface, provides a fundamentally new view on wireless communication systems that can impact a wide range of future passive and IoT communication systems at radiofrequencies.

REFERENCES

1. Liu F, Tsilipakos O, Pitilakis A, Tasolamprou AC, Mirmoosa MS, Kantartzis NV, et al. Intelligent metasurfaces with continuously tunable local surface impedance for multiple reconfigurable functions. *Phys Review Appl* (2019) 11:044024. doi:10.1103/physrevapplied.11.044024

2. Liu H, Sarrazin J, Deshours F, Mavridis T, Petrillo L, Liu Z, et al. Performance assessment of IR-UWB body area network (BAN) based on IEEE 802.15.6 standard. *IEEE Antenn Wireless Propag Lett* (2016) 15:1645–8. doi:10.1109/LAWP.2016.2520021

3. Li A, Singh S, Sievenpiper D. Metasurfaces and their applications. *Nanophotonics* (2018) 7:989–1011. doi:10.1515/nanoph-2017-0120

4. Luo Z, Chen MZ, Wang ZX, Zhou L, Li YB, Cheng Q, et al. Digital nonlinear metasurface with customizable nonreciprocity. *Adv Funct Mater* (2019) 29:1906635. doi:10.1002/adfm.201906635

5. Moccia M, Liu S, Wu RY, Castaldi G, Andreone A, Cui TJ, et al. Coding metasurfaces for diffuse scattering: scaling laws, bounds, and suboptimal design. *Adv Opt Mater* (2017) 5:1700455. doi:10.1002/adom.201700455

DATA AVAILABILITY STATEMENT

The raw data supporting the conclusions of this article will be made available by the authors, without undue reservation.

AUTHOR CONTRIBUTIONS

SY designed and performed the design and simulation as well as wrote the paper. All authors participated in the data analysis and read the manuscript.

6. Rabinovich O, Epstein A. Analytical design of printed circuit board (pcb) metagratings for perfect anomalous reflection. *IEEE Trans Antenn Propag* (2018) 66:4086–95. doi:10.1109/tap.2018.2836379

7. Yang R, Li D, Gao D, Zhang A, Hu B, Yang P, et al. Negative reflecting meta-mirrors. *Sci Rep* (2017) 7:5729. doi:10.1038/s41598-017-06184-1

8. Tao Z, Wan X, Pan BC, Cui TJ. Reconfigurable conversions of reflection, transmission, and polarization states using active metasurface. *Appl Phys Lett* (2017) 110:121901. doi:10.1063/1.4979033

9. Zhang L, Wan X, Liu S, Yin JY, Zhang Q, Wu HT, et al. Realization of low scattering for a high-gain fabry-perot antenna using coding metasurface. *IEEE Trans Antenn Propag* (2017) 65:3374–83. doi:10.1109/tap.2017.2700874

10. Zheng Q, Li Y, Zhang J, Ma H, Wang J, Pang Y, et al. Wideband, wide-angle coding phase gradient metasurfaces based on pancharatnam-berry phase. *Sci Rep* (2017) 7:43543. doi:10.1038/srep43543

11. Su J, Lu Y, Zhang H, Li Z, Yang Y, Che Y, et al. Ultra-wideband, wide angle and polarization-insensitive specular reflection reduction by metasurface based on parameter-adjustable meta-atoms. *Sci Rep* (2017b) 7:42283. doi:10.1038/srep42283

12. Ratni B, Bochkova E, Piau G-P, de Lustrac A, Lupu A, Burokur SN. Design and engineering of metasurfaces for high-directivity antenna and sensing applications. *EPJ Appl Metamater* (2016) 3:4. doi:10.1051/epjam/2016008

13. Chen K, Zhang N, Ding G, Zhao J, Jiang T, Feng Y. Active anisotropic coding metasurface with independent real-time reconfigurability for dual polarized waves. *Adv Mater Technol* (2020) 5:1900930. doi:10.1002/admt.201900930

14. Su J, Kong C, Li Z, Yin H, Yang Y. Wideband diffuse scattering and rcs reduction of microstrip antenna array based on coding metasurface. *Electron Lett* (2017a) 53:1088–9. doi:10.1049/el.2017.1656

15. Chaimool S, Hongnara T, Rakluea C, Akkaraekthalin P, Zhao Y. Design of a pin diode-based reconfigurable metasurface antenna for beam switching applications. *Int J Antenn Propag* (2019) 2019:1–7. doi:10.1155/2019/7216324

16. Modi AY, Balanis CA, Birtcher CR, Shaman HN. New class of rcs-reduction metasurfaces based on scattering cancellation using array theory. *IEEE Trans Antenn Propag* (2019) 67:298–308. doi:10.1109/TAP.2018.2878641

17. Huang H, Omar AA, Shen Z. Low-rcs and beam-steerable dipole array using absorptive frequency-selective reflection structures. *IEEE Trans Antenn Propag* (2019) 68:2457–62. doi:10.1109/TAP.2019.2943322

18. Zhang XG, Tang WX, Jiang WX, Bai GD, Tang J, Bai L, et al. Light-controllable digital coding metasurfaces. *Adv Sci* (2018) 5:1801028. doi:10.1002/advs.201801028

19. Vellucci S, Monti A, Barbuto M, Toscano A, Bilotti F. Waveform-selective mantle cloaks for intelligent antennas. *IEEE Trans Antenn Propag* (2019) 68:1717–25. doi:10.1109/TAP.2019.2948736

20. Phon R, Ghosh S, Lim S. Novel multifunctional reconfigurable active frequency selective surface. *IEEE Trans Antenn Propag* (2019) 67:1709–18. doi:10.1109/TAP.2018.2889002

21. Wu H, Bai GD, Liu S, Li L, Wan X, Cheng Q, et al. Information theory of metasurfaces. *Nat Sci Review* (2019) 7:561–71. doi:10.1093/nsr/nwz195

22. Zhang L, Wang ZX, Shao RW, Shen JL, Chen XQ, Wan X, et al. Dynamically realizing arbitrary multi-bit programmable phases using a 2-bit time-domain coding metasurface. *IEEE Trans Antenn Propag* (2019) 68:2984–921. doi:10.1109/TAP.2019.2955219

23. Wang Q, Zhang XG, Tian HW, Jiang WX, Bao D, Jiang HL, et al. Millimeter–wave digital coding metasurfaces based on nematic liquid crystals. *Adv Theory Simul* (2019) 2:1900141. doi:10.1002/adts.201900141

Check for updates

Hybrid Metamaterials Perfect Absorber and Sensitive Sensor in Optical Communication Band

Xuehan Liu[1], Keyang Li[1], Zhao Meng[2], Zhun Zhang[1]* and Zhongchao Wei[1]

[1]Guangdong Provincial Key Laboratory of Nanophotonic Functional Materials and Devices, School of Information and Optoelectronic Science and Engineering, South China Normal University, Guangzhou, China, [2]Guangdong Women and Children Hospital, Guangzhou, China

A subwavelength metamaterial perfect absorber (MPA) in optical communication band was proposed and tested using the finite-difference time-domain method. The absorber is periodic and comprises a top layer of diamond silicon surrounded by L-shaped silicon and a gold layer on the substrate. It can achieve dual-band perfect absorption, and one of the peaks is in the optical communication band. By changing the gap (g) between two adjacent pieces of L-shaped silicon, and the thickness (h) of the silicon layer, the resonance wavelength of absorption peak can be tuned. When the incident electromagnetic wave entered the absorber, the metamaterial absorber could almost completely consume the incident electromagnetic waves, thereby achieving more than 99% perfect absorption. The absorption peak reaches 99.986% at 1310 nm and 99.421% at 1550 nm. Moreover, the MPA exposed to different ambient refraction indexes can be applied as plasma sensors, and can achieve multi-channel absorption with high figure of merit (FOM*) value and refractive index (RI) sensitivity. The FOM* values at 1310 nm and 1550 nm are 6615 and 168, respectively, and both resonance peaks have highly RI sensitivity. The results confirm that the MPA is a dual-band, polarization-independent, wide-angle absorber and insensitive to incident angle. Thence it can be applied in the fields of optical communication, used as a light-wave filter and plasma sensor, and so on.

Keywords: metamaterial, perfect absorber, optical communication band, finite difference time domain method, sensor

1 INTRODUCTION

Electromagnetic metamaterials are an artificial composite structure or composite material with extraordinary electromagnetic properties that natural materials do not possess, and research on these materials has attracted considerable attention and made significant progress in recent years [1, 2]. Using electromagnetic metamaterials can achieve arbitrary "cutting" of electromagnetic and light wave properties, thus creating peculiar electromagnetic characteristics such as perfect lens [3, 4], negative refractive index [5], and electromagnetic stealth [6]. An attractive application field of metamaterials is the "perfect absorber" of electromagnetic waves [8, 9]. The concept of the perfect absorber was originally proposed by Landy et al in 2008 [10]. After then, a large range of absorbers with dielectric disks, ribbons, rings, and diamond arrays have been proposed and demonstrated [11–20]. In these studies, perfect absorbers in visible, infrared, and terahertz (THz) range were presented [21–28]. For instance, Li et al. proposed a novel broadband metamaterial perfect absorber based on visible light [12]. Xu et al. demonstrated an ultra-broadband metamaterial absorber in a

frequency range of 3–7.8 THz [29]. A multi-channel plasmonic perfect absorber based on the mid-infrared region was proposed by Meng et al. [13]. A triple-band perfect absorber based on the infrared range was designed by Wu et al. [30]. Most of them are metamaterial-based electromagnetic resonance absorbers. By rationally designing the physical size and material parameters, the metamaterial can be coupled with the electromagnetic component of the incident electromagnetic wave, so that the electromagnetic waves incident on the specific broadband of the absorber can be 100% absorbed. At present, the potential applications of perfect absorbers include bolometer [10], electromagnetic stealth [31], and thermal emission [32].

Optical communication is a communication method using light waves as carriers. The two most obvious advantages of optical communications are transmission distance and capacity. Wavelength-division multiplexing technology ensures that the optical fiber system has a strong transmission capacity, so it can be applied to cross-sea communication systems. Optical communication also has an extremely wide transmission frequency band, with high information-transmission efficiency and a strong ability to resist electromagnetic interference, which can maintain high communication-transmission quality in various application environments. Furthermore, the optical communication bands have the lowest loss, the smallest dispersion, and the lowest microbending loss, providing a comprehensive array of applications in optical amplifier long-distance trunk systems and submarine cable systems. Therefore, we planned to combine the metamaterial perfect absorber with the optical communication band for our study, that is, we want to realize the resonance absorption window in the optical communication band.

In this article, a metamaterial perfect absorber (MPA) in optical communication band is proposed. The absorber comprises a diamond silicon surrounded by four L-shaped pieces of silicon, which were placed on a metallic plate to prevent energy from seeping out of the system. The number of electromagnetic response modes of the top structural unit determines the number of metamaterial absorption peaks; therefore, our proposed absorber has dual-band perfect absorption. Finite-difference time-domain (FDTD) simulations showed that there are two absorption peaks above 99% after optimization, and the wavelength of one of the absorption peaks was at an optical communication wavelength. According to the effective medium theory [7], the characteristics of metamaterials can be characterized by the effective dielectric constant and permeability, whereas the effective dielectric constant and permeability of metamaterials can be controlled by the orderly design of the material's key physical dimensions. Therefore, the resonance wavelength of absorption peak can be tuned by changing the geometrical dimensions of the structure, such as gap (g) between two adjacent L-shaped pieces of silicon, and the thickness (h) of the silicon layer. In addition, the designed MPA achieves near-perfect polarization independence and incident angle-insensitive dual-band light absorption. For the incident angle, the simulation results show that the designed structure realizes wide-angle absorption of 0°–40° for TM waves and TE waves, displaying a relatively perfect absorption effect. Moreover,

the MPA exposed to different ambient refraction indexes can be applied to the field of plasma sensors, and can achieve multi-channel absorption with high FOM* value and RI sensitivity. The proposed subwavelength structure has important value in the fields of light-wave filters, thermal radiation meters, array thermal imaging detectors, and electromagnetic wave modulators.

2 MATERIALS AND METHODS

The structure stereogram of the proposed MPA is shown in **Figure 1A**. There are four L-shaped [33–36] structures of the same size in a unit cell, as shown in **Figure 1B**. The upper layer is a resonator formed by a structure in which four L-shaped dielectrics surround a diamond-shaped dielectric, and the lower layer is a metal substrate. The optimized parameters of each part of 1310 nm structure and 1550 nm structure are marked in **Table 1**. Here, the resonance wavelength of the absorption peak was tuned by changing the structural parameters of the absorber to move the absorption peak from 1310 nm to 1550 nm. The two arm lengths of L-shaped silicon, distance between each two adjacent L-shaped silicon, thickness of the patterned silicon layer and structural periodicity are fixed at L, g, h and P, respectively. The arm widths of L-shaped silicon, semi-major axis and semi-minor axis of the diamond silicon are W, a and b, respectively. In the simulations, the incident light appears perpendicularly on the patterned silicon structure metamaterial absorber in the negative direction of the z-axis, with the electric field along the x direction and the magnetic field along the y direction. The mesh size in a patterned silicon layer is $\Delta x = \Delta y = 4$ nm, and $\Delta z = 6$ nm. The simulation time and mesh accuracy were set to 15,000 (fs) and 4, respectively. The permittivity of Si and Au in the near-infrared region were obtained from the experiments of Palik and CRC [41]. The periodic boundary conditions were set in both x and y directions to reproduce this array, and the boundary condition along the z direction was the perfectly matched layer (PML) to eliminate scattering.

The material of the metal substrate is gold, and the thickness of the gold reflection mirror is defined as t = 100 nm. The skin depth δ (or penetration depth) commonly used in engineering to characterize the skin depth of electromagnetic waves, which is defined as the distance the electromagnetic wave travels when the amplitude of the electromagnetic wave is attenuated to the surface value $1/e$ (or 0.368). According to this definition, it can be described as [37–40].

$$e^{-\alpha\delta} = {}^1\!/_e \tag{1}$$

therefore,

$$\delta = \sqrt{\frac{2}{\omega\mu\sigma}} \tag{2}$$

where ω is the angular frequency of the electromagnetic wave, μ is the magnetic permeability, and σ is the electrical conductivity. The thickness of the bottom metal plate is calculated as 100 nm, which is much greater than the skin depth δ of gold in this
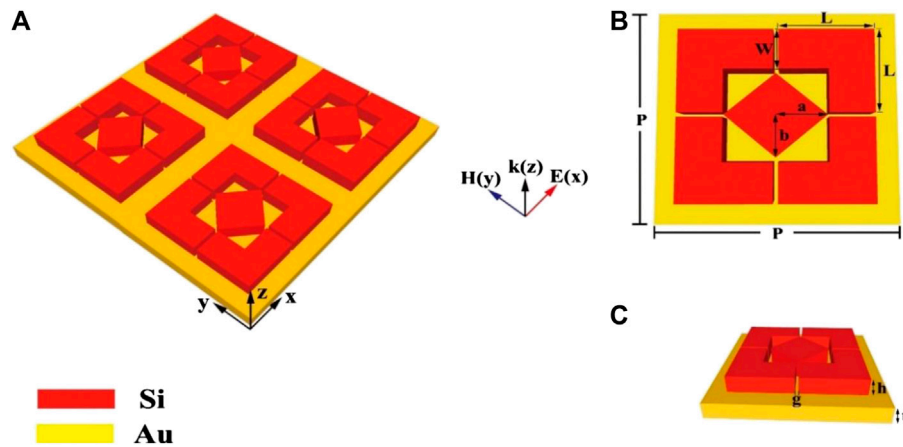
FIGURE 1 | (A) Perspective view of the MPA device structure. (B) Top view of the unit cell structure. (C) Side view of the unit cell structure.

TABLE 1 | Comparison of parameters of 1310 nm structure and 1550 nm structure.

Parameter	1310 nm structure	1550 nm structure
L (nm)	307	
W (nm)	142	157
a (nm)	167	153
b (nm)	164	150
g (nm)	6	
h (nm)	281	
P (nm)	844	

wavelength range. Therefore, the electromagnetic wave cannot penetrate the metal layer, the transmission coefficient of the absorber structure is always 0, and the absorption is only affected by the reflection coefficient. When electromagnetic waves occur on the metamaterial structure, electric field resonance and magnetic field resonance will occur in the absorber, accompanied by the generation of effective dielectric constant $\varepsilon(\omega)$ and effective permeability $\mu(\omega)$. This is due to

$$n(\omega) = \sqrt{\varepsilon(\omega)\mu(\omega)} \tag{3}$$

$$Z(\omega) = \sqrt{\mu(\omega)/\varepsilon(\omega)} \tag{4}$$

where $n(\omega)$ is the refractive index of the dielectric, and $Z(\omega)$ is the impedance of the dielectric material. Suppose $\varepsilon(\omega) = \varepsilon(\omega)' + i\varepsilon(\omega)''$, $\mu(\omega) = \mu(\omega)' + i\mu(\omega)''$. At a specific resonance frequency, when $\varepsilon(\omega)' = \mu(\omega)'$, $\varepsilon(\omega)'' = \mu(\omega)''$, that is, the effective dielectric constant $\varepsilon(\omega)$ and effective permeability $\mu(\omega)$ of the absorbing material are equal, the effective impedance of the absorber matches the wave impedance $Z(\omega)$ in free space. At this time, in the case of normal incidence of electromagnetic waves, the reflectance is

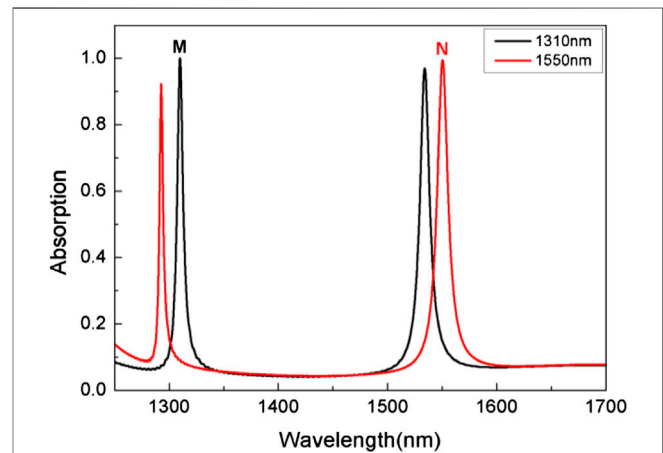$$R = \left| \frac{Z - Z_0}{Z + Z_0} \right|^2 = \left| \frac{\mu_r - n}{\mu_r + n} \right|^2 \tag{5}$$

FIGURE 2 | Simulated absorbance of the proposed MPA, whose structure is shown in **Figure 1**. The black solid line and the red solid line correspond to wavelengths of 1310 nm and 1550 nm, respectively. The corresponding peak at 1310 nm is labeled M, and the corresponding peak at 1550 nm is labeled N.

which equals zero, and where $n = \sqrt{\varepsilon_r \mu_r}$ is the refractive index coefficient of the dielectric, $Z = \sqrt{\mu/\varepsilon}$ represents the dielectric material impedance, and $Z_0 = \sqrt{\mu_0/\varepsilon_0}$ represents the free space impedance. When the thickness of the bottom metal layer is greater than the penetration depth of the electromagnetic wave, so that electromagnetic waves cannot pass through the material, the transmittance is

$$T = \left[\cos(nkl) - \frac{i}{2}\left(z + \frac{1}{z}\right)\sin(nkl) \right]^{-1} \tag{6}$$

which is almost equal to zero. The electromagnetic wave is confined to the inside of the structure until it is completely consumed by the dielectric layer or the metal layer. According to Kirchhoff's theorem, the sum of absorptance A, transmittance
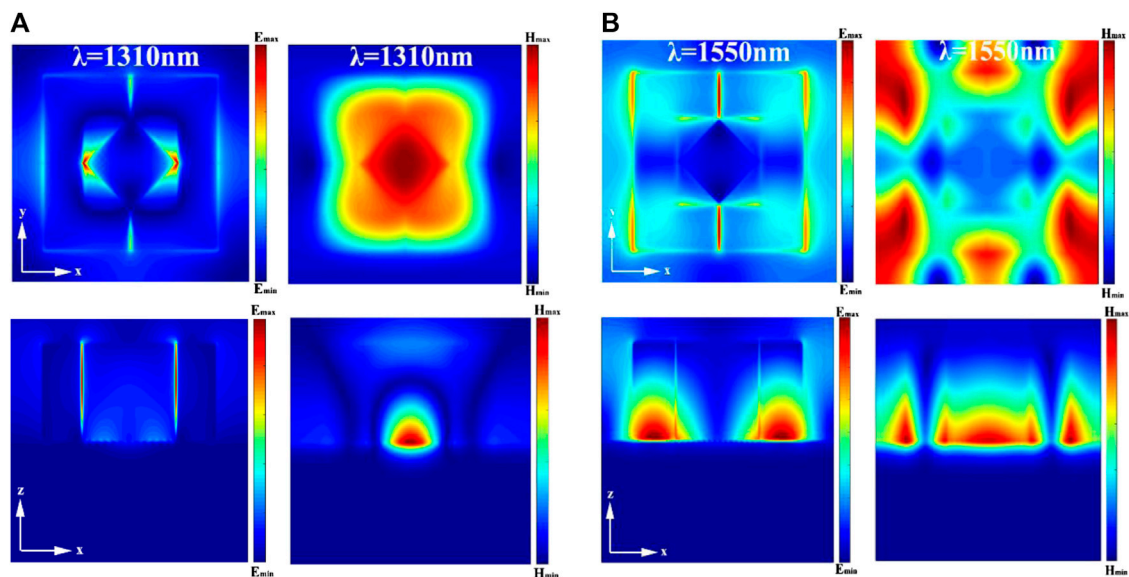
FIGURE 3 | Electric and magnetic field intensity distribution diagram of the top planes (xoy) and cross-sectional planes (xyz) of the unit cell structure at the absorption peak of **(A)** 1310 nm, and **(B)** 1550 nm.

T, and reflectance R is equal to 1, that is, $A+ T + R = 1$, so the absorptance is

$$A = 1 - R = 1 - \left|\frac{Z - Z_0}{Z + Z_0}\right|^2 = 1 - \left|\frac{\mu_r - n}{\mu_r + n}\right|^2 \quad (7)$$

It can be seen from **Eq. 7** that if the frequency corresponding to the incident spatial impedance of the electromagnetic wave and the impedance of the dielectric layer have $Z = Z_0$, the electromagnetic wave is absorbed without reflection, and the electromagnetic wave of a specific wavelength band can be absorbed at close to 100%.

3 RESULTS AND DISCUSSION

Tunable Hybrid Metamaterial Absorber

The absorption spectrum of the proposed MPA in the optical communication band as a function of wavelength was calculated, as seen in **Figure 2**. The black solid line indicates that the peak on the left (labeled M) in the absorption spectrum corresponds to a wavelength of 1310 nm, and the peak value at M is up to 99.986%, so we call it 1310 nm for short. The red solid line indicates that the peak on the right (labeled N) in the absorption spectrum corresponds to a wavelength of 1550 nm, and the absorption at N reaches 99.421%; thus, we simply call it 1550 nm. Through a comparison of **Table 1**, we found that the resonant wavelength could be effectively tuned from 1310nm to 1550 nm by changing the semi-major axis (a) and the semi-minor axis (b) of the diamond silicon, and the arm widths (W) of the L-shaped silicon. The spectrum is shown in **Figure 2**.

To better understand the physical mechanism of the proposed dual-channel perfect absorption, the electric and magnetic field

intensity distributions of the unit cell structure at M and N are shown in **Figure 3**. The top (xoy) planes and cross-sectional (xyz) planes are plotted. In **Figure 3A**, it can be seen that the electric field at 1310 nm is mainly distributed between the closely adjacent diamond silicon and L-shaped silicon due to the localized surface plasmon resonance (LSPR), whereas the strong magnetic field is distributed in the diamond. This indicates that there is both electric dipole resonance and magnetic dipole resonance at the 1310 nm wavelength [15, 42, 43]. However, contrary to the electromagnetic field intensity distribution at 1310 nm, it can be clearly seen from **Figure 3B** that at the 1550 nm wavelength, the enhanced electric field is mainly concentrated between the bottom of the resonator and the gold film of the reflective layer. There is also a partly weak electric field distribution between the resonators, and the magnetic field strength is distributed in the dielectric layer. The reason is that a strong enhancement of the localized electromagnetic field is excited at the resonance frequencies between the two layers, and this effect results in almost zero reflectance observed in simulations and calculations [16]. These characteristics confirm that the absorption at the 1550 nm wavelength is caused by the coupling of the dipole resonance of the resonator and the second resonance of the silicon wafer.

To further understand the working mechanism of the proposed MPA, the absorption under different structural parameters was studied. **Figure 4** shows the calculated absorption intensity for the structure at 1310 nm and 1550 nm by varying the g parameter. For these two wavelengths, both the g values were changed from 2 nm to 18 nm, with an interval of 4 nm. The trends of both wavelengths with the change of g value are almost the same, as shown in **Figures 4A,B**. The absorption peaks of both wavelengths are blue-shifted with the increases of g value. The plasmon resonance will occur when SPPs resonate on
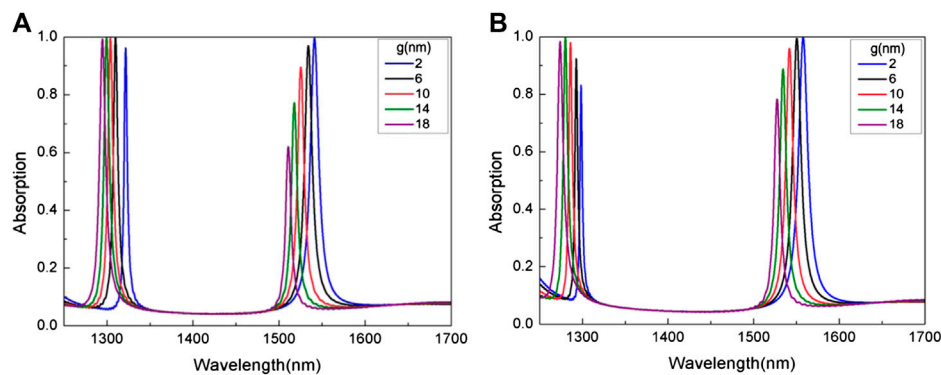
FIGURE 4 | Absorption spectrum for different gaps (g) between two adjacent L-shaped silicon of **(A)** 1310 nm and **(B)** 1550 nm. Other parameters are consistent with those in **Figure 1**.
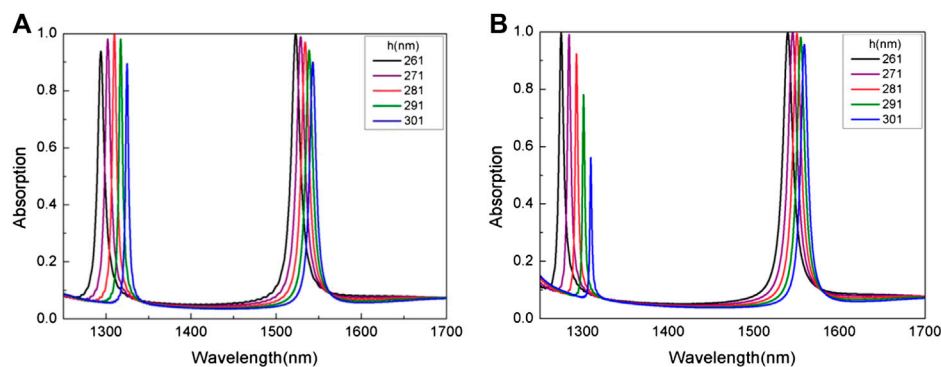

FIGURE 5 | Absorption spectrum for the silicon layer h with different thicknesses at **(A)** 1310 nm and **(B)** 1550 nm. Other structural parameters are consistent with those in **Figure 1**.

the horizontal surface of L-shaped silicon, and the resonance conditions of L-shaped silicon can be expressed as [30].

$$2k_{sp}L_{eqv} + 2\delta = 2\rho\pi \tag{8}$$

where $k_{sp} = 2\pi n_{sp}/\lambda_m$, n_{sp} is the effective index of SPPs and λ_m is the resonance wavelength, and L_{eqv} denotes the equal resonance arm length, δ means the phase change at the end of the horizontal arms, and ρ is an integer; as the incident wavelength is larger than the arm length, ρ can be regarded as 1. Then, the resonance wavelength can be simplified as [30].

$$\lambda_m = 2\pi n_{sp}L_{eqv}\big/(\pi - \delta) \tag{9}$$

It can be discovered from Formula (9) that the resonance wavelength is proportional to the effective arm length of the L-shaped silicon, and the absorption peak undergoes a redshift as the arm length (L) increases. However, the sum of L and g is fixed: as g increases, L decreases, which is presented in **Figure 4**.

The next observation is the effect of different thicknesses of the silicon layer on the absorption spectrum, and the results obtained are shown in **Figure 5**. Other geometric parameters remain

unchanged, and the thickness (h) of the silicon layer increases from 261 nm to 301 nm, with an interval of 10 nm. It can be seen from **Figures 5A,B** that both absorption peaks experience a redshift with the increase of h.

Polarization independence and incident angle insensitivity are important factors that should be considered in practical applications. **Figure 6** and **Figure 7** show the influence of the incident angle in the TM mode and TE mode and the polarization angle on the absorption performance in the 1310 nm and 1550 nm structures, respectively. It can be seen that as the incident angle increases from 0° to 40°, the absorption peak still achieves nearly uniform perfect absorptance at the resonance frequency. It indicates that the absorption of the absorber is insensitive to the incident angle, the reason may be due to the structural symmetry of the absorber. **Figure 6C** and **Figure 7C** show the relationship between the variety of polarization angle and the absorption spectrum under normal incidence. Due to the high symmetry and the local resonance of the structure, the position and intensity of the absorption peak remain almost unchanged when the polarization angle changes from 0° to 90° in 10° increments at normal incidence. Therefore, the metamaterial absorber is independent of polarization.
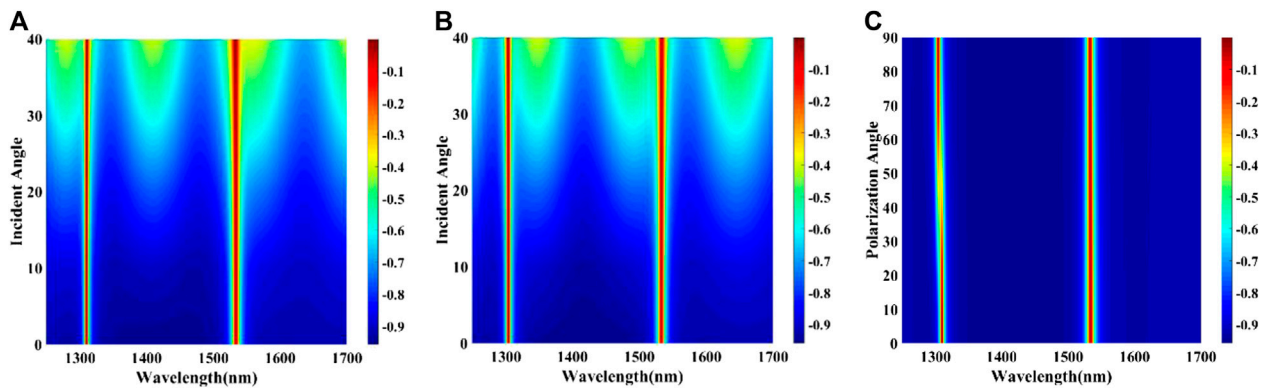
FIGURE 6 | In the 1310 nm structure, tuned incident angle from 0° to 40° in **(A)** TM mode and **(B)** TE mode, and **(C)** the variety of polarization angle from 0° to 90° under normal incidence.
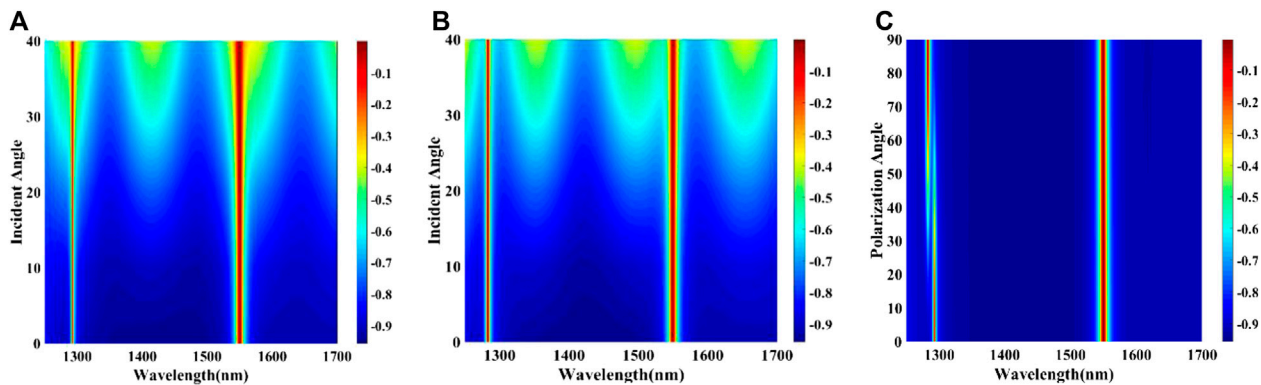

FIGURE 7 | In the 1550 nm structure, tuned incident angle from 0° to 40° in **(A)** TM mode and **(B)** TE mode, and **(C)** the variety of polarization angle from 0° to 90° under normal incidence.

FIGURE 8 | (A) The reflectance spectra exposed to different ambient refraction indexes, and **(B)** the relationship between resonance wavelength and refractive index in 1310 nm structure.

Polarization-insensitive metamaterial perfect absorbers have been widely used in optoelectronic devices including thermoelectric devices.

Tunable Hybrid Metamaterial Sensor

The reflectance spectrum with different ambient refractive indices at 1310 nm and 1550 nm are illustrated in **Figure 8A**
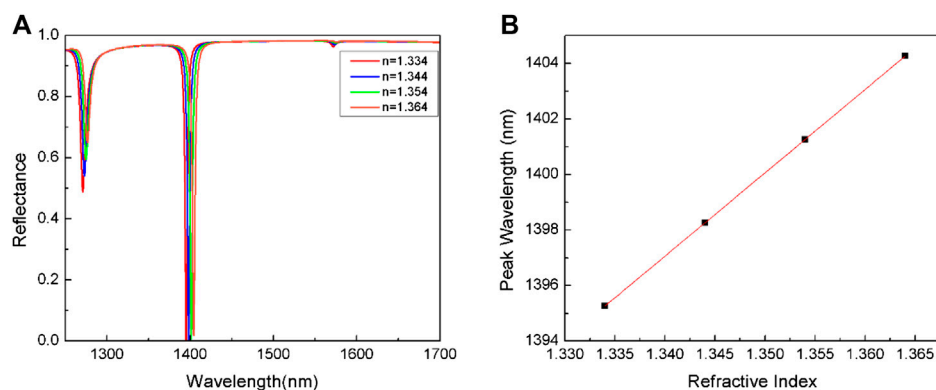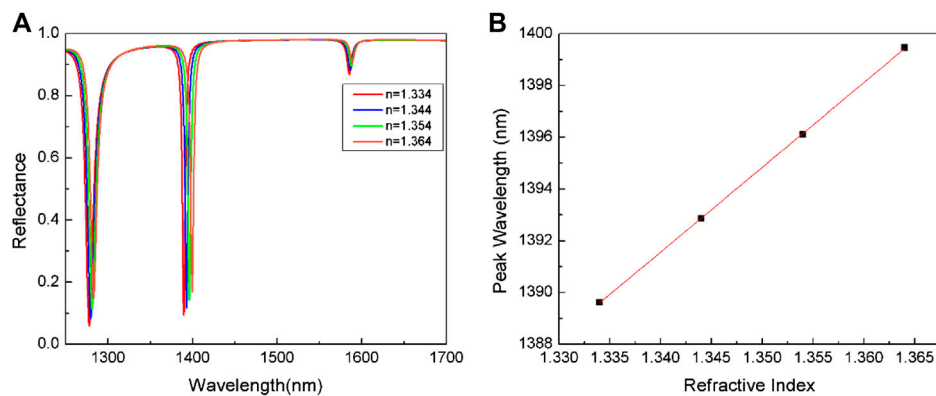
FIGURE 9 | (A) The reflectance spectra exposed to different ambient refraction indexes, and **(B)** the relationship between resonance wavelength and refractive index in 1550 nm structure.
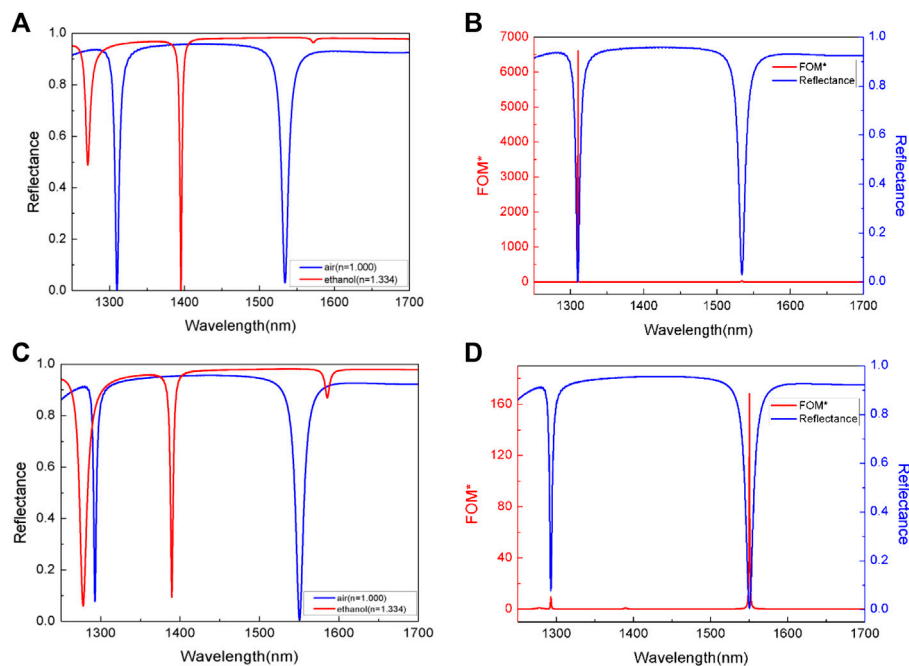

FIGURE 10 | (A,C) Reflectance spectra and **(B,D)** FOM* values of 1310 nm and 1550 nm structures with air and ethanol solution as medium.

and **Figure 9A**, respectively. They are both red-shifted by increasing the refraction index from 1.334 to 1.364, and the reflection intensities is decreasing. Here, we take the high-frequency reflection wavelength (near 1400 nm) in **Figure 8A** and **Figure 9A** as an example to obtain the relationship between resonance wavelength and refractive index, as shown in **Figure 8B** and **Figure 9B**. The black dots are the resonant wavelengths under different ambient refraction indexes, the red line is obtained by linear fitting, and the fitting degree is close to or equal to 1. And these two images have a common point that the resonance wavelength increases with the increase of refractive index. Moreover, the low-frequency

and high-frequency RI sensitivities of the 1310 nm structure are 185.1 nm/RIU, 300.0 nm/RIU, respectively. The low-frequency and high-frequency RI sensitivities of the 1550 nm structure are 168 nm/RIU and 328 nm/RIU, respectively. The results show that the two resonance peaks of the absorber both have high sensitivity and can be used in the field of dual-band sensors.

We used figure of merit (FOM*) to measure the sensitivity of the refractive index sensor. The FOM* value means the change in reflectance intensity caused by the diversification in the ambient refractive indices around the perfect absorber. The larger the FOM* value, the higher the sensitivity of the refractive index sensor. The expression is as follows [44]:
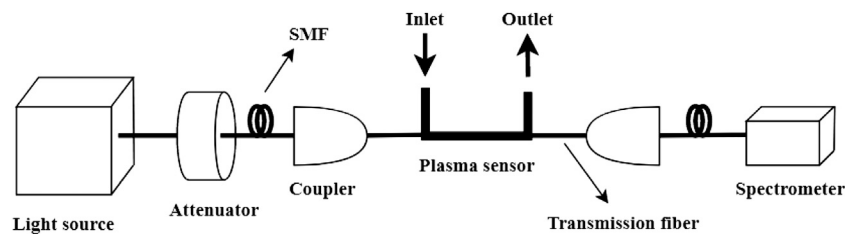
FIGURE 11 | Diagram of system device used for chemical solution concentration detection.

$$FOM^* = MAX|[dI(\lambda)/dn(\lambda)]/I(\lambda)| \qquad (10)$$

where $dI(\lambda)/dn(\lambda)$ is the change of relative reflection intensity caused by the variations of the environmental refractive index at the resonance wavelength, and $I(\lambda)$ represents reflectivity. Taking ethanol solution as an example, **Figures 10A,C** show the reflection spectra of 1310 nm and 1550 nm structures with air and ethanol solution as the environmental media, respectively. It can be seen from the figures that the reflection spectrum of the ethanol solution as the medium is blue-shifted compared with the air as the medium. From **Figures 10B,D**, it can be found that the FOM* value near the reflection valley at 1310 nm and 1550 nm is the largest, the value is 6615 and 168, respectively, which indicates that the absorber can be used as a sensor in the optical communication band.

The system that plasma sensor for detection of chemical solution concentration is shown in **Figure 11**. The light source firstly weakens the light intensity through optical attenuator, and then enters the plasma sensor by transmission fiber and coupler. The light being modulated by the detection sample in the sensing area is received by the spectrometer, and it performs photoelectric conversion in the spectrometer and records the signal processing unit in real time. Finally, the detection signal can be obtained by normalized spectral processing.

4 CONCLUSION

A metal-dielectric dual-channel metamaterial perfect absorber in the optical communication band was proposed, and a single patterned silicon layer and a bottom gold layer were used for structural design. The simulation of the designed subwavelength structure was carried out using the FDTD method. By designing and optimizing the structure, size, and arrangement of metamaterial artificial units, the effective dielectric constant of the absorbing material is equal to the effective magnetic permeability, the electromagnetic wave of this frequency band completely enters the absorber and is hardly reflected, which will cause perfect absorption of the incident wave, thereby achieving a high absorption rate. The regulation of the resonance absorption position with the structural parameters was studied further. The effective adjustment of the absorption peak position was achieved

by changing the arm length, thickness of the dielectric layer. Moreover, the combination of four identical L-shaped and diamond-shaped structures could achieve dual-band perfect absorption, and was polarization independent, wide-angle, incident-angle insensitive. The absorber can be used as a refraction index sensor. The results show that the FOM* values at 1310 nm and 1550 nm are the highest, at 6615 and 168, respectively. The calculated high RI sensitivity further showed that the designed perfect absorber could be used in the field of detectors, sensors and filters, with the potential for application in related fields.

DATA AVAILABILITY STATEMENT

The original contributions presented in the study are included in the article/Supplementary Material, further inquiries can be directed to the corresponding author.

AUTHOR CONTRIBUTIONS

Conceptualization, ZW and ZZ; methodology, ZZ; software, XL; validation, XL, ZW, KL, and ZZ; formal analysis, ZW and ZZ; investigation, XL; resources, XL, KL, ZM; data curation, XL, ZM, and KL; writing—original draft preparation, XL; writing—review and editing, XL and ZW; visualization, ZW; supervision, ZZ; project administration, ZZ; funding acquisition, ZW. All authors have read and agreed to the published version of the manuscript.

FUNDING

ACKNOWLEDGMENTS

REFERENCES

1. Sreekanth KV, ElKabbash M, Caligiuri V, Singh R, De Luca A, Strangi G. Graphene and topological insulator-based active THz hyperbolic metamaterials. In *New Directions in thin film nanophotonics, progress in optical science and Photonics*. Singapore: Springer (2019) 6:159–72. doi:10.1007/978-981-13-8891-0_9

2. Chang YC, Kildishev AV, Narimanov EE, Norris TB. Metasurface perfect absorber based on guided resonance of a photonic hypercrystal. *Phys Rev B* (2016) 94:155430. doi:10.1103/PhysRevB.94.155430

3. Pendry JB. Negative refraction makes a perfect lens. *Phys Rev Lett* (2000) 85: 3966–9. doi:10.1103/PhysRevLett.85.3966

4. Casse BDF, Lu WT, Huang YJ, Gultepe E, Menon L, Sridhar S. Super-resolution imaging using a three-dimensional metamaterials nanolens. *Appl Phys Lett* (2010). 96: 1–3. doi:10.1063/1.3291677

5. Ramakrishna SA, Grzegorczyk TM. *Physics and applications of negative refractive index materials*. Bellingham, Washington: CRC (2008) 1–415. doi:10.1201/9781420068764

6. Liu R, Ji C, Mock JJ, Chin JY, Cui TJ, Smith DR. Broadband ground-plane cloak. *Science* (2009). 323:366–9. doi:10.1126/science.1166949

7. Smith DR, Pendry JB. Homogenization of metamaterials by field-averaging. *J Opt Soc Am B* (2006) 23:391–403. doi:10.1364/JOSAB.23.000391

8. Wang Z, Tong Z, Ye Q, Hu H, Nie X, Yan C, et al. Dynamic tuning of optical absorbers for accelerated solar-thermal energy storage. *Nat Commun* (2017) 8: 1478. doi:10.1038/s41467-017-01618-w

9. Monti A, Alù A, Toscano A, Bilotti F. The design of optical circuit-analog absorbers through alectrically small nanoparticles. *Photonics* (2019) 6:26. doi:10.3390/photonics6010026

10. Landy NI, Sajuyigbe S, Mock JJ, Smith DR, Padilla WJ. Perfect metamaterial absorber. *Phys Rev Lett* (2008) 100:207402. doi:10.1103/PhysRevLett.100.207402

11. Zhao X, Wang Y, Schalch J, Duan G, Cremin K, Zhang J, et al. Optically modulated ultra-broadband all-silicon metamaterial terahertz absorbers. *Acs Photon* (2019) 6:830–7. doi:10.1021/acsphotonics.8b01644

12. Li C, Fan H, Wei Z, Lan S, Liu H. Multipole resonance in arrays of diamond dielectric: a metamaterial perfect absorber in the visible regime. *Nanomaterials* (2019) 9:1222. doi:10.3390/nano9091222

13. Meng HY, Xue XX, Lin Q, Liu GD, Zhai X, Wang LL. Tunable and multi-channel perfect absorber based on graphene at mid-infrared region. *Appl Phys Express* (2018) 11:052002. doi:10.7567/APEX.11.052002

14. Pradhan JK, Anantha Ramakrishna S, Rajeswaran B, Umarji AM, Achanta VG, Agarwal AK, et al. High contrast switchability of VO2 based metamaterial absorbers with ITO ground plane. *Opt Express* (2017) 25:9116–21. doi:10.1364/OE.25.009116

15. Lu X, Wan R, Zhang T. Metal-dielectric-metal based narrow band absorber for sensing applications. *Opt Express* (2015) 23:29842–7. doi:10.1364/oe.23.029842

16. Zhang B, Zhao Y, Hao Q, Kiraly B, Khoo IC, Chen S, et al. Polarization-independent dual-band infrared perfect absorber based on a metal-dielectric-metal elliptical nanodisk array. *Opt Express* (2011) 19:15221–8. doi:10.1364/OE.19.015221

17. Ke S, Wang B, Huang H, Long H, Wang K, Lu P. Plasmonic absorption enhancement in periodic cross-shaped graphene arrays. *Opt Express* (2015) 23: 8888–900. doi:10.1364/OE.23.008888

18. Si J, Dong Z, Yu X, Deng X. Tunable polarization-independent dual-band coherent perfect absorber based on metal-graphene nanoring structure. *Opt Express* (2018) 26:21768–77. doi:10.1364/OE.26.021768

19. Ra'di Y, Asadchy VS, Kosulnikov SU, Omelyanovich MM, Morits D, Osipov AV, et al. Full light absorption in single arrays of spherical nanoparticles. *ACS Photon* (2015) 2:653–60. doi:10.1021/acsphotonics.5b00073

20. Alessio M, Andrea A, Alessandro T, Filiberto B. Narrowband transparent absorbers based on ellipsoidal nanoparticles. *Appl Opt* (2017) 56:7533–8. doi:10.1364/AO.56.007533

21. Yao G, Ling F, Yue J, Luo C, Ji J, Yao J. Dual-band tunable perfect metamaterial absorber in the THz range. *Opt Express* (2016) 24:1518–27. doi:10.1364/OE.24.001518

22. Sun P, You C, Mahigir A, Liu T, Xia F, Kong W, et al. Graphene-based dual-band independently tunable infrared absorber. *Nanoscale* (2018) 10:15564–70. doi:10.1039/c8nr02525h

23. Fann CH, Zhang J, ElKabbash M, Donaldson WR, Michael Campbell E, Guo C. Broadband infrared plasmonic metamaterial absorber with multipronged absorption mechanisms. *Opt Express* (2019) 27:27917–26. doi:10.1364/OE.27.027917

24. Xu H, Hu L, Lu Y, Xu J, Chen Y. Dual-band metamaterial absorbers in the visible and near-infrared regions. *J Phys Chem C* (2019) 123:10028–33. doi:10.1021/acs.jpcc.9b00434

25. De Souza ILG, Rodriguezesquerre VF. Design of planar and wideangle resonant color absorbers for applications in the visible spectrum. *Sci Rep* (2019) 9, 7045. doi:10.1038/s41598-019-43539-2

26. Peng C, Ou K, Li G, Li X, Wang W, Zhao Z, et al. Tunable phase change polaritonic perfect absorber in the mid-infrared region. *Opt Express* (2020) 28: 11721–9. doi:10.1364/OE.390000

27. Wu P, Zhang C, Tang Y, Liu B, Lv L. A perfect absorber based on similar fabry-pert four-band in the visible range. *Nanomaterials* (2020) 10:488. doi:10.3390/nano10030488

28. Rana AS, Mehmood MQ, Jeong H, Kim I, Rho J. Tungsten-based ultrathin absorber for visible regime. *Sci Rep* (2018) 8:2443. doi:10.1038/s41598-018-20748-9

29. Xu Z, Wu D, Liu Y, Liu C, Yu Z, Yu L, et al. Design of a tunable ultra-broadband terahertz absorber based on multiple layers of graphene ribbons. *Nanoscale Res Lett* (2018) 13:143. doi:10.1186/s11671-018-2552-z

30. Wu D, Wang M, Feng H, Xu Z, Liu Y, Xia F, et al. Independently tunable perfect absorber based on the plasmonic properties in double-layer graphene. *Carbon* (2019) 155:618–23. doi:10.1016/j.carbon.2019.09.024

31. Schurig D, Mock JJ, Justice BJ, Cummer SA, Pendry JB, Starr AF, et al. Metamaterial electromagnetic cloak at microwave frequencies. *science* (2006) 314:977–80. doi:10.1126/science.1133628

32. Watts CM, Liu X, Padilla WJ. Metamaterial electromagnetic wave absorbers. *Adv Mater Weinheim* (2012) 24:OP98-120. doi:10.1002/adma.201200674

33. Xiang Y, Wang L, Lin Q, Xia S, Qin M, Xiang Z. Tunable dual-band perfect absorber based on L-shaped graphene resonator. *IEEE Photonic Tech L* (2019) 31:483–6. doi:10.1109/LPT.2019.2900269

34. Bai Y, Zhao L, Ju D, Jiang Y, Liu L. Wide-angle, polarization-independent and dual-band infrared perfect absorber based on L-shaped metamaterial. *Opt Express* (2015) 23:8670–80. doi:10.1364/OE.23.008670

35. Wang A, Qu S, Yan M, Wang W, Wang J, Zheng L, et al. Six-band polarization-insensitive perfect metamaterial absorber using L-shaped resonators. *Appl Phys A* (2019) 125:1–7. doi:10.1007/s00339-019-2568-y

36. Gupta A, Chauhan M, Rajput A, Mukherjee B. Wideband backstop filter using L-shaped and Quad mode resonator for C and X band application. *Electromagnetics* (2020) 40:177–85. doi:10.1080/02726343.2020.1726003

37. Reuter GEH, Sondheimer EH. The theory of the anomalous skin effect in metals. *Nature* (1948) 161:336–64. doi:10.1038/161394a0

38. Olyslager F, De Zutter D. Skin effect. In *Wiley encyclopedia of electrical and electronics engineering*. New York, NY: Wiley (1999) 19:314–8. doi:10.1002/047134608x.W4949

39. Dyson FJ. Electron spin resonance absorption in metals. II. theory of electron diffusion and the skin effect. *Phys Rev* (1955) 98:349–59. doi:10.1103/PhysRev.98.349

40. Theye ML. Anomalous skin effect and size effect in thin metallic films. *Phys Lett A* (1967) 25:764–5. doi:10.1016/0375-9601(67)90984-X

41. Li J, Chen C, Jans H, Xu X, Verellen N, Vos I, et al. 300 mm Wafer-level, ultra-dense arrays of Au-capped nanopillars with sub-10 nm gaps as reliable SERS substrates. *Nanoscale* (2014) 6:12391–6. doi:10.1039/c4nr04315d

42. Cheng YZ, Mao XS, Wu CJ, Wu L, Gong RZ. Infrared non-planar plasmonic perfect absorber for enhanced sensitive refractive index sensing. *Opt Mater* (2016). 53:195–200. doi:10.1016/j.optmat.2016.01.053

43. Kuznetsov AI, Miroshnichenko AE, Fu YH, Zhang J, Luk'yanchuk B. Magnetic light. *Sci. Rep.* (2012) 2:492. doi:10.1038/srep00492

44. Sreekanth KV, ElKabbash M, Alapan Y, Rashed AR, Gurkan UA, Strangi G. A multiband perfect absorber based on hyperbolic metamaterials. *Sci Rep* (2016) 6:26272. doi:10.1038/srep26272

Advanced Electromagnetic Metamaterials for Temperature Sensing Applications

Liang Ma[1], Dexu Chen[1], Wenxian Zheng[2,3], Jian Li[1]*, Sidrish Zahra[1], Yifeng Liu[1], Yuedan Zhou[1], Yongjun Huang[1]* and Guangjun Wen[1]

[1] School of Information and Communication Engineering, Sichuan Provincial Engineering Research Center of Communication Technology for Intelligent IoT, University of Electronic Science and Technology of China, Chengdu, China, [2] Shenzhen Graduate School of Tsinghua University, Shenzhen, China, [3] Shenzhen Intellifusion Technologies Co., Ltd., Shenzhen, China

Metamaterials with novel properties have excited much research attention in the past several decades. Many applications have been proposed and developed for the reported metamaterials in various engineering areas. Specifically, for the resonant-type metamaterials with narrow resonance line width and strong resonance strength, the resonant frequency and strength are highly depended on the changings of meta-atom structure and/or substrate media properties induced by the environment physical or chemistry parameters varying. Therefore, physical or chemistry sensing applications for the resonant-type metamaterial units or arrays are developed in recent years. In this mini review, to help the researchers in those fields to catch up with the newly research advances, we would like to summarize the recently reported high-performance metamaterial-inspired sensing applications, especially the temperature sensing applications, based on different kinds of metamaterials. Importantly, by analyzing the advantages and disadvantages of several conventional metamaterial units, the newly proposed high quality-factor metamaterial units are discussed for high-precision sensing applications, in terms of the sensitivity and resolution. This mini review can guide researchers in the area of metamaterial-inspired sensors to find some new design routes for high-precision sensing.

Keywords: metamaterial, sensor, resonance, high quality factor, high precision sensing

INTRODUCTION

Electromagnetic metamaterials are kinds of synthetic structural materials with novel electromagnetic properties not found in nature [1]. Researchers have found very wide applications for the electromagnetic metamaterials in the fields of electromagnetism, optics, and materials sciences [1–4]. Specifically, the resonant frequency and strength of resonant-type electromagnetic metamaterials are strongly correlated with unit cell structural parameters and dielectric material properties of substrates, and those structural parameters and/or dielectric properties can be tuned by changing the environment physical and/or chemistry parameters. Therefore, new sensing technologies based on the resonant-type electromagnetic metamaterials can be developed [5–9]. For examples, the electromagnetic metamaterials can be widely used to sense as well as detect the changes of media parameters, pressure, humidity, temperature, and chemistry/biology molecules in the environments [10–12]. Comparing with the conventional sensing techniques,

the metamaterial-inspired sensing has the potential advantages including the high precision, label-free, safety, and can work properly in long-distance wireless situation. The explorations of sensing mechanism, sensing technology and device engineering based on the electromagnetic metamaterials are well-developed and its application methods in environmental sensing, chemical detection, biosensing and IoT emerging technologies are widely studied in recent years [13–18]. Previously reported review works have focused on the analysis of different sensing mechanisms, sensing methods, and wide application explorations [14–18]. However, the analysis on how to further improve the sensing performance is absent. Therefore, this mini review would like to summarize the recently reported high-precision sensing applications (especially the temperature sensing) based on the advanced high-performance resonant-type electromagnetic metamaterials.

RESEARCH PROGRESS

Overall Sensing Applications Analysis of Metamaterials

In the field of sensing applications based on the electromagnetic metamaterials, a variety of sensing technologies and design methods have been developed as mentioned above [5–13]. The sensing principle for most of the reported metamaterial-based sensors can be summarized as follows. At the resonant frequency of the electromagnetic metamaterial, a large number of electric field/magnetic field components are concentrated inside the basic unit of the electromagnetic metamaterial (meta-atom) and thus the macroscopic resonant frequency/strength characteristics of the electromagnetic metamaterial will follow the structural/material parameter changings inside the meta-atom. That means the characteristic changings of the dielectric material as well as the changes of surrounding environments will accordingly result in the changings of the resonant frequency or the resonant strength. Therefore, the external detection circuit and processing algorithm can be flexibly used to realize the changings monitoring of chemical/biological molecule types, gas concentrations, pressure, humidity and temperature. This sensing mechanism based on the metamaterials has many advantages compared to the conventional sensing techniques.

For examples, in the sensing fields of biology, chemistry, medicine, etc., traditional biosensors need to be labeled with fluorophores in the target. So the process is complicated, time consumed and expensive. Considering this problem, the researchers have developed different kinds of metamaterial-based sensors worked at optics [11, 12, 19], THz [20–26] and microwave [27–32], achieved groundbreaking realization methods and performances. Specifically, the refractive index of the medium around the meta-atom will be changed with the lesion level and chemical composition/concentration changings [33]. By detecting and analyzing the changes of the electromagnetic wave transmission/reflection amplitude at resonance or the resonant frequency caused by the corresponding refractive index changes, the lesion level and chemistry composition/concentration can be determined. In the field of

hazardous gas or chemical sensing applications, researchers have also designed hydrogen concentration detectors based on nanorod-structured electromagnetic metamaterials [11] and hazardous chemical concentration detectors based on metal split ring resonator (SRR) [34]. When the used metamaterial is exposed to the hydrogen or there are different kinds and/or concentrations of hazardous chemical materials at the split of the metal SRR, the transmission/reflection characteristics (resonant frequency or strength) of the electromagnetic metamaterial will be changed. As a result, the hydrogen can be detected and analyzed accordingly and the concentration characteristics of other hazardous chemical materials can be detected as well.

In addition, the resonant frequency/strength characteristics of the electromagnetic metamaterial are not only strongly related to the properties of the dielectric material surrounding the meta-atom, but also depended on the distance between the meta-atom and the substrate dielectric material. The relative position changes of the dielectric material around the meta-atom will result in the changes of equivalent refractive index near the meta-atom. Accordingly, the researchers designed microwave and/or THz bands pressure sensor based on the electromagnetic metamaterials [33, 35]. In the field of humidity sensing applications, the humidity changes of the medium around the meta-atom can also cause the changes of equivalent refractive index of the medium [36]. Thereby, determining the humidity is achieved by detecting the resonant frequency/strength of the electromagnetic metamaterial. For example, Romero in [37] proposed a wireless capacitive sensing tag loaded with a metamaterial unit in a single-layer design. The selected metamaterial structure is the conventional SRR, which allowed the tag to be miniaturized and the sensor to be highly sensitive.

Metamaterial-Based Temperature Sensing Technology

Among the various metamaterial-based sensing applications, the temperature sensing is one of the key researches and application fields for the electromagnetic metamaterials. This is because some of the used substrate materials and/or constructed sub-wavelength structures have high temperature sensitive property. According to the sensing mechanism of resonant-type metamaterial-inspired sensors mentioned above, the temperature sensitive dielectric substrate materials and the sub-wavelength nano/micro mechanical structure with thermal expansion coefficient differences will result in the changings of resonant frequency/strength under different temperatures [38–42].

Temperature Sensing Based on Temperature-Sensitive Dielectric Inspired Metamaterials

Generally, for the electromagnetic metamaterials formed on the temperature-sensitive dielectric substrate, the resonant frequency/strength is highly related to the equivalent dielectric constant varying of such substrate induced by temperature changing. Various temperature-sensitivity dielectric substrates can be used, such as the low-temperature co-fired ceramic (LTCC) substrate, sea water, barium titanate, lithium niobate, etc. For examples, in 2010, Varadan and Ji pioneered the

experimental studies for the resonant frequency/strength changing amounts of electromagnetic metamaterials based on the LTCC substrate due to the changings of the dielectric constant, electrical conductivity, and the thermal expansion of the medium during the temperature changes [43]. The results shown in this work indicated that the dielectric constant change has the main function (accounting for 84.03%).

In 2012, Ekmekci and Turhan-Sayan explored the temperature-sensing characteristics of SRR filling with sea water as the background medium [44]. For the proposed miniaturized metamaterial sensor prototype operating at X-band, a 158-MHz resonant frequency shift corresponds to a 20°C temperature change is achieved, leading to an average sensitivity level of 7.9 MHz/°C. In 2014, Zhang et al. used barium titanate (Ba0.5Sr0.5TiO3, BST) as a temperature-sensitive medium of the dielectric-type metamaterial and analyzed the temperature sensing mechanism [45]. An electric resonance characteristic with Lorentz-type dispersion of effective permittivity is seen around the resonant frequency. The relative permittivity of dielectric cut-wire is decreased with the increase in environmental temperature, hence, resulted in the blue shift of electric resonant frequency, with a calculated temperature sensitivity of 25 MHz/°C. In 2015, Karim et al. designed a closed-ring resonator (CRR) and a variety of open-ring resonators based on lithium niobate (LiNbO3) and compared their respective temperature sensitivity performances [46, 47]. This CRR structure-based sensor has a sensitivity up to 7.286 MHz/°C. At the same year, Zemouli et al. proposed a metamaterial sensor consisting of two concentric metallic rings and a thin metallic wire deposited on the surface of BaTiO$_3$ substrate and studied the variations of the resonant frequency according to the permittivity changing under varied temperatures [40].

In 2017, Karim et al. further designed an array of CRRs embedded in a multi-layer dielectric substrate [48]. A mixture of 70 vol% Boron Nitride (BN) and 30 vol% Barium Titanate (BTO) was used as the dielectric substrate. It was observed that for a temperature change from 23 to 200°C, the change in resonant frequency is 81.75 MHz, corresponding to a temperature sensitivity of 0.462 MHz/°C. At the same year, Qiu and Liu presented a thermally tunable Fano resonator obtained by asymmetrically coupling a conductive rubber-based H-shaped split ring resonator (SRR) and a copper C-shaped SRR coated on a Teflon fiberglass slab substrate [49]. At the Fano resonance, surface current distributions are anti-symmetric since the current excited in the H-shaped conductive rubber-based SRR and the C-shaped copper SRR are opposite and almost equal in magnitude. Consequently, the electrical and magnetic fields are canceled out, resulting in a high quality factor. Therefore, with the increase in temperature, the Fano resonant frequency was slightly shifted from 11 to 10.5 GHz, and the transmission loss gradually increased as well. For more details about the high quality factor metamaterials used in the high-performance temperature sensing area will be discussed in later.

In general, the temperature-sensing technology based on temperature-sensitive dielectric substrates has the advantages of miniaturization, high flexibility and simple preparation process. However, its dielectric constant changes with temperature

increase/decrease are in a very limited linear range. The inherent drawbacks such as low sensitivity and small dynamic range of this kind of metamaterial-based sensors will be limited for the practical application.

Temperature Sensing Based on the Thermal Expansion Coefficient Difference

Based the different thermal expansion coefficients of different substrates used in the metamaterials, the bending deformations due to the changes of background temperature will alter the equivalent capacitance/inductance parameters of the meta-atom, thereby causing the resonant frequency shift or resonance strength change. For examples, Thai et al. firstly loaded a cantilever arm at the open slot of the metal SRR as shown in **Figure 1A-i** [38, 50]. The arm consisted of two layers of heterogeneous materials with different thermal expansion coefficients. The upper layer was silicon with a smaller thermal expansion coefficient while the lower layer and the arm are all aluminum with larger thermal expansion coefficient. When the temperature is changed the cantilever will bend upwards or downwards, as a result affecting the equivalent capacitance value of the metal SRR. **Figures 1A-ii,iii** show the experimental transmission curve changes with different background temperatures, and a frequency shift of 800 MHz from 4.8 to 4.0 GHz can be seen.

Moreover, based the well-developed nano-fabrication process, temperature sensing and detection can be realized in the THz and optical frequency bands by constructing nano-scale MEMS metamaterial structures. For examples, in 2011, Ou et al. designed the nanoscale reconfigurable photonic metamaterials and the structure is shown in **Figure 1B-i** [51]. The Au-Si3N4-Au sandwich symmetrical structure shown in this figure has a very small deformation due to temperature change, while the two-layer structure composed of metal-semiconductor (Au-Si3N4) can show obviously deformation. The resonant properties of this system utterly depend on the coupling between neighboring bridges. For example, from **Figure 1B-ii** it can be seen that as the background temperature is increased, a dramatic increase of its transmission amplitude near its resonant frequency is achieved. Importantly, as the metamaterial structure was cooled back to its initial temperature these changes of its transmission spectrum were reversed.

In addition, Alves et al. constructed a MEMS temperature-sensing micro-mechanical arm on a semiconductor body and explored the temperature sensing technique in the terahertz band [29]. The sensor's absorbing element is designed with a resonant frequency that matches the source of the quantum cascade laser illumination. At the same time the semiconductor layer provides structural support, desired thermomechanical properties. As shown in **Figure 1C-i**, the absorbing element is connected to two Al/SiOx microcantilevers (legs), anchored to a silicon substrate, which acts as a heat sink, allowed the sensor to return to its undisturbed position when the excitation was stopped. **Figure 1C-ii** shows the experimental results for the temperature sensing properties, which indicates a sensitivity of 0.2 deg/°C.
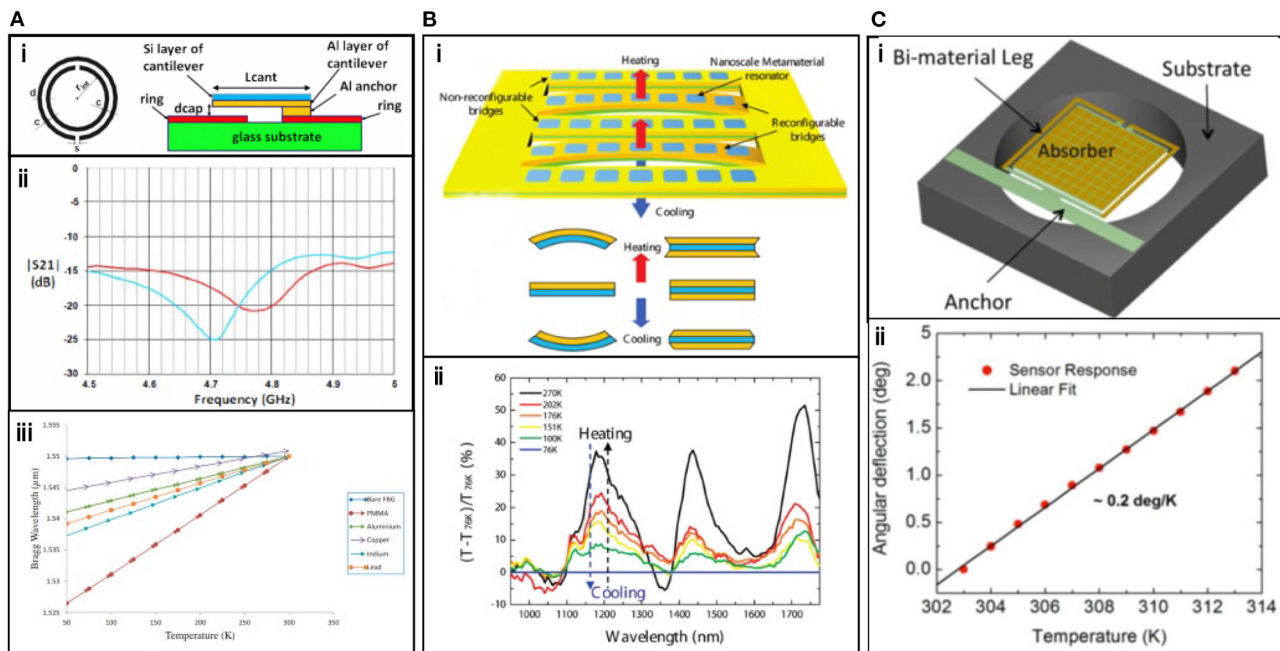
FIGURE 1 | Temperature sensitivity metamaterial units. **(A)** SRR on a cantilever arm, and the transmission spectra and resonant frequency response under different temperatures [38, 50], **(B)** nanoscale reconfigurable photonic metamaterials and the corresponding temperature changing performances [51], **(C)** Metamaterial absorber configuration fabricated on a microcantilevers and the accordingly temperature changing inspired structure deformation performance [29].

Generally speaking, the temperature sensing based on the difference in thermal expansion coefficient, especially for nano-scale MEMS micro-mechanical structure, mainly worked in the optical and THz frequency bands and had the advantages of reconfigurability, miniaturization and easy to integration. However, the shape deformation due to the difference in thermal expansion coefficient of heterogeneous composites is weak. And it also has complicated preparation process, high processing difficulty and high cost.

Sensitivity Enhancement Design of Electromagnetic Metamaterial Based Sensor

The above research progresses and results demonstrated the feasibility of electromagnetic metamaterials in the field of sensing application. However, the researchers did not thoroughly study the specific technical methods to optimize and improve the sensitivity and resolution of sensing. According to the resonance type sensing theory, high sensing sensitivity and resolution require the sensing unit's resonance quality factor and the FOM (FOM is defined as the ratio of the sensitivity to the resonance 3-dB bandwidth) to be as high as possible [52, 53]. A resonant-type sensor based on the meta-atom the has a large amount of electric field/magnetic field components accumulated inside the resonance unit (e.g., at the opening gap of the SRR) during resonance. Therefore, it is an effective way to further improve the sensitivity and resolution of the resonant-type sensors by

enhancing the electric field/magnetic field components of the electromagnetic metamaterial while effectively reducing the loss, to increase the resonant quality factor and improve the FOM of the sensor devices.

Based on the above suggestions, researchers have explored a variety of technical methods to improve the sensitivity of sensor, starting from the study of the resonance characteristics of new electromagnetic metamaterials. Firstly, the planar absorber composed of electromagnetic metamaterial can be equivalent to a Fabry-Perot cavity. The electric and magnetic field energy during resonance is well-bounded inside the cavity, and the radiation loss is small, resulting in the high resonant quality factor. Thus, the metamaterial absorbers can be used to improve sensing sensitivity and resolution for sensing application. For example, Cong et al. and Yahiaoui et al. studied the THz band single-frequency and multi-frequency metamaterial absorber based high-sensitivity sensors [25, 26], as shown in **Figure 2A-i**. It was observed from this figure that the FOM value of metamaterial absorber sensors have been found to be significantly higher than those of planar metamaterial resonators. The measured frequency shift of the sensors for different analyte thicknesses is shown in **Figure 2A-ii**. It was analyzed that the total frequency shift saturated at about 14.0%.

Moreover, Dong et al. achieved an electromagnetic-induced transparency (EIT) resonance characteristics based on the interaction between different electromagnetic metamaterial units and incident electromagnetic waves [54]. They used the three-bar
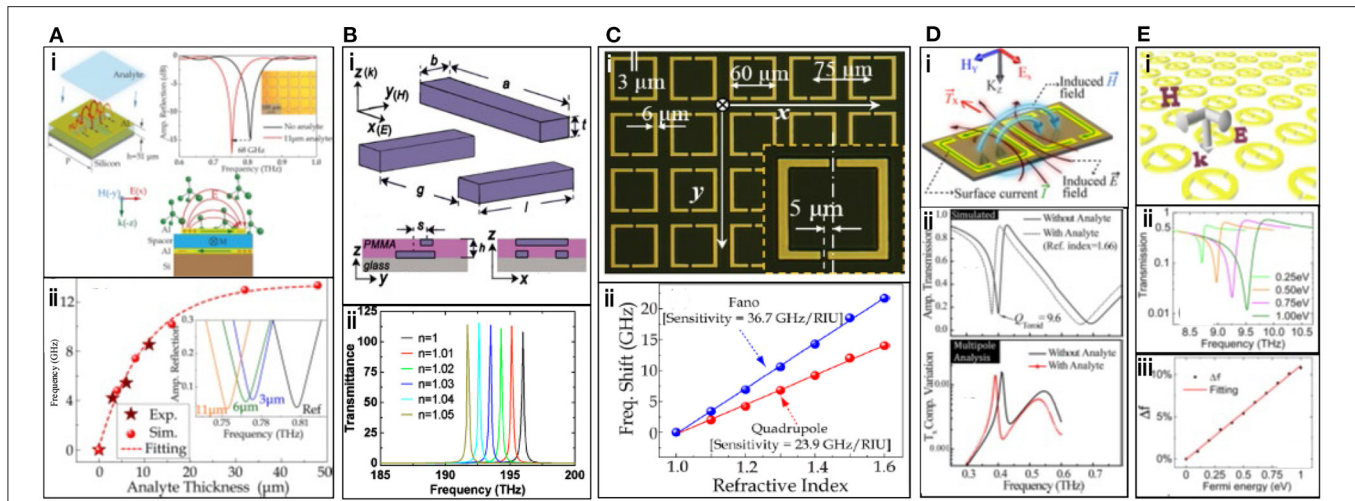
FIGURE 2 | Performance enhanced metamaterial unit based sensors. **(A)** CSA and CCSA based Fabry-Perot cavity type sensors and the sensing performance [25, 26], **(B)** schematic illustration of EIT-like metamaterial unit and the enhanced narrow transparency windows at different refraction indexes [54], **(C)** microscopic image of the terahertz asymmetric Fano resonances shift with the change in refractive indexes [24], **(D)** operating mechanism for the toroidal resonance and the corresponding resonance changing performance [55], and **(E)** schematic illustration for the newly developed graphene-inspired anapole resonator and the accordingly resonance changings under different Femi levels [56].

configuration to investigate the active plasmon analog of the EIT in order to improve the performance of the refractive-index fluctuation sensing of the surrounding medium which can be seen in **Figure 2B-i**. The result shown in this work (e.g., **Figure 2B-ii**) is higher than the traditional metamaterial resonance unit, which can be used to improve sensing sensitivity and resolution.

On another hand, Singh et al. broke the basic electromagnetic metamaterial unit structure and proposed a new Fano asymmetric resonance which can be seen in **Figure 2C-i** [24]. From that method they were able to achieve sensitivity levels of 7.75×10^3 nm/refractive index unit (RIU) for quadrupole and 5.7×10^4 nm/RIU with the Fano resonance. The sensitivity of Fano resonance gets enhanced due to much stronger interaction of analyte layer with the enhanced electric field in the capacitive gaps as shown in **Figure 2C-ii**. Semouchkina et al. also applied a full-scale electromagnetic metamaterial in a parallel version of the metal waveguide to achieve an ultra-high-Q Fano resonance characteristic, and explored the design method of a high-sensitivity sensor [57]. In addition, in 2016, Campione et al. presented a new approach that relies on a single resonator and produces robust, high quality-factor Fano resonance, by breaking the highly symmetric resonator geometries, such as cubes, to induce couplings between the orthogonal resonance modes. In particular, they designed perturbations that couple "bright" dipole modes to "dark" dipole modes whose radiative decay is suppressed by local field effects, achieving a quality-factor of ~600 [58].

For those proposed high quality-factor metamaterials, it can be used very easily in the high-precision temperature sensing area if those meta-atoms are designed on the temperature sensitivity substrates or the meta-atom is composed directly by the temperature sensitivity metals.

DISCUSSION AND PERSPECTIVE

Based on the performance enhanced sensing designs by using the asymmetric high quality-factor resonance mode, in the past several years, researchers further proposed other kinds of high quality-factor metamaterial units for sensing applications, including the toroidal resonance [55, 59–61], anapole resonance [56, 62–67], and enhanced magnetic plasmon resonance [68–74]. For examples, by placing the period symmetric arrangement of the Fano resonator shown in **Figure 2C-i** as the mirror symmetric arrangement shown in **Figure 2D**, one can get the toroidal resonance with quality factor larger than the regular Lorentz resonance [63]. By concentrating the electric and magnetic field within the resonator of the new kind of anapole resonator shown in **Figure 2E**, the sensing resolution can be further enhanced as anticipated [67].

CONCLUSION

In summary, the sensing based on the electromagnetic metamaterials has developed rapidly in terms of sensing mechanism and implementation methods. Especially in the field of temperature sensing area, a variety of resonant-type temperature sensing technologies and many achievements have emerged in the past years, and researches and explorations have been carried out for further optimization and improvement of sensing sensitivity and resolution. Most of the existing temperature-sensing technologies based on temperature-sensitive dielectric materials, thermal expansion coefficient difference, and nano-scale MEMS structure are all derived from the dielectric constant, material shape, mechanical structure, etc. The sensing sensitivity improvement technologies based on high-quality-factor electromagnetic metamaterials are explored.

AUTHOR CONTRIBUTIONS

FUNDING

REFERENCES

1. Cui TJ, Smith DR, Liu R. *Metamaterials: Theory, Design and Applications*. New York, NY: Spring-Verlag (2010).

2. Xu HX, Ma S, Luo W, Cai T, Sun S, He Q, et al. Aberration-free and functionality-switchable meta-lenses based on tunable metasurfaces. *Appl Phys Lett.* (2016) 109:193506. doi: 10.1063/1.4967438

3. Xu HX, Sun S, Tang S, Ma S, He Q, Wang GM, et al. Dynamical control on helicity of electromagnetic waves by tunable metasurfaces. *Sci Rep.* (2016) 6:1–10. doi: 10.1038/srep27503

4. Ren X, Das R, Tran P, Ngo TD, Xie YM, Auxetic metamaterials and structures: a review. *Smart Mat Struct.* (2018) 27:023001. doi: 10.1088/1361-665X/aaa61c

5. Ishimaru A, Jaruwatanadilok S, Kuga Y. Generalized surface plasmon resonance sensors using metamaterials and negative index materials. *Prog Electromag Res.* (2005) 51:139–52. doi: 10.2528/PIER04020603

6. Driscoll T, Andreev GO, Basov DN, Palit S, Cho SY, Jokerst NM, et al. Tuned permeability in terahertz split-ring resonators for devices and sensors. *Appl Phys Lett.* (2007) 91:062511. doi: 10.1063/1.2768300

7. Al-Naib IAI, Jansen C, Koch M. Thin-film sensing with planar asymmetric metamaterial resonators. *Appl Phys Lett.* (2008) 93:083507. doi: 10.1063/1.2976636

8. Cubukcu E, Zhang S, Park YS, Bartal G, Zhang X. Split ring resonator sensors for infrared detection of single molecular monolayers. *Appl Phys Lett.* (2009) 95:043113. doi: 10.1063/1.3194154

9. Papasimakis N, Luo Z, Shen ZX, De Angelis F, Di Fabrizio E, Nikolaenko AE, et al. Graphene in a photonic metamaterial. *Optics Express.* (2010) 18:8353–9. doi: 10.1364/OE.18.008353

10. Withayachumnankul W, Jaruwongrungsee K, Fumeaux C, Abbott D. Metamaterial-inspired multichannel thin-film sensor. *IEEE Sensors.* (2012) 12:1455–8. doi: 10.1109/JSEN.2011.2173762

11. Lee HJ, Lee JH, Moon HS, Jang IS, Choi JS, Yook JG, et al. A planar split-ring resonator-based microwave biosensor for label-free detection of biomolecules. *Sens Actuators B Chem.* (2012) 169:26–31. doi: 10.1016/j.snb.2012.01.044

12. Nasir ME, Dickson W, Wurtz GA, Wardley WP, Zayats AV. Hydrogen detected by the naked eye: optical hydrogen gas sensors based on core/shell plasmonic nanorod metamaterials. *Adv Mater.* (2014) 26:3532–7. doi: 10.1002/adma.201305958

13. Xu X, Peng B, Li D, Zhang J, Wong LM, Zhang Q, et al. Flexible visible–infrared metamaterials and their applications in highly sensitive chemical and biological sensing. *Nano Lett.* (2011) 11:3232–8. doi: 10.1021/nl2014982

14. Xu W, Xie L, Ying Y. Mechanisms and applications of terahertz metamaterial sensing: a review. *Nanoscale.* (2017) 9:13864–78. doi: 10.1039/C7NR03824K

15. Salim A, Lim S. Review of recent metamaterial microfluidic sensors. *Sensors.* (2018) 18:232. doi: 10.3390/s18010232

16. Yoo SJ, Park QH. Metamaterials and chiral sensing: a review of fundamentals and applications. *Nanophotonics.* (2019) 8: 249–61. doi: 10.1515/nanoph-2018-0167

17. Vivek A, Shambavi K, Alex Z C. A review: metamaterial sensors for material characterization. *Sensor Rev.* (2019) 39:417–32. doi: 10.1108/SR-06-2018-0152

18. Bogue R. Sensing with metamaterials: a review of recent developments. *Sensor Rev.* (2017) 37:305–11. doi: 10.1108/SR-12-2016-0281

19. Kabashin AV, Evans P, Pastkovsky S, Hendren W, Wurtz GA, Atkinson R, et al. Plasmonic nanorod metamaterials for biosensing. *Nat.* (2009) 8:867–71. doi: 10.1038/nmat2546

20. Wu X, Pan X, Quan B, Xu X, Gu C, Wang L. Self-referenced sensing based on terahertz metamaterial for aqueous solutions. *Appl Phys Lett.* (2013) 102:151109. doi: 10.1063/1.4802236

21. Drexler C, Shishkanova TV, Lange C, Danilov SN, Weiss D, Ganichev SD, et al. Terahertz split-ring metamaterials as transducers for chemical sensors based on conducting polymers: a feasibility study with sensing of acidic and basic gases using polyaniline chemosensitive layer. *Microchim Acta.* (2014) 181:1857–62. doi: 10.1007/s00604-014-1263-0

22. Cheng Y, Mao XS, Wu C, Wu L, Gong R. Infrared non-planar plasmonic perfect absorber for enhanced sensitive refractive index sensing. *Opt Mater.* (2016) 53:195–200. doi: 10.1016/j.optmat.2016.01.053

23. Li J, Shah CM, Withayachumnankul W, Ung BS-Y, Mitchell A, Sriram S, et al. Flexible terahertz metamaterials for dual-axis strain sensing. *Opt Lett.* (2013) 38:2104–6. doi: 10.1364/OL.38.002104

24. Singh R, Cao W, Al-Naib I, Cong L, Withayachumnankul W, Zhang W. Ultrasensitive terahertz sensing with high-Q Fano resonances in metasurfaces. *Appl Phys Lett.* (2014) 105:171101. doi: 10.1063/1.4895595

25. Cong L, Tan S, Yahiaoui R, Yan F, Zhang W, Singh R. Experimental demonstration of ultrasensitive sensing with terahertz metamaterial absorbers: a comparison with the metasurfaces. *Appl Phys Lett.* (2015) 106:31107. doi: 10.1063/1.4906109

26. Yahiaoui R, Tan S, Cong L, Singh R, Yan F, Zhang W. Multispectral terahertz sensing with highly flexible ultrathin metamaterial absorber. *J Appl Phys.* (2015) 118:83103. doi: 10.1063/1.4929449

27. Alahnomi RA, Zakaria Z, Ruslan E, Ab Rashid SR, Mohd Bahar AA. High-Q sensor based on symmetrical split ring resonator with spurlines for solids material detection. *IEEE Sens J.* (2017) 17:2766–75. doi: 10.1109/JSEN.2017.2682266

28. Tao H, Kadlec EA, Strikwerda AC, Fan K, Padilla WJ, Averitt RD, et al. Microwave and terahertz wave sensing with metamaterials. *Opt Express.* (2011) 19:21620–6. doi: 10.1364/OE.19.021620

29. Alves F, Grbovic D, Kearney B, Karunasiri G. High sensitivity metamaterial based bi-material terahertz sensor. *Terahertz RF Millimeter Submillimeter Wave Technol Appl VI.* (2013) 8624:862411. doi: 10.1117/12.2005272

30. Melik R, Unal E, Kosku Perkgoz N, Puttlitz C, Demir HV. Flexible metamaterials for wireless strain sensing. *Appl Phys Lett.* (2009) 95:3–5. doi: 10.1063/1.3250175

31. Penirschke A, Schussler M, Jakoby R. New microwave flow sensor based on a left-handed transmission line resonator. In: *2007 IEEE/MTT-S International Microwave Symposium* (Honolulu, HI). (2007). p. 393–6.

32. Xu K, Liu Y, Chen S, Zhao P, Peng L, Dong L, et al. Novel microwave sensors based on split ring resonators for measuring permittivity. *IEEE Access.* (2018) 6:26111–20. doi: 10.1109/ACCESS.2018.2834726

33. Liu Y, Zhan S, Cao G, Li J, Yang H, Liu Q, et al. Theoretical design of plasmonic refractive index sensor based on the fixed band detection. *IEEE J Sel Top Quantum Electron.* (2018) 25:4600206. doi: 10.1109/JSTQE.2018. 2827661

34. Rawat V, Kitture R, Kumari D, Rajesh H, Banerjee S, Kale SN. Hazardous materials sensing: an electrical metamaterial approach. *J Magn Magn Mater.* (2016) 415:77–81. doi: 10.1016/j.jmmm.2015.11.023

35. Melik R, Unal E, Perkgoz N, Santoni B, Kamstock D, Puttlitz C, et al. Nested metamaterials for wireless strain sensing. *IEEE J Sel Top Quantum Electron.* (2010) 16:450–8. doi: 10.1109/JSTQE.2009.2033391

36. Kim H S, Cha S H, Roy B, Kim S, Ahn YH. Humidity sensing using THz metamaterial with silk protein fibroin. *Opt Express.* (2018) 26:33575–81. doi: 10.1364/OE.26.033575

37. Romero RA, Feitoza RS, Rambo CR, Sousa FR. A low-cost passive wireless capacitive sensing tag based on split-ring resonator. *IEEE International Instrumentation and Measurement Technology Conference (I2MTC) Proceedings* (Pisa). (2015), 434–9. doi: 10.1109/I2MTC.2015. 7151307

38. Thai TT, Mehdi JM, Aubert H, Pons P, DeJean GR, Tentzeris MM, et al. A novel passive wireless ultrasensitive RF temperature transducer for remote sensing. In: *2010 IEEE MTT-S International Microwave Symposium* (Anaheim, CA). (2010). p. 473–6.

39. Li J, Gai L, Li H, Hu H. A high sensitivity temperature sensor based on packaged microfibre knot resonator. *Sens Actuators A Phys.* (2017) 263:369–72. doi: 10.1016/j.sna.2017.06.031

40. Zemouli S, Chaabi A, Talbi HS. Design of a compact and high sensitivity temperature sensor using metamaterial. *Int J Antennas Propag.* (2015) 2015:301358. doi: 10.1155/2015/301358

41. Liu M, Hwang HY, Tao H, Strikwerda AC, Fan K, Keiser GR, et al. Terahertz-field-induced insulator-to-metal transition in vanadium dioxide metamaterial. *Nature.* (2012) 487:345–8. doi: 10.1038/nature11231

42. Lv TT, Li YX, Ma HF, Zhu Z, Li ZP, Guan CY, et al. Hybrid metamaterial switching for manipulating chirality based on VO 2 phase transition. *Sci Rep.* (2016) 6:1–9. doi: 10.1038/srep23186

43. Varadan V, Ji L. Temperature dependence of resonances in metamaterials. *IEEE Trans Microw Theory Tech.* (2010) 58:2673–81. doi: 10.1109/TMTT.2010.2065910

44. Ekmekci E, Turhan-Sayan G. Multi-functional metamaterial sensor based on a broad-side coupled SRR topology with a multi-layer substrate. *Appl Phys A.* (2013) 110:189–97. doi: 10.1007/s00339-012-7113-1

45. Zhang F, Chen L, Wang Y, Zhao Q, He X, Chen K. Thermally tunable electric mie resonance of dielectric cut-wire type metamaterial. *Opt Express.* (2014) 22:24908. doi: 10.1364/OE.22.024908

46. Karim H, Shuvo MAI, Delfin D, Lin Y, Choudhuri A, Rumpf RC. Development of metamaterial based low cost passive wireless temperature sensor. *SPIE Sens Smart Struct Technol Civil Mech Aerospace Syst.* (2014) 9061:662–70. doi: 10.1117/12.2045242

47. Kairm H, Delfin D, Shuvo MAI, Chavez LA, Garcia CR, Barton JH, et al. Concept and model of a metamaterial-based passive wireless temperature sensor for harsh environment applications. *IEEE Sens J.* (2015) 15:1445–52. doi: 10.1109/JSEN.2014.2363095

48. Karim H, Delfin D, Chavez LA, Delfin L, Martinez R, Avila J, et al. Metamaterial based passive wireless temperature sensor. *Adv Eng Mater.* (2017) 19:1600741. doi: 10.1002/adem.201600741

49. Qiu K, Liu Z. Thermally tunable fano resonance of a conductive rubber-based metamaterial. *Microw Opt Technol Lett.* (2017) 59:2960–4. doi: 10.1002/mop.30867

50. Thai TT, Chebila F, Mehdi JM, Pons P, Aubert H, DeJean GR, et al. Design and development of a millimetre-wave novel passive ultrasensitive temperature transducer for remote sensing and identification. In: *The 40th European Microwave Conference* (Paris). (2010). p. 45–8.

51. Ou JY, Plum E, Jiang L, Zheludev NI. Reconfigurable photonic metamaterials. *Nano Lett.* (2011) 11:2142–4. doi: 10.1021/nl200791r

52. Yang S, Tang C, Liu Z, Wang B, Wang C, Li J, et al. Simultaneous excitation of extremely high-Q-factor trapped and octupolar modes in terahertz

53. Du L-H, Li J, Liu Q, Zhao J-H, Zhu L-G. High-Q Fano-like resonance based on a symmetric dimer structure and its terahertz sensing application. *Opt Mater Express.* (2017) 7:1335–42. doi: 10.1364/OME.7. 001335

54. Dong Z-G, Liu H, Cao J-X, Li T, Wang S-M, Zhu S-N, et al. Enhanced sensing performance by the plasmonic analog of electromagnetically induced transparency in active metamaterials. *Appl Phys Lett.* (2010) 97:114101. doi: 10.1063/1.3488020

55. Gupta M, Srivastava YK, Manjappa M, Singh R. Sensing with toroidal metamaterial. *Appl Phys Lett.* (2017) 110:121108. doi: 10.1063/1. 4978672

56. Algorri JF, Zografopoulos DC, Ferraro A, García-Cámara B, Vergaz R, Beccherelli R, et al. Anapole modes in hollow nanocuboid dielectric metasurfaces for refractometric sensing. *Nanomaterials.* (2019) 9:30. doi: 10.3390/nano9010030

57. Semouchkina E, Duan R, Semouchkin G, Pandey R. Sensing based on Fano-type resonance response of all-dielectric metamaterials. *Sensors.* (2015) 15:9344–59. doi: 10.3390/s150409344

58. Campione S, Liu S, Basilio LI, Warne LK, Langston WL, Luk TS, et al. Broken symmetry dielectric resonators for high quality factor Fano metasurfaces. *ACS Photonics.* (2016) 3:2362–7. doi: 10.1021/acsphotonics. 6b00556

59. Kaelberer T, Fedotov VA, Papasimakis N, Tsai DP, Zheludev NI. Toroidal dipolar response in a metamaterial. *Science.* (2010) 330:1510–2. doi: 10.1126/science.1197172

60. Liu Z, Du S, Cui A, Li Z, Fan Y, Chen S, et al. High-quality-factor mid-infrared toroidal excitation in folded 3D metamaterials. *Adv Mater.* (2017) 29:1606298. doi: 10.1002/adma.201606298

61. Ma L, Chen D, Zheng W, Li J, Wang W, Liu Y, et al. Thermally tunable high-Q metamaterial and sensing application based on liquid metals. *Optics Express.* (2021) 29:6069–79. doi: 10.1364/OE.418024

62. Evlyukhin AB, Yu YF, Bakker RM, Chipouline A, Kuznetsov AI, Luk'yanchuk B, et al. Nonradiating anapole modes in dielectric nanoparticles. *Nat Commun.* (2015) 6:8069. doi: 10.1038/ncomms 9069

63. Basharin AA, Chuguevsky V, Volsky N, Kafesaki M, Economou EN. Extremely high Q-factor metamaterials due to anapole excitation. *Phys Rev B.* (2017) 95:035104. doi: 10.1103/PhysRevB.95. 035104

64. Wu PC, Liao CY, Savinov V, Chung TL, Chen WT, Huang YW, et al. Optical anapole metamaterial. *ACS Nano.* (2018) 12:1920–7. doi: 10.1021/acsnano.7b08828

65. Savinov V, Papasimakis N, Tsai DP, Zheludev NI. Optical anapoles. *Commun Phys.* (2019) 2:69. doi: 10.5258/SOTON/D0914

66. Sabri L, Huang Q, Liu JN, Cunningham BT. Design of anapole mode electromagnetic field enhancement structures for biosensing applications. *Optics Express.* (2019) 27:7196–212. doi: 10.1364/OE.27. 007196

67. Liu X, Liu Z, Hua M, Wang L, Wang K, Zhang W, et al. Tunable terahertz metamaterials based on anapole excitation with graphene for reconfigurable sensors. *ACS Appl Nano Mater.* (2020) 3:2129–33. doi: 10.1021/acsanm.0c00141

68. Chen J, Nie H, Zha T, Mao P, Tang C, Shen X, et al. Optical magnetic field enhancement by strong coupling in metamaterials. *J Lightwave Technol.* (2018) 36:2791–5. doi: 10.1364/JLT.36. 002791

69. Chen J, Nie H, Peng C, Qi S, Tang C, Zhang Y, et al. Enhancing the magnetic plasmon resonance of three-dimensional optical metamaterials *via* strong coupling for high-sensitivity sensing. *J Lightwave Technol.* (2018) 36:3481–5. doi: 10.1109/JLT.2018.2846019

70. Chen J, Nie H, Tang C, Cui Y, Yan B, Zhang Z, et al. Highly sensitive refractive-index sensor based on strong magnetic resonance in metamaterials. *Appl Phys Express.* (2019) 12:052015. doi: 10.7567/1882-0786/ab14fa

71. Chen J, Qi S, Hong X, Gu P, Wei R, Tang C, et al. Highly sensitive 3D metamaterial sensor based on diffraction coupling of magnetic

plasmon resonances. *Results Phys.* (2019) 15:102791. doi: 10.1016/j.rinp.2019.
102791

72. Chen J, Peng C, Qi S, Zhang Q, Tang C, Shen X, et al. Photonic microcavity-enhanced magnetic plasmon resonance of metamaterials for sensing applications. *IEEE Photonics Technol Lett.* (2018) 31:113–6. doi: 10.1109/LPT.2018.2881989

73. Chen J, Chen S, Gu P, Yan Z, Tang C, Xu Z, et al. Electrically modulating and switching infrared absorption of monolayer graphene in metamaterials. *Carbon.* (2020) 162:187–94. doi: 10.1016/j.carbon.2020. 02.032

74. Chen J, Yang C, Gu P, Kuang Y, Tang C, Chen S, et al. High sensing properties of magnetic plasmon resonance by strong coupling in three-dimensional metamaterials. *J Lightwave Technol.* (2021) 39:562–5. doi: 10.1109/JLT.2020. 3033971

Reconfigurable THz Metamaterial Filter Based on Binary Response for Information Processing System

Eistiak Ahamed[1], Ahmed Mahfuz Tamim[1], Mohammad Rashed Iqbal Faruque[1]*, Rasheduzzaman Sifat[1] and Mohammad Tariqul Islam[2]

[1] Space Science Center (ANGKASA), Universiti Kebangsaan Malaysia, Bangi, Malaysia, [2] Department of Electrical, Electronic and Systems Engineering, Universiti Kebangsaan Malaysia, Bangi, Malaysia

Light-matter interactions between the metallic and dielectric layers along with the controlling of electromagnetic waves can create a way to develop micro-devices and moderate the functionalities for advanced applications. This study describes a new controlling technique of the plasmatic electron packet based on an electric split-ring resonator (eSRR). All numerical experiments were performed using an advanced CST electromagnetic package. The proposed metamaterial tunneled structure in this study operates using terahertz (THz) frequency spectrum as an efficient digital processing filter. The array combination of the tunneled structure consisted of three individual unit cells. Moreover, the two engineered metallic arms added to the tunneled structure exhibited two peak resonances and one passband frequency region. A large evanescent field was produced to enhance the wave-metal interactions with the presence of a metal-dielectric micro-tunnel. The intensity of the electromagnetic wave-metal interactions was encoded to binary 0 and 1 for information encoding purposes. As a result, the reconfigurable micro-unit cell metamaterial tunneled structure was able to effectively control the electric field and allow electron packets to be digitally encoded for the information processing system.

Keywords: electric split-ring resonator, digital filter, micro-structured tunnel, reconfigurable, THz

INTRODUCTION

Materials with special characteristics like negative permittivity together with negative permeability cannot be found in nature. Thus, engineers or researchers sought to develop artificial materials of different structures exhibiting negative permittivity and negative permeability at a time within a certain frequency spectrum. Such artificial materials are known as metamaterials [1, 2]. One exotic phenomenon of metamaterial is that they can greatly impact the propagation of electromagnetic waves with a superior ability to control the electromagnetic waves as their subwavelength periodic meta-atom unit cell can be designed and optimized for desired applications. In previous works, light-matter interactions in microstructures were optimized to produce non-typical electromagnetic responses. With this in mind, negative electrical permittivity and negative magnetic permeability are included and examined to minimize the gap between basic micro-science and micro-devices [3] alongside the dynamic functionalities of the micro-devices. Metamaterials that can be actively controlled are utilized for numerous applications like controlling the propagation of the electromagnetic wave, analogue computing, [4, 5] etc. Recent studies focus

more on the orbital angular momentum (OAM) of planar metamaterial and metasurfaces [6, 7]. For instance, in an optical transmission system, the OAM of light can be used for multiplexing and to increase the power of the system.

The developmental increase of coded, programmable, and digital metamaterial concepts represent the beginning of a new age in the field of information technology [8–10]. Metamaterials incorporated in digital applications have different exotic characteristics such as beam manipulation [11], broadband diffusion [12], controlling of electromagnetic waves [13], vibration controlling [14], etc. In 2014, Giovampaola and Engheta [15] presented a digital metamaterial concept by constructing metamaterial bytes using spatial mixtures of digital metamaterial bits. The digital metamaterial bits were particles of the materials which indicate explicit material properties of the positive permittivity layer of Silicon (Si) and negative permittivity layer of Silver (Ag). In the following year, a coding metamaterial was developed by Cui et al. [8] for the manipulation of the reflection, scattering, and diffusion of waves in the microwave spectrum. They presented two types of unit cells with 0 and π phases which they named as 0 and 1. They then extended the work from 1-bit coding to 2-bit coding metamaterial. Additionally, Shen et al. [16] presented an integrated Si-based digital metamaterial exhibiting

unidirectional energy flow. They also utilized integrated digital metamaterial to develop an optical diode. Furthermore, Shen et al. [17] developed a coding metasurface for beamforming applications based on transmission whereby the transmitted field patterns depended upon the metamaterial bits of the particular meta-atom structure. Meanwhile, Gao et al. [12] presented a coded Minkowski closed-loop structured unit cell to produce several bits on different geometrical scales to control terahertz (THz) radiation.

Moreover, many studies reported numerous micro-electro-mechanical-system (MEMS) based metamaterial and metasurface structures for numerous applications [18–22]. Ma et al. [18] developed polarization-sensitive MEMS-based tunable metamaterials for the terahertz spectrum. The proposed metamaterial structures used curved cantilevers of electric split-ring resonators based on deformable MEMS. In 2014, Han et al. [19] developed a MEMS-based reconfigurable filter and modulator. Low loss and high transparent substrate Quartz was used as a substrate. At 480 GHz, the system manifested a high contrast switching efficiency of 16.5 dB. Meanwhile, Bilgin et al. [20] developed a MEMS-based THz detector which was characterized to extract its mechanical performance in 2015. The detector had a pixel size of $200 \times 200\,\mu m$, working between 1 and 5 THz bands. Arbabi et al. [21] in 2018, developed a
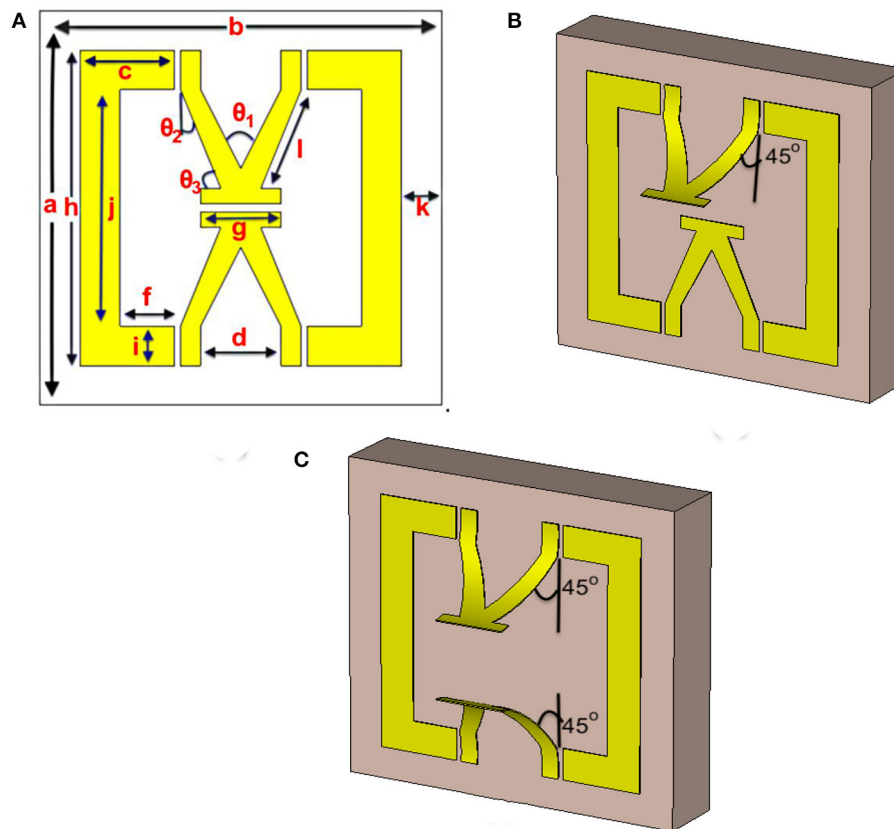

FIGURE 1 | Proposed metamaterial **(A)** C-V unit cell, **(B)** V one arm bend, and **(C)** V two-arm bend structures.

MEMS-based tunable dielectric metasurface lens. The lens was made of MEMS and has an optical power shift of more than 4% per 1 μm movement of the metasurface. In 2020, Huang et al. [22] developed an actively tunable THz filter based on MEMS metamaterial. Due to the advantage in optical applications, electromagnetically induced transparency (EIT) analogues in classical oscillator systems were also discussed. As a functional filter, the metamaterial regulated EIT activity to regulate waves around 1.832 THz.

This study introduces a new reconfigurable metamaterial microstructure that works as a digital filter and is capable of performing bit sequencing conversion in the THz frequency spectrum. The micro-unit cell structure exhibited two transmission resonances an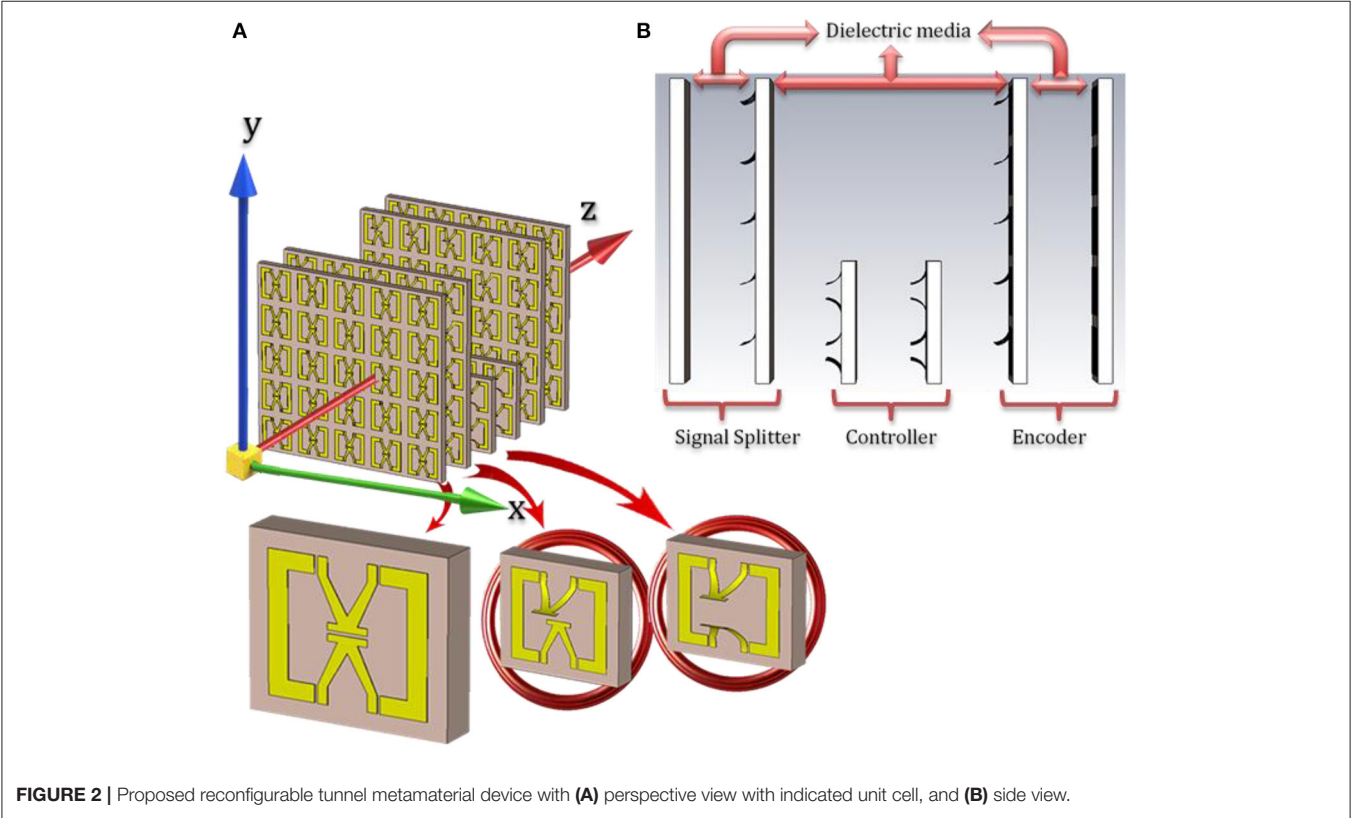d one special passband resonance. A special tunneled arrangement is also presented and numerically explained by digital binary output. Moreover, the basic unit cell is defined as the digital metamaterial by addressing the dielectric substrate as "0" and the metallic resonator as "1." Appropriate tunnel sequencing which was designed and explained can manipulate the electromagnetic waves and convert propagating waves to binary output through a digital metamaterial filter.

STRUCTURE OF MICRO METAMATERIAL DEVICE

Figure 1A illustrates the geometry of the metamaterial structure. Its unit cells are composed of corrugated metal strips labeled C to V (C-V) in alphabetical order and periodically arrayed in the x- and y-directions. The C and V strips create horizontal and vertical mirror images, respectively. **Figures 1A–C** present the proposed and modified C-V structures. Whereby, **Figures 1B,C** represent the reconfigurable designs of the C-V structure. which are based on **Figure 1A** [10]. **Figure 1B** displays one arm of V strips that was freed, while **Figure 1C** depicts two arms that were freed from the dielectric interface. On the other hand, lossy metal aluminium utilized in this study possesses an electric conductivity of 3.56 × 10,007 S/m, thermal conductivity of 237 W/k/m and Young's modulus of 69 GPa. The success of aluminium nano-particles in the field of nanoscience and nanotechnology is therefore attributed to their desirable properties. They are non-magnetic, light and non-sparking.

TABLE 1 | Geometric parameters of the proposed metamaterial microstructure.

Parameters	Dimensions (μm)	Parameters	Dimensions (μm)
a	10.00	i	1.00
b	10.00	j	6.00
c	2.35	k	2.00
d	2.00	l	2.69
e	0.15	θ_1	45°
f	1.35	θ_2	30°
g	2.00	θ_3	60°
h	8.00		

FIGURE 2 | Proposed reconfigurable tunnel metamaterial device with **(A)** perspective view with indicated unit cell, and **(B)** side view.

Also, since they are high in the scale of malleability, they are commonly used in many industrial applications requiring a solid, lightweight and easily constructible material.

Figure 1 and **Table 1** depict the geometrical parameters of the unit cell. The symbols "a" and "b" denote the substrate length and width, respectively. Meanwhile, symbol "e" represents the gap distance between strips C and V, "h" indicates the length of part C, "c" is the width of the two legs in part C, "d" is the gap between the legs of part V, "I" is the metal width of leg C, "j" is the vertical length of strip C, "g" and "l" are the base width and slope of strip V alongside "k" which is the distance between the metal arm and substrate edge. The angles between the two legs of strip V on the bottom inner side, the outer side of the head of strip V, and the bottom outer side of strip V were $\theta_1 = 45°$, $\theta_2 = 30°$, and $\theta_3 = 60°$, respectively. Moreover, the arms of strip V are bent at a 45° angle from the dielectric-metal interface as depicted in **Figures 1B,C**.

Recently, the use of filters in processing optical information has gained the interest of many researchers. Analogous data sets can be encoded for optical communication based on their amplitude, phase, intensity, wavelength, or polarization [23, 24]. Based on these properties, a three-unit cell was designed to create an array to serve as an individual unit cell. The array plates were also used to arrange a parallel sequence to achieve binary information of the proposed micro reconfigurable metamaterial device. Furthermore, the proposed device consisted of four
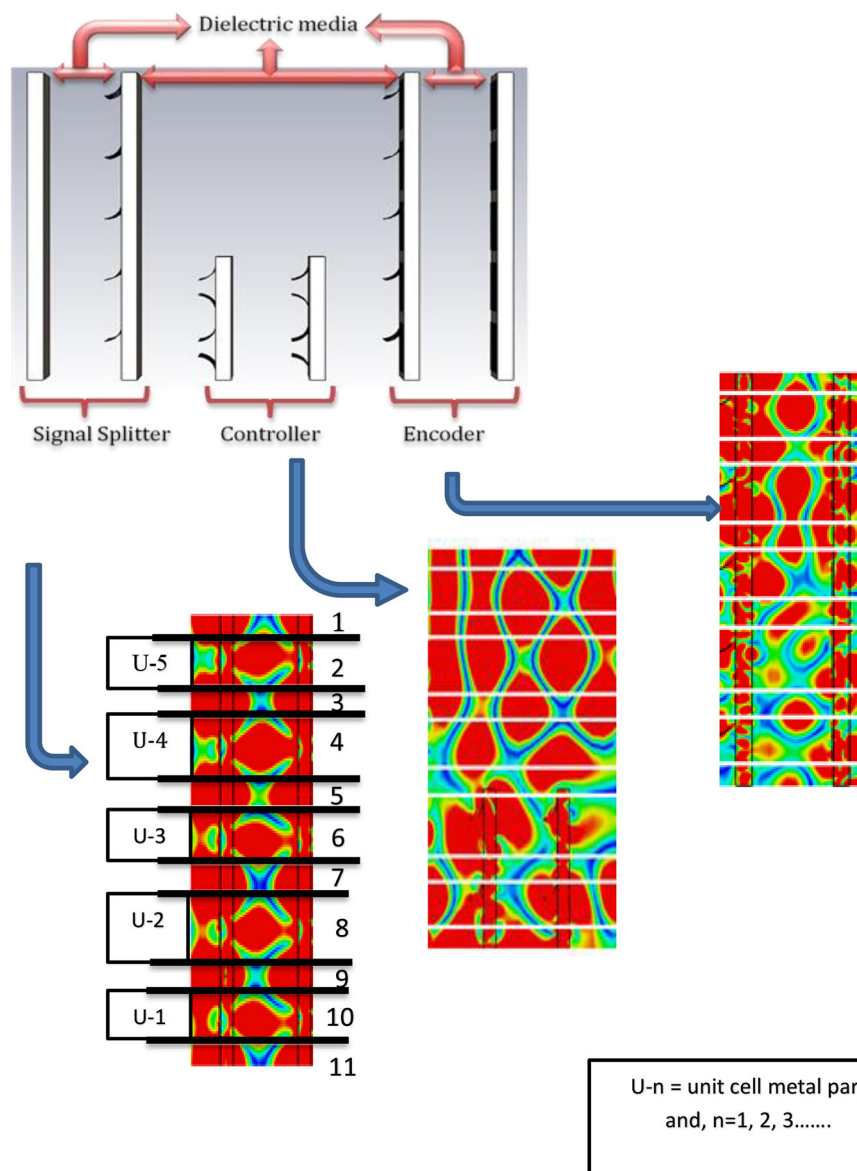

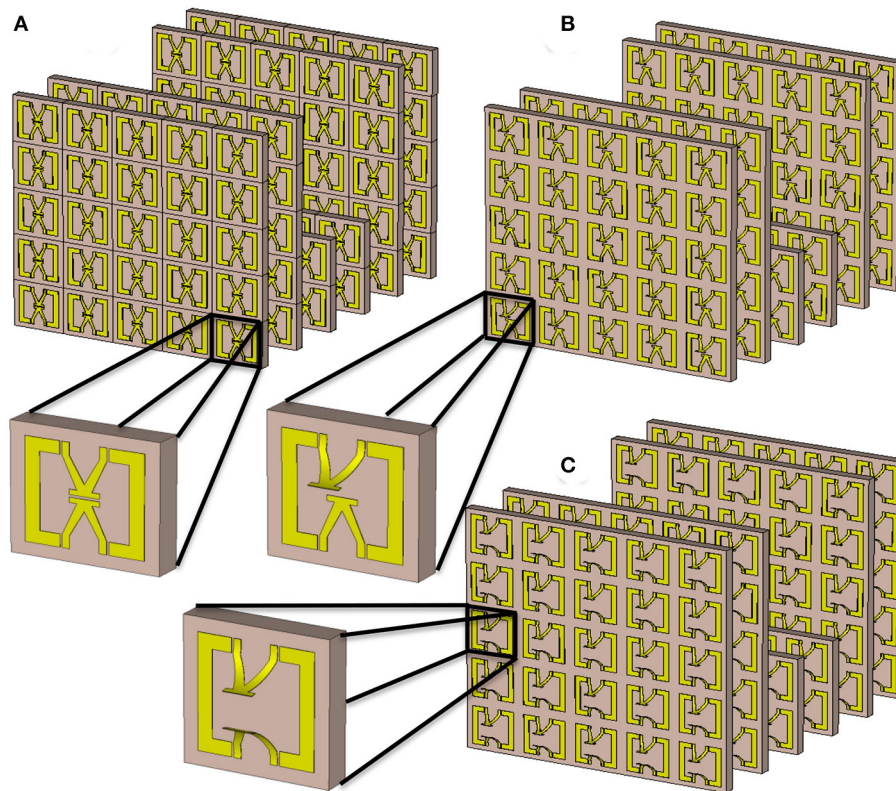**FIGURE 3 |** Combined tunnel structure with its e-field response.

FIGURE 4 | Three different tunnel structures. **(A)** Normal C-V eSRR tunnel structure **(B)** V one arm bend, and **(C)** V two-arm bend of eSRR tunnel structure with unit cells.

different array structures including one arrangement exhibiting tunneling of normal dielectric-metal combination, two providing one- and two-arm bend tunnel combinations and the other exhibiting combined reconfigurable tunnel structure. **Figure 2** indicates the subsequent combinations of the tunnel structure, in which the micro-structured metamaterial tunneled structure was divided into three parts corresponding to the processes of splitting, enhancing, and encoding. According to **Figure 5**, these parts respond to the propagation of electromagnetic waves. The proposed micro metamaterial structure and its operating reconfigurable unit cell are exhibited in **Figure 2**.

The designed C-V metamaterial structure can be modified into a bent structure. After designing three modified reconfigurable structures in one tunnel metamaterial arrangement, the tunnel structure manifested a special response at its passband double negative frequency region. The tunnel structure arrangement is illustrated in **Figure 3**. The first two array structures are of the 5 × 5 array structure indicated by the signal splitter. This part converted the input signal into 11 electron clouds for a 5 × 5 array structure. Following the conversion into 11 clouds, the signal passed through a controller part indicated by the two tunnel arrangements. Here the signal experienced a strong evanescent field effect and was significantly modified. Then, the modified controlled signal finally passed through the encoder part to create binary responses according to field intensity. The procedure is presented in **Figure 3**.

Before designing, the reconfigurable array combination three-unit cells (eSRR) are designed. **Figure 4** exhibits the three-unit cell-based meta-tunnel structure device. All the structures contained a 5 × 5 array unit cell in the signal splitter and encoder region. However, the tunnel area used a 2 × 5 array pattern. The stacked tunnel metamaterial device has six metamaterial array plates, whereby the distance between each plate was 10 μm.

RESULTS AND DISCUSSION

Figures 4A–C depict the proposed eSRR design and the two other tunnel structures. **Figure 5A** describes the scattering parameters of the normal C-V structure. The first structure exhibited transmission resonances of 25.70 and 26.71 THz, with a passband frequency of 25.70 THz. The C-V structure with one V arm bend demonstrated transmission resonances of 25.50 and 26.85 THz (**Figure 5B**), whereas the structure with a tunnel and two V arm bends exhibited transmission resonances of 25.22, 25.98, and 28.75 THz (**Figure 5C**). At the same time, the two reconfigurable structures, namely one arm and two-arm bend structures, exhibited passband resonances of 25.90 and 25.22 THz, respectively. Furthermore, the tunnel structure scattering parameters were better compared to the solid unit cell and array. Meanwhile, the reconfigurable combined tunnel structure exhibited a passband resonance of 29.36 THz.
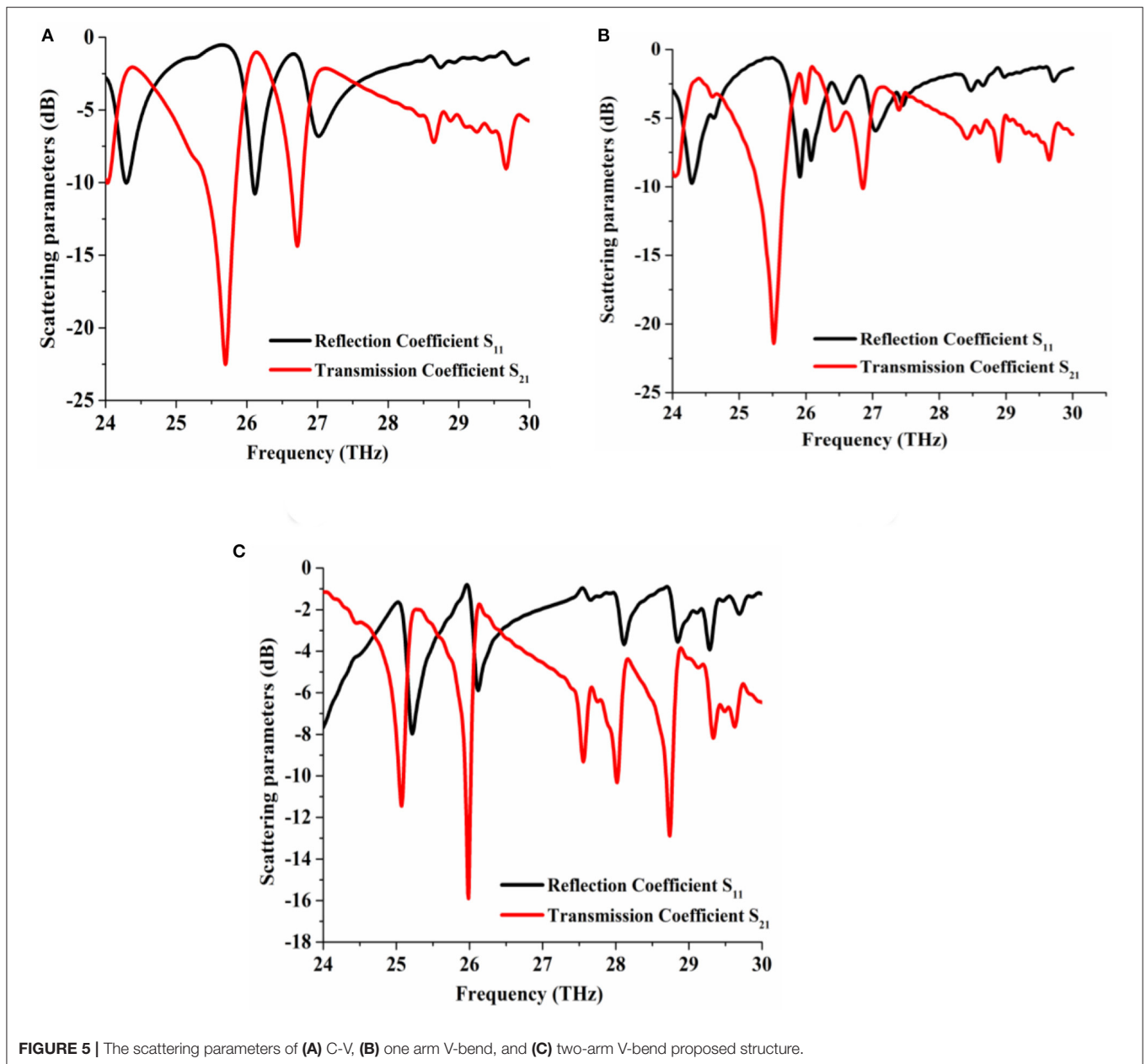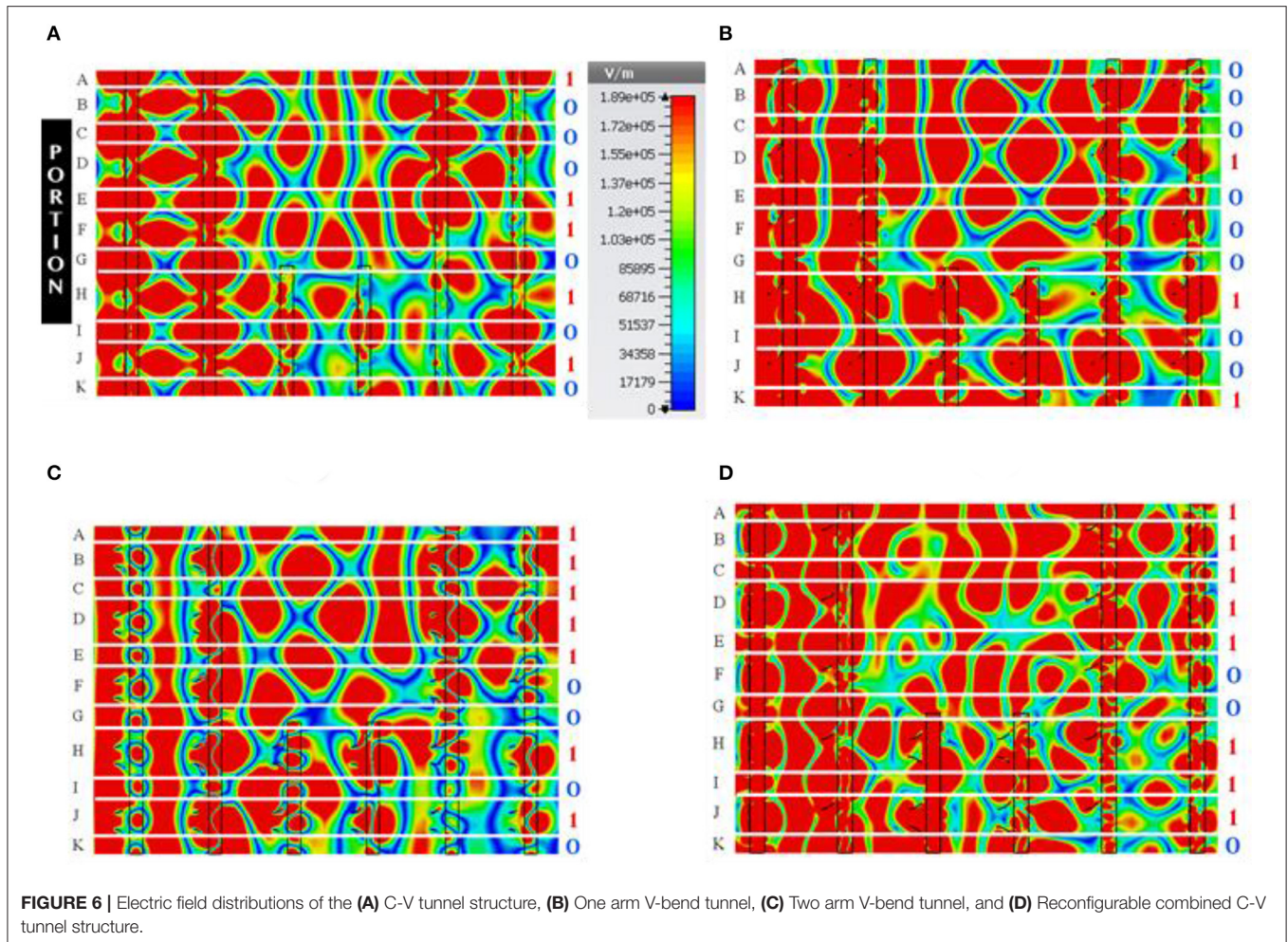
FIGURE 5 | The scattering parameters of **(A)** C-V, **(B)** one arm V-bend, and **(C)** two-arm V-bend proposed structure.

Electrons have a special quality in conveying information from the sender to the receiver. Based on this special behavior, the electric field in a metal-dielectric interface is explored to develop devices like phase shifter, converter, plasmonic power divider, lenses, etc. The evanescent field in the stacked metamaterial tunnel array structure can create different electron cloud patterns that are unavailable in a normal stacked metamaterial array pattern. These metamaterial tunnel array devices could be explained using binary responses. The designed eSRR tunnel structure created a binary response below its λ/2 limits, while creating a strong evanescent field response in the passband field. The characteristics of the introduced tunnel structures were examined using the transverse electromagnetic (TEM)

wave propagation, which interacts partly with the first layer of the metamaterial array and then spreads into eleven clouds of electron regulated by the micro-structured tunnels. The controlled electron clouds were then encoded by the encoding portion whereby the generated signal was delivered to the receiving portion. Next, the modulated electromagnetic electron clouds were transmitted by waveguide port 1 as waveguide port 2 received them. However, based on this condition, the designed four tunnel structures were identified to be in their passband resonances.

In the array pattern, the electric field clouds for the C-V tunnel field contour, V one arm bend, and V two-arm bend in the tunnel field contour are presented in **Figure 6**. The propagation wave
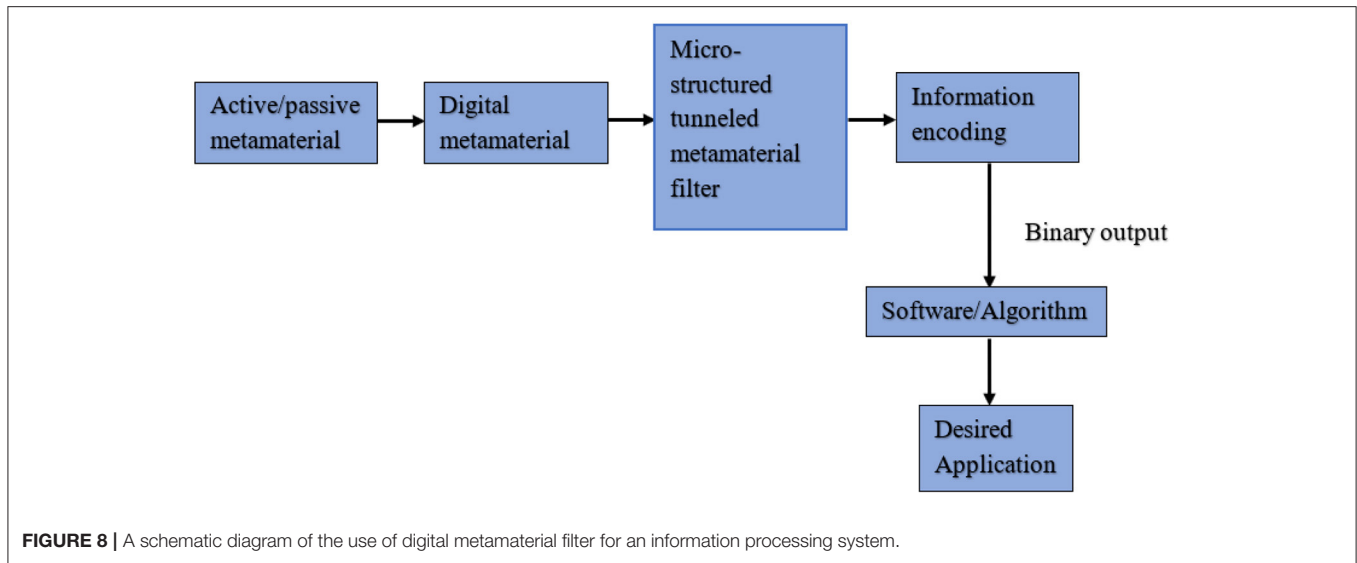
FIGURE 6 | Electric field distributions of the **(A)** C-V tunnel structure, **(B)** One arm V-bend tunnel, **(C)** Two arm V-bend tunnel, and **(D)** Reconfigurable combined C-V tunnel structure.

traveled in a z-direction for all the cases. The tunnel can create a strong evanescent field in a higher frequency region. Therefore, the tunnel array device faces a strong evanescent field contour in the tunnel area. The linear wave experienced a dielectric-metal path in the tunnel area creating a strong evanescent field environment to help obtain different binary responses. In the case of V one arm and two-arm array structures, the wave contours were affected by the dielectric metal interface where its attenuation constant alpha was changed. The wave which experienced a dielectric metal combination with a bend pattern also created a strong evanescent field.

On the other hand, the micro-structured tunnel controlled the strength of the induced electric field. The amplitude of the propagating TEM wave varied when the structural configuration was modified and the electric field intensity was adjusted. When the propagation wave (PW) enters the structure of the first array and gathers information from the last metamaterial slab, the electron clouds formed in the tunnel structure through TEM wave propagation were utilized to convert the electrical signal to information signal as binary output (0 or 1). Therefore, based on the metallic and dielectric parts of the metamaterial tunneled structure, the whole structure can be divided into 11

FIGURE 7 | Binary response of the indicated four-tunnel structure.
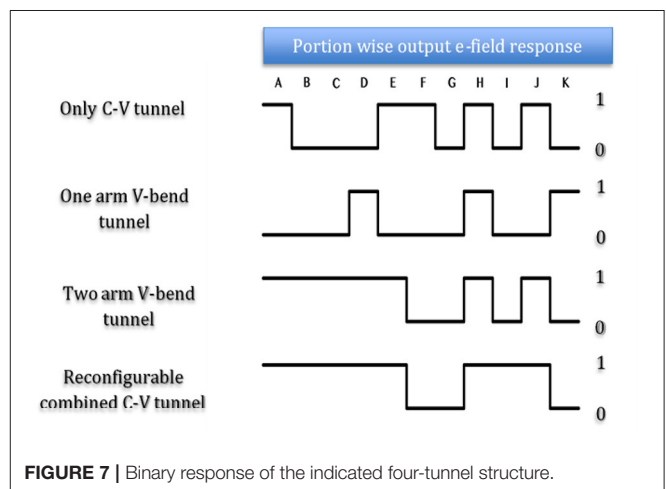
sections. Firstly, the propagating electromagnetic wave occurred during the first metamaterial collection whereby the modulated electron contour was broken into parts. These contours are

FIGURE 8 | A schematic diagram of the use of digital metamaterial filter for an information processing system.

referred to as a cloud and were transformed when the tunnel was inserted (**Figure 6**) which can be explained digitally. Normally, the movement of free electrons can be used for signal encoding in the forms of current or voltage at the dielectric-metal interface.

The information encoded in this study was digitized based on voltage. Binary output "1" referred to the high voltage red area, whereas the low intensity of the remaining colors was classified as binary "0." Portion A of the passband frequency (25.70 THz) in **Figure 6A** indicated that the electron cloud was digitally high, contributing to a high conversion point. Meanwhile, the converted clouds in portions E, F, H, and J were also digitally high and were represented by "1." However, the digitally low electron clouds in portions B, C, D, G, I, and K were classified as "0." Nevertheless, the tunnel structure response for one V arm bend (**Figure 6B**) was digitally high at portions D, H, and K, while digitally low at portions A, B, C, E, F, G, I, and J with 22.89 THz. High response at portions A, B, C, D, E, H, and J were evident for the two-arm bend V tunnel structure, with low responses at portions F, G I, and J at 22.34 THz (**Figure 6C**). Finally, the combined normal and reconfigurable tunnel structure indicated digital responses at 29.34 THz at which the passband was created. This device exhibited digitally high responses at portions A, B, C, D, E, H, I, and J, whereas digitally low responses were recorded at portions F, G, and K (**Figure 6D**).

The digital responses obtained from various portions of the four-tunnel structure are indicated in **Figure 7**. Electric clouds are dominated by the structure of the tunnel, whereby, all the tunnel arrangements responded differently according to the passband resonances. The e-field responses from **Figure 6A** are summarized in **Figure 7** and indicated by only the C-V tunnel; likewise, three more structures are indicated by its digital responses in **Figure 7**.

A schematic diagram of the information processing system using the micro-structured metamaterial device is illustrated in **Figure 8**. Active or passive metamaterial representing the meta-atom structure generated the meta-atom in a digital form.

Next, the micro-structured tunnel configuration was utilized as a filter to encode the binary output from the propagation of waves. Moreover, artificial intelligence (AI) software or algorithm can be used for micro-device applications based on binary outputs.

CONCLUSION

To sum up, a new reconfigurable metamaterial micro-structure was designed and numerically explained based on its binary output to create a digital information filter. The configurations can be completely controlled by the metamaterial tunnel structure arrangement. The electric field was also primarily determined by the configuration of the tunneled micro-structure, whereby the modulated wave signal was encoded to binary output using the proposed meta-device. The entire encoding function was numerically clarified for resonance frequency that corresponded to the reconfigurable tunnel micro-structured metamaterial of one optical passband. A possible schematic diagram of the information processing system was also drawn for the application purpose. In conclusion, the arrangement of the micro-structured tunnel and the flexibility of controlling the moving arms were compatible with an advanced information processing system.

DATA AVAILABILITY STATEMENT

The original contributions presented in the study are included in the article/supplementary material, further inquiries can be directed to the corresponding author/s.

AUTHOR CONTRIBUTIONS

EA and AT: conception and design of the study and analysis of data. EA and RS: initial drafting of the

manuscript. EA, AT, and RS: overall drafting of the manuscript. MF and MI: revising the manuscript critically for important intellectual content. MF: Supervision. All authors contributed to the article and approved the submitted version.

REFERENCES

1. Smith DR, Pendry JB, Wiltshire MC. Metamaterials and negative refractive index. *Science*. (2004) 305:788–92. doi: 10.1126/science.1096796

2. Siddiky AM, Faruque MR, Islam MT, Abdullah S, Khandaker MU. Inverse double-C shaped square split ring resonator based metamaterial with multi-resonant frequencies for satellite band applications. *Results Phys*. (2020) 19:103454. doi: 10.1016/j.rinp.2020.103427

3. Wang Q, Rogers ETF, Gholipour B, Wang C, Yuan G, et al. Optically reconfigurable metasurfaces and photonic devices based on phase change materials. *Nat Photon*. (2016) 10:60–65. doi: 10.1038/nphoton.2015.247

4. Nan J, Yang R, Xu J, Fu Q, Zhang F, Fan Y. Actively modulated propagation of electromagnetic wave in hybrid metasurfaces containing graphene. *EPJ Appl Metamater*. (2020) 7:9. doi: 10.1051/epjam/2020011

5. Cheng K, Fan Y, Zhang W, Gong Y, Fei S, Li H. Optical realization of wave-based analog computing with metamaterials. *Appl Sci*. (2021) 11:141. doi: 10.3390/app11010141

6. Bai X, Kong F, Qian J, Song Y, He C, Liang X, et al. Polarization-insensitive metasurface lens for efficient generation of convergent OAM beams. *IEEE Antennas Wireless Propag Lett*. (2019) 18:2696–700. doi: 10.1109/LAWP.2019.2949085

7. Li H, Kang L, Dong K. Generating tunable orbital angular momentum radio beams with dual-circular-polarization and dual-mode characteristics. *IEEE Access*. (2020) 8:211248–54. doi: 10.1109/ACCESS.2020.30 38568

8. Cui TJ, Qi MQ, Wan X, Zhao J, Cheng Q. Coding metamaterials, digital metamaterials and programmable metamaterials. *Light Sci Appl*. (2014) 3:e218. doi: 10.1038/lsa.2014.99

9. Ma Q, Cui TJ. Information metamaterials: bridging the physical world and digital world. *PhotoniX*. (2020) 1:1–32. doi: 10.1186/s43074-020-00006-w

10. Ahamed E, Faruque MR, Alam MJ, Mansor MF, Islam MT. Digital metamaterial filter for encoding information. *Sci Rep*. (2020) 10:1–9. doi: 10.1038/s41598-020-60170-8

11. Huang C, Sun B, Pan W, Cui J, Wu X, Luo X. Dynamical beam manipulation based on 2-bit digitally-controlled coding metasurface. *Sci Rep*. (2017) 7:1–8. doi: 10.1038/srep42302

12. Gao LH, Cheng Q, Yang J, Ma SJ, Zhao J, Liu S, et al. Broadband diffusion of terahertz waves by multi-bit coding metasurfaces. *Light Sci Appl*. (2015) 4:e324. doi: 10.1038/lsa.2015.97

13. Zhang C, Cao WK, Yang J, Ke JC, Chen MZ, Wu LT, et al. Multiphysical digital coding metamaterials for independent control of broadband electromagnetic and acoustic waves with a large variety of functions. *ACS Appl Mater Interfaces*. (2019) 11:17050–5. doi: 10.1021/acsami.9 b02490

14. Liu H, Zhang Q, Zhang K, Hu G, Duan H. Designing 3D digital metamaterial for elastic waves: from elastic wave polarizer to vibration control. *Adv Sci*. (2019) 6:1900401. doi: 10.1002/advs.201900401

15. Giovampaola CD, Engheta N. Digital metamaterials. *Nat Mater*. (2014) 13:1115–21. doi: 10.1038/nmat4082

16. Shen B, Polson R, Menon R. Integrated digital metamaterials enables ultra-compact optical diodes. *Optics Express*. (2015) 23:10847–55. doi: 10.1364/OE.23.010847

17. Shen Z, Jin B, Zhao J, Feng Y, Kang L, Xu W, et al. Design of transmission-type coding metasurface and its application of beam forming. *Appl Phys Lett*. (2016) 109:121103. doi: 10.1063/1.4962947

18. Ma F, Qian Y, Lin YS, Liu H, Zhang X, Liu Z, et al. Polarization-sensitive microelectromechanical systems based tunable terahertz metamaterials using three dimensional electric split-ring resonator arrays. *Appl Phys Lett*. (2013) 102:161912. doi: 10.1063/1.4803048

19. Han Z, Kohno K, Fujita H, Hirakawa K, Toshiyoshi H. MEMS reconfigurable metamaterial for terahertz switchable filter and modulator. *Optics Express*. (2014) 22:21326–39. doi: 10.1364/OE.22.021326

20. Bilgin H, Yalcinkaya AD, Torun H. MEMS-based terahertz detectors. *Proc Eng*. (2015) 120:15–9. doi: 10.1016/j.proeng.2015.08.556

21. Arbabi E, Arbabi A, Kamali SM, Horie Y, Faraji-Dana M, Faraon A. MEMS-tunable dielectric metasurface lens. *Nat Commun*. (2018) 9:1–9. doi: 10.1038/s41467-018-03155-6

22. Huang Y, Nakamura K, Takida Y, Minamide H, Hane K, Kanamori Y. Actively tunable THz filter based on an electromagnetically induced transparency analog hybridized with a MEMS metamaterial. *Sci Rep*. (2020) 10:20807. doi: 10.1038/s41598-020-77922-1

23. Argyris A, Grivas E, Bogris A, Syvridis D. Transmission effects in wavelength division multiplexed chaotic optical communication systems. *J Lightwave Technol*. (2010) 28:3107–14. doi: 10.1109/JLT.2010.2073444

24. Willner AE, Khaleghi S, Chitgarha MR, Yilmaz OF. All-optical signal processing. *J Lightwave Technol*. (2013) 32:660–80. doi: 10.1109/JLT.2013.2287219

Advantages of publishing in Frontiers

OPEN ACCESS
Articles are free to read
for greatest visibility
and readership

FAST PUBLICATION
Around 90 days
from submission
to decision

HIGH QUALITY PEER-REVIEW
Rigorous, collaborative,
and constructive
peer-review

TRANSPARENT PEER-REVIEW
Editors and reviewers
acknowledged by name
on published articles

Frontiers
Avenue du Tribunal-Fédéral 34
1005 Lausanne | Switzerland

Visit us: www.frontiersin.org
Contact us: frontiersin.org/about/contact

REPRODUCIBILITY OF RESEARCH
Support open data
and methods to enhance
research reproducibility

DIGITAL PUBLISHING
Articles designed
for optimal readership
across devices

FOLLOW US
@frontiersin

IMPACT METRICS
Advanced article metrics
track visibility across
digital media

EXTENSIVE PROMOTION
Marketing
and promotion
of impactful research

LOOP RESEARCH NETWORK
Our network
increases your
article's readership